From the holdings of the Department of Special Collections , Princeton University Library, Princeton, NJ

These documents are either in the public domain, or can only be used for educational and research purposes (Fair use) as per U.S. Copyright law (text below). By accessing this file, all users agree that their use falls in the public domain or within fair use as defined by the copyrightlaw. We do not charge any permission or usage fees for the publication of images of material inour collections, including those provided by Princeton University Library, via our website, catalog, or directly from staff.For more information regarding copyright, credit, and citation please review the information onthe Copyright, Credit and Citation Guidelines page of our website.
https://library.princeton.edu/special-collections/policies/copyright-credit-and-citation-guidelines. If you have any questions, including how to order higher-quality images from the collection, contact Special Collections Public Services via our Ask Us! Form. https://library.princeton.edu/special-collections/ask-us

---

Doctoral Dissertations, 2011-2026 Atmospheric and Oceanic Sciences

2019

THE EFFECTS OF GREENHOUSE GASES AND ABSORBING AEROSOLS ON TROPICAL PRECIPITATION

Chua, Xin Rong

Princeton, NJ : Princeton University

---

http://arks.princeton.edu/ark:/88435/dsp01n009w520c

U.S. Copyright law: The copyright law of the United States (Title 17, §108, United States Code) governs the making of photocopies or other reproductions of copyrighted material. Under certain conditions specified in the law, libraries and archives are authorized to furnish a photocopy or other reproduction. One of these specified conditions is that the photocopy or reproduction is not to be used for any purpose other than private study, scholarship, or research. If a user makes a request for, or later uses, a photocopy or reproduction for purposes in excess of fair use that user may be liable for copyright infringement. This institution reserves the right to refuse to accept a copying order if, in its judgment, fulfillment of the order would involve a violation of copyright law. https://www.copyright.gov/title17/title17.pdf

The effects of greenhouse gases and absorbing aerosols on tropical precipitation

Xin Rong Chua

A Dissertation
Presented to the Faculty
of Princeton University
in Candidacy for the Degree
of Doctor of Philosophy

Recommended for Acceptance
by the Program in
Atmospheric and Oceanic Sciences
Adviser: Dr. Yi Ming

September 2019

© Copyright by Xin Rong Chua, 2019.

All rights reserved.

Abstract

Greenhouse gases and absorbing aerosols warm the climate system by absorbing radiation. At the same time, aerosol particles also have the potential to significantly alter cloud microphysics. This thesis explores the hydrological implications of the radiative and microphysical perturbations using cloud-resolving model (CRM) and global climate model (GCM) simulations.

Absorption from greenhouse gases and absorbing aerosols heats the atmosphere on the fast time scales of days to months, thereby reducing mean precipitation. It is identified using CRM simulations in radiative-convective equilibrium (RCE) that the reduction mainly comes from weak, rather than strong, precipitation events. The intensity of strong events is maintained by a compensation between an increase in boundary layer moisture and a reduction in updraft frequency.

An often-cited hypothesis in aerosol-cloud interactions is that increased cloud droplet number concentrations allows more cloud water to be lofted above the freezing level, releasing additional latent heat that invigorates convection. Our RCE experiments show that ice processes are not necessary for convective invigoration, with the evaporation of cloud droplets playing a more important role.

To address the effects of spatial inhomogenity of aerosol distributions on extreme events, we investigate the effect of different spatial distributions of black carbon aerosols on tropical cyclone (TC) statistics on fast time scales using the Geophysical Fluid Dynamics Laboratory (GFDL) GCM HiRAM. Free-tropospheric black carbon is much more effective than boundary layer black carbon in altering TC statistics. The atmospheric heating of BC leads to larger reductions in TC intensity as compared to carbon dioxide.

In boreal winter, the cold surges associated with the movements of the Siberian high contribute significantly to mean and extreme precipitation over the Maritime Continent. Using simulations from the GFDL AM4, we predict increases in surge

precipitation under surface warming. The increase in surge precipitation is amplified under a more realistic spatial pattern of warming.

The physical understanding obtained by the combination of theory and models in this thesis serve as a guide for policymakers in planning for rainfall under a changing climate.

Acknowledgements

Before beginning this thesis, I would like to thank the people who have supported me in my scientific journey.

My greatest debt of gratitude goes to my advisor Yi Ming for his dedicated guidance and support. Yi has been a great mentor who kept faith with me even when times were tough. It has also been a pleasure to collaborate with Nadir Jeevanjee, who provided both critical insight and guidance.

My committee members Leo Donner, Stephan Fueglistaler and Ming Zhao have been highly valuable in helping me grow as a scientist. I also benefited greatly from discussions with Jenny Chang, Stephen Garner, Huan Guo, Lucas Harris, Muhammad Hassim, Xianan Jiang, Hugh Morrison and David Paynter. Shuguang Wang made his version of the Weather Research and Forecasting model available and was very forthcoming with advice and suggestions. Usama Anber, Spencer Clark, and Hailey Shin generously gave of many hours of their time as I found my footing with various computational tools. I also thank the modeling and support teams of GFDL for their work and assistance.

My studies were supported by the National Research Foundation of Singapore and the Cooperative Institute of Climate Science/ Cooperative Institute for Modeling the Earth System. The support of the AOS program staff, especially Anna Valerio, Laura Rossi, and Chris Ober is also greatly appreciated, as is the administrative support provided by the Public Utilities Board of Singapore.

I have many treasured memories of the AOS program, GFDL, and Princeton. My cohort – Jenny Chang, Spencer Clark, Michelle Frazer, Tsung-Lin Hsieh, Justin Ng, and Sarah Schlunegger – provided camaraderie, support, and laughter, and I will regard our friendship as of my major takeaways from Princeton. Katja Luxem and Noemi Vergopolan encouraged my interests in organizing discussions about the environment. Lisa Lonie introduced me to the joys of the carillon community. Mary-Ann

Cavallaro was a gracious and welcoming host parent who I am glad to have befriended. The university Writing Center as well as the writer's group at the Princeton Public Library provided excellent support in helping me grow as a writer. My journey from Singapore to Princeton was made possible by Xi Xi and Jason Cohen, who introduced me to the field. At various points, I benefited from discussions with researchers at the Centre for Climate Research Singapore, the Centre for Environmental Sensing and Modeling, and the Tropical Marine Science Institute. I am particularly grateful to Tieh-Yong Koh, Hock Lim, and Chee Kiat Teo for their generous advice and guidance.

Finally, I thank my parents for their support of my pursuit to obtain a PhD.

Contents

Abstract iii

Acknowledgements v

List of Tables x

List of Figures xii

1 Introduction **1**

1.1 Motivation 1

1.2 Overview 4

2 The fast response of precipitation intensity to atmospheric heating **6**

2.1 Introduction 6

2.2 Methods 8

2.3 Results 10

2.3.1 Domain-average responses 10

2.3.2 Precipitation intensity 14

2.3.3 Boundary layer energy balance 17

2.4 Discussion and summary 18

2.5 Acknowledgments 20

2.A Frameworks for re-evaporation 21

3 On the role of liquid microphysical processes in convective invigoration **26**

3.1 Introduction . . . 26
3.2 Methods . . . 27
3.2.1 Model . . . 27
3.2.2 Experiments . . . 28
3.2.3 Definition of convective mass flux . . . 29
3.3 Domain-mean vertical responses . . . 29
3.4 Connections between thermodynamic, dynamic, and microphysical variables . . . 34
3.5 Conclusions . . . 42
3.5.1 Discussion . . . 42
3.5.2 Summary . . . 44
3.6 Acknowledgments . . . 44

4 The fast response of tropical cyclones to black carbon 46
4.1 Introduction . . . 46
4.2 Methods . . . 51
4.2.1 Model description . . . 51
4.2.2 Experimental design . . . 52
4.3 Results . . . 53
4.3.1 Magnitudes and spatial distributions of atmospheric absorption 53
4.3.2 Changes in TC frequency and intensity . . . 57
4.3.3 Connections with large-scale environment . . . 60
4.4 Discussion . . . 72
4.5 Conclusions . . . 75
4.6 Acknowledgments . . . 75

5 The effect of surface warming on cold surges over the Maritime Continent 77

5.1 Introduction 77
5.2 Methods 79
5.2.1 Model, data and experiments 79
5.2.2 Definition of cold surges 80
5.2.3 Weather regime classification 80
5.2.4 Statistical significance 81
5.2.5 Moisture budget analysis 81
5.3 Evaluation of AM4 82
5.3.1 Weather regimes 82
5.3.2 Cold surges 83
5.4 Results 85
5.4.1 Temperature and precipitation 85
5.4.2 Moisture budget analysis 86
5.4.3 Connections with large-scale environment 87
5.5 Conclusions 87
5.5.1 Discussion 87
5.5.2 Summary 88
5.6 Acknowledgments 89

6 Conclusions **101**
6.1 Summary and implications 101
6.2 Limitations and future work 103

Bibliography **106**

List of Tables

2.1 Domain-average tropospheric radiative cooling (RA, W m^{-2}), surface sensible heat flux (SH, W m^{-2}), surface latent heat flux (LH, W m^{-2}), near-surface temperature (T_a, K) and water vapor mixing ratio (q_a, g kg^{-1}), precipitation (P, mm day^{-1}), and changes in the perturbation cases. All changes are significant. 11

3.1 The values of γ [the ratio of column-integrated re-evaporation (E) to column-integrated condensation (C)], E and its rain (ER) and cloud (EC) components, C, accretion (AR), precipitation P in the BASE liquid microphysics experiments, and their changes in BASE* (δBASE*). Except for γ, which is unitless, all the quantities are domain-averaged and in mm day^{-1}. The connections between the processes in LIQ are illustrated in Figure 3.5. In FULL, additional ice processes (Table 3.2) are involved in ER, EC, C, and AR. 36

3.2 Additional ice processes included in the calculation of the terms in Table 3.1 in the FULL cases. 45

4.1 Tropical-mean changes in the various components of the atmospheric energy balance (W m^{-2}). The fractional changes (percentage) are in parentheses. 54

4.2 Fractional changes (percentage) in TC and hurricane counts in the entire, Northern Hemisphere (NH) and Southern Hemisphere (SH) tropics. Statistically significant values are in bold. 57

4.3 Fractional changes (percentage) of genesis-weighted precipitation (P), 500-hPa vertical velocity ($-\omega_{500}$), wind shear (S), potential intensity ($\mathcal{I}$), thermodynamic efficiency ($\mathcal{T}$) and enthalpy difference ($\mathcal{E}$). 62

5.1 The relative frequency (fraction) of the three most frequent weather regimes in DJF, and their sum, in observations (OBS) and in AM4, in descending order of dryness (vertically-averaged relative humidity). Values significantly different from AM4 are in bold. 83

5.2 The mean and standard deviation (std) components of the wind index, the pressure index, and the surge frequency (f_s, unitless). Winds are given in m s^{-1} and SLP in hPa. Values significantly different from AM4 are in bold. 84

List of Figures

2.1 Vertical profiles of (a) temperature (T, K), (b) water vapor mixing ratio (q, g kg^{-1}), (c) equivalent potential temperature (θ_e, K), (d) cloud fraction in BASE. (e-h) Changes in (a-d) due to heating (prefixed by δ) in HEAT, A850, and B850. All changes rise significantly above the noise level. 13

2.2 (a) The domain-average precipitation ($p(r>r_t)$, mm day^{-1}) of the events whose hourly precipitation rates exceed r_t (mm day^{-1}) in the full re-evaporation experiments. (b) $p(r>r_t)$ normalized by domain-mean precipitation P. (c) The scatter plot of r (mm day^{-1}) against 500-hPa vertical velocity (w, m s^{-1}) for BASE and HEAT. The solid lines are the best-fit lines with zero-intercept for $w > 0.1$ m s^{-1}. (d) The probability of w exceeding a threshold w_t (m s^{-1}), or $\int_{w_t}^{\infty} \mathcal{P}(w)dw$, for $w_t > 0.1$ m s^{-1}. (e) The domain-average precipitation ($p(w>w_t)$, mm day^{-1}) of the events where w exceeds w_t, estimated with Equation 2.3. (f) The difference in $p(w>w_t)$ (m s^{-1}) between BASE and HEAT, and its thermodynamic and dynamic components and their sum, estimated with Equation 2.4. 22

2.3 (a) The individual terms in the boundary layer energy balance (W m^{-2}) in BASE: surface sensible heating (SH), radiative cooling (RA_b), re-evaporative cooling (RE) and the exchange of sensible heat with the free troposphere (EX). (b) Changes in HEAT, A850 and B850. (c,d) Same as (a,b), but for the partial re-evaporation cases. The solid and dashed lines denote the change in SH calculated from the predictive theories that include (Equation 2.5) and exclude (Equation 2.7) the effect of re-evaporative cooling, respectively. 23

2.4 As in Figure 1, but for BASE*, HEAT*, A850*, and B850*. 24

2.5 Scatter plots related to frameworks for changes in re-evaporation. The solid lines are the one-to-one lines. (a) Fractional changes in re-evaporation (E) against fractional changes in precipitation (P) (circles, best-fit slope with no-intercept of 1.1 and $R = 0.97$) and the sum of fractional changes in $1 - RH$ and the fall velocity (w_f), calculated as in Lutsko and Cronin (2018) (crosses, best-fit slope with no intercept of 2.8 and $R = 0.86$). (b) Fractional changes of the re-evaporation efficiency (β) against the sum of fractional changes in $1 - RH$ and the fall velocity (the same quantity as in (a)). The best-fit slope with no intercept is 0.47, with $R = 0.85$. 25

3.1 Domain-average vertical profiles of (a) cloud liquid (solid) and ice (dashed) condensates (q_c, 10^{-5} kg kg^{-1}), (b) precipitating liquid (solid) and ice (dashed) condensates (q_p, 10^{-5} kg kg^{-1}) and (c) cloud fraction (unitless) in the BASE experiments. Cloud fraction is calculated using a condensate and vertical velocity threshold as in Chapter 2. (d-f) Changes in (a-c) due to δBASE*. The shading in (d-f) represents the noise in BASE. 30

3.2 Domain-average vertical profiles of (a) convective mass flux (M_c, g m^{-2} s^{-1}), (b) updraft vertical velocity (m s^{-1}), and (c) updraft fraction (%) in the BASE experiments. (d-f) Changes in (a-c) due to δBASE*. The shading in (d-f) represents the noise in BASE. 31

3.3 Domain-average vertical profiles of (a) relative humidity (RH, unitless), (b) temperature (T, K) and (c) water vapor mixing ratio (q_v, g kg^{-1}) in the BASE experiments. (d-f) Changes in (a-c) due to δBASE*. The shading in (d-f) represents the noise in BASE. 33

3.4 Scatter plots of (a) vertically averaged convective mass flux ($[M_c]$, g m^{-2} s^{-1}) against column relative humidity (CRH), (b) $[M_c]$ against mid-tropospheric (600 to 400 hPa) relative humidity (MRH), (c) CRH against the ratio of column-integrated re-evaporation to condensation (γ, unitless), (d) MRH against γ in all experiments. 35

3.5 Column-integrated and domain-averaged values (mm day^{-1}) of microphysical processes converting between water vapor (q_v), cloud condensates (q_c) and precipitating condensates (q_p) [condensation of cloud condensates (C), evaporation of cloud condensates (EC), conversion of cloud water to rain by autoconversion (CR) and accretion (AR) and evaporation of rain (ER)], as well as surface evaporation (ES) and precipitation (P) for (a) LIQ and (b) δLIQ*. The corresponding values for all configurations are listed in Table 3.1. 38

3.6 Domain-average vertical profiles of the microphysical (mp), advection (adv), vertical diffusion (vdif) and radiative (rad) heating rates in (a) FULL, (b) LIQ, (c) RE and (d) CE. (e-h) Changes in (a-d) due to δBASE*.The vertically-averaged value of the absolute changes in mp is given on the top left hand corner. All values are in K day^{-1}. . . . 39

3.7 The decomposition of the microphysical term in Figure 3.6 (mp) into contributions from rain re-evaporation (er), formation of cloud droplets by condensation (cc), evaporation of cloud droplets (ec), and ice processes (ice) in the BASE configurations (a) FULL, (b) LIQ, (c) RE and (d) CE. (e-h) Changes in (a-d) due to δBASE*. All values are in K day^{-1}. 41

4.1 Geographical distributions of the changes in atmospheric absorption (W m^{-2}, δAS for BC cases and δAL for CO2). The numbers in parentheses indicate the fraction over the ocean (f_o). The rectangle boxes denotes the main development regions, as is the case for the other maps in this chapter. 55

4.2 Vertical distributions of the tropical-mean changes in radiative heating rate (K day^{-1}, shortwave for the BC cases and longwave for CO2). . . 57

4.3 Geographical distributions of the changes in annual-mean TC genesis counts averaged over 4° × 5° grids. 59

4.4 Changes in TC intensity as measured by δF (upper), $N\delta P$ (middle) and δI (lower). See text for explanation. 63

4.5 Geographical distributions of the changes in genesis-weighted 500-hPa vertical velocity ($\delta[-\omega_{500}]_G$, hPa day^{-1}). Tropical-mean values are in parentheses. 64

4.6 Same as Figure 4.5, but for wind shear (S, m s^{-1}). 65

4.7 Same as Figure 4.5, but for potential intensity ($\mathcal{I}$, m s^{-1}). 68

4.8 Vertical distributions of the tropical-mean changes in air temperature (K). 70

4.9 Tropical-mean changes in atmospheric heating rates (K day^{-1}) in FT and BL. They include shortwave radiation (SW), longwave radiation (LW), convective (CV) and large-scale (LS) latent heating, and vertical diffusion (VD) and dynamical advection (DY) of sensible heat. 71

5.1 Precipitation (mm day^{-1}, contours) and low-level (850 hPa) winds (m s^{-1}, vectors) averaged over all (a) DJF days (b) surge days (c) non-surge days. The precipitation averaged over the oceans around Borneo (within the black box) is given in the top left hand corner. The red boxes are used in the definition of the surges (see Methods). (d-f) As in (a-c), but for AM4. 90

5.2 Climate variables used to perform the weather regime classification in OBS: (a) relative humidity (RH, fraction), (b) equivalent potential temperature (θ_e, K), (c) wind vectors (m s^{-1}), (d) temperature anomalies relative to the annual mean (K). The dashed lines represent the annual climatological mean. (e-h) As in (a-d), but for AM4. 91

5.3 (a-d) Precipitation (mm day^{-1}, contours) and low-level (850 hPa) winds (m s^{-1}, vectors) averaged over the days in R1-R4 in OBS, respectively. (e-h) As in (a-d), but in AM4. 92

5.4 (a) Precipitation (mm day^{-1}, contours) and low-level (850 hPa) winds (m s^{-1}, vectors) due to surges in OBS (i.e. (b)-(c) in Figure 5.1). (b) As in (a), but for AM4. The precipitation averaged over the oceans around Borneo (within the black box) is given in the top left hand corner. The red boxes are used in the definition of the surges (see Methods). 93

5.5 Geographical distribution of changes in DJF surface temperature (T_s, K) in (a) 2K (b) P1. The global mean temperature change is given in parentheses. 94

5.6 Zonal-mean DJF temperature changes in the Northern Hemisphere ($[T]$, K) in (a) 2K (b) P1. 95

5.7 The changes in (a) surge and (b) DJF precipitation (mm day^{-1}, contours) and 850 hPa winds (m s^{-1}, vectors) in 2K. The percentage increase in precipitation over the ocean around Borneo (box) is given in the top left corner, with the percentage increase in parantheses. (c-d) As in (a-b), but for P1. 96

5.8 Changes in (a) evaporation (E), (b) advection of moisture by the mean circulation (MC) and its (c) thermodynamic (TD) and (d) dynamic (DY) components in 2K. Values averaged over the surge area (box) are given in the top left corner. (e-h) As in (a-d) but for P1. All values are in mm day^{-1}. 97

5.9 Geographical changes in sea level pressure (SLP, hPa) for (a) 2K and (b) P1 in DJF. Changes averaged over the Siberian High (rectangle) are given in parantheses. 98

5.10 Geographical changes in 300 hPa temperature (T_{300}, K) (contours) and winds (vectors) for (a) 2K and (b) P1 in DJF. Temperature changes averaged over the Siberian High (rectangle) are given in parantheses. 99

5.11 As in Figure 5.10, but for 700 hPa temperature (T_{700}, K). Missing values due to the presence of topography have been masked in gray. 100

Chapter 1

Introduction

1.1 Motivation

The bulk of Earth's precipitation falls in the tropics, nourishing and sometimes destroying the habitats of the majority of its species and human population. Precipiation takes place in the form of weak drizzle or strong events such as convecting thunderstorms. Disorganized events triggered by surface heating ('popcorn' convection, Martin and Suomi (1972)) serve as an important source of precipitation, and can be responsible for flash floods (National Environmental Agency, 2010). On larger scales, convection can exhibit coherent structures through their interaction with the environment. One example is the tropical cyclone, which typically undergoes genesis in warm, moist oceanic regions (Gray, 1968). Organized by Earth's rotation, the broader circulation of the TC extends up to O(100km) from the eye (Schenkel et al., 2017). The destruction tropical cyclones can cause is illustrated by Typhoon Yolanda (Haiyan), which cost $43 billion Philippine pesos (approximately USD 900 million) in damages after it hit the Philippines (NDRRMC, 2014)). At the same time, typhoons supply almost half (47.5%) of the rainfall in Taiwan during July - September, thereby serving to support agricultural activity (Chen et al., 2010). Another is the equatorial

cold surge (Chang et al., 1979) triggered by movements of the Siberian High during boreal winter (Ding, 1993). After being warmed and moistened by surface fluxes over the South China Sea (Johnson and Houze, 1987), the surge winds deposit rainfall on the Maritime Continent, the mixture of land and ocean that separates mainland Asia from Australia. The presence of cold surges is one reason why precipitation in the Maritime Continent peaks in boreal winter, thereby supporting the growing season in Indonesia (e.g. Naylor et al., 2007). Cold surges are also responsible for extreme rainfall events across the Maritime Continent (Tangang et al., 2008; Pullen et al., 2015; Lim et al., 2017). Given the myriad impacts of precipitation, we seek to understand how its intensity and frequency distribution is shaped by anthropogenic influences.

Humans impose a significant perturbation on the climate system by burning fossil fuels and biomass, which releases greenhouse gases and aerosols. Greenhouse gases are well-mixed in the atmosphere with a lifetime of decades to centuries, and contribute a radiative forcing of 2.54-3.12 W m^{-2} (Myhre et al., 2013), mostly due to absorption of longwave radiation. Aerosols are tiny solid or liquid particles which are removed from the atmosphere via gravitational settling and dry and wet deposition (Seinfeld and Pandis, 2012) in days-weeks (e.g. Bond et al., 2013), and thus exhibit high concentrations close to their sources, particularly in Asia, America, and Europe and largely confined within the lowest two kilometers of the atmosphere (Boucher et al., 2013). Depending on their chemical composition, aerosols can either absorb or scatter shortwave and longwave radiation (the direct effect). In addition, aerosols can also alter cloud albedo (Twomey, 1974) and lifetime (Albrecht, 1989), known as the indirect effects. Strongly absorbing in the shortwave, black carbon contributes a radiative forcing of 0.3-1.1 W m^{-2}, a heating second only to that of greenhouse gases (Myhre et al., 2013).

To reason effectively about the consequences of the spatially complex and mechanistically diverse anthropogenic forcing on tropical precipitation, this thesis places

heavy emphasis on identifying physically robust constraints. One such constraint is the global atmospheric energy balance between surface sensible and latent heat fluxes and radiative cooling. To leading order, in the global-mean, this constraint dictates that increases in column-integrated atmospheric absorption of radiation are balanced by reductions in latent heating from precipitation (e.g. Allen and Ingram, 2002). By a moisture budget argument, a decrease in precipitation acts to weaken the atmospheric circulation (e.g. Held and Soden, 2006). In contrast, high precipitation extremes are constrained by the balance between adiabatic cooling from the vertical advection of moisture and latent heat from condensation (e.g Muller et al., 2011). Chapter 2 helps extend the two constraints to the intensity distribution of precipitation.

Besides interacting with radiation, aerosols can also alter the intensity of convection and precipitation (e.g. Andreae et al., 2004; Rosenfeld et al., 2008; Lebo and Seinfeld, 2011). An oft-cited mechanism (Rosenfeld et al., 2008) is that latent heat from freezing serves as a source of buoyancy that invigorates updrafts, but the relevance of this hypothesis in the climate setting has not been rigorously tested. Through testing this hypothesis, Chapter 3 uncovers the role of various microphysical processes through which increased aerosol concentrations alter convection.

Additional constraints on organized convection can be obtained by examining the mechanisms governing the underlying physical phenomena. Conceptualizing of the tropical cyclone (TC) as a 'heat engine' that converts surface heat fluxes to mechanical energy in the form of winds (Emanuel, 1986), the potential intensity theory serves as a theoretical bound on TC wind speeds. Together with climatological factors known to favor TCs such as mid-tropospheric ascending motions and low wind shear, PI has been used in the construction of indices that predict TC genesis (e.g. Camargo et al., 2007b). The applicability of genesis predictors and PI in the face of a spatially inhomogenous forcing such as absorbing aerosols has received relatively little attention, motivating the work of Chapter 4. In addition, an explicit investigation

into the behavior of cold surges under warming remains absent from the literature. Chapter 5 addresses this gap by investigating how the mechanisms which govern surge rainfall change under surface warming.

1.2 Overview

This thesis seeks to understand the multi-faceted influences of greenhouse gases and absorbing aerosols on tropical precipitation. Chapters 2 and 3 focus on a mechanistic understanding of simulated clouds and convection in the idealized setting of radiative-convective-equilibrium using a cloud-resolving model. Chapter 2 investigates the fast response of precipitation intensity to atmospheric heating. We analyze the roles of free-troposphere and boundary heating on near-surface temperature. Chapter 3 analyzes the impact of increases in cloud droplet number concentrations on convection. We make use of mechanism denial experiments to identify the key physical processes underlying the changes in convection.

Chapters 4 and 5 explore how aspects of intense tropical precipitation interact with the changes in the large scale circulation brought about by the heating from greenhouse gases and absorbing aerosols. In Chapter 4, we find that the fast response of the atmosphere to heating from black carbon aerosols acts to reduce the frequency and intensity of tropical cyclones. We relate the changes in tropical cyclone statistics to changes in environmental parameters known to influence TC behavior. Chapter 5 explores the effect of surface warming precipitation over the Maritime Continent in boreal winter, with an emphasis on cold surges. Chapter 6 concludes with a summary of the work and its implications, together with a discussion on the limitations of this thesis and how they might be addressed in future work.

Chapter 2 is joint work with Yi Ming and Nadir Jeevanjee, and Chapters 3-5 are joint work with Yi Ming. Chapter 2 forms the basis of Chua et al. (2019); Chapter 4

has been submitted to Journal of Climate. Chapter 2 has been presented at American Geophysical Union (AGU) meeting in 2017 and 2018, the Asia-Oceania Geosciences Society meeting (AOGS) in 2017, and the Gordon Research Seminar and Conference (GRC) in 2017. Chapter 4 has been presented at the American Meterological Society meeting in 2017, AGU 2015 and 2016, AOGS 2015, GRC 2015, and the Monsoons and ITCZ Workshop 2015.

Chapter 2

The fast response of precipitation intensity to atmospheric heating

2.1 Introduction

Greenhouse gases and absorbing aerosols warm the climate by absorbing longwave and shortwave radiation, respectively. Greenhouse gases represent the strongest anthropogenic climate forcing, with top-of-the-atmosphere (TOA) values of 2.54-3.12 W m^{-2} (Myhre et al., 2013). Unlike well-mixed greenhouse gases, unevenly distributed absorbing aerosols can lead to local TOA forcing exceeding 20 W m^{-2} (e.g. Strong et al., 2015). The radiative heating gives rise to a fast (days to months) atmosphere-land response and a slow (years or longer) response that involves the ocean (e.g. Andrews and Forster, 2010). Given the different time scales, the two responses can be approximated as distinct. In fact, global climate model (GCM) simulations indicate that the fast response to atmospheric absorption acts to reduce global-mean precipitation, while the slow response has the opposite effect (Andrews et al., 2010; Ming et al., 2010; Fläschner et al., 2016). Thus, one can study the fast response in isolation from the slow response.

On fast time scales, an increase in atmospheric radiative heating must be partially balanced by a reduction in surface latent heat flux (and mean precipitation) (Andrews et al., 2010; Bala et al., 2010; Dinh and Fueglistaler, 2017; Richardson et al., 2015). This change in mean precipitation need not scale with, or even agree in sign, with those of precipitation extremes. Under a quadrupling of CO_2, GCMs consistently simulate reductions in mean precipitation (-3 to -8%), but disagree on the sign of the change in annual maximum daily precipitation (Sillmann et al., 2017).

Besides the lack of consensus among models identified by Sillmann et al. (2017), there are many well-known reasons to doubt the capability of GCMs in simulating extreme precipitation with parameterized moist convection, especially in the tropics (O'Gorman, 2015). GCMs typically underestimate intense precipitation when compared with observations, with the biases being more severe for low-resolution GCMs (1° or coarser) (Stephens et al., 2010; Kopparla et al., 2013; Sillmann et al., 2013; O'Brien et al., 2016). While the convective parameterization of a GCM can be altered to better match observations, a troubling sign is that such a modification can lead to larger changes in the frequency of heavy rain than a 2 K increase in sea surface temperatures (SSTs) (Wilcox and Donner, 2007), casting in doubt the utility of GCMs in studying extreme precipitation changes.

In light of the limited resolution of GCMs, we turn to cloud-resolving models (CRMs) on a limited-area domain, which have been shown to produce realistic simulations of heavy rain events when forced with proper boundary conditions (e.g. Fan et al., 2015; Lee et al., 2016; Hodzic and Duvel, 2018). Since what is at issue here is the general characteristics of the fast response to atmospheric heating, we intentionally move away from detailed simulation of a particular region or event in favor of a setting that is more representative of the climate system, namely radiative-convective equilibrium (RCE). One advantage of RCE is that both energy and moisture are conserved within the atmosphere, which need not be the case for individual events. RCE

is an idealized representation of the atmosphere where radiation and convection balance in the absence of lateral energy transport. RCE studies of surface warming have identified a strong link between precipitation intensity and boundary layer moisture (e.g. Muller et al., 2011; Romps, 2011).

In this study, we investigate the fast response of precipitation intensity to atmospheric heating in a CRM. This motivates us to also analyze the boundary layer energy balance in order to better identify the physical mechanisms through which elevated heating affects boundary layer temperature and humidity. Existing works have focused on the balance among surface sensible heating, radiative cooling and entrainment of free-tropospheric air into the boundary layer (Ball, 1960; Lilly, 1968). The entrainment term is often parameterized as a fixed fraction of the surface sensible heat flux (0.2 or 0.25 in Betts, 1973; Tennekes, 1973; Betts and Ridgway, 1989; Betts, 2000; Cronin, 2013), implying that the sensible heat flux is tightly coupled to the boundary layer radiative cooling. While Betts (2000) later recognized that re-evaporative cooling might contribute to the boundary layer energy balance, a possible change in re-evaporation under warming is not taken into account explicitly in the analytical models of climate sensitivity (Takahashi, 2009; Cronin, 2013). To guide future theoretical development, we systematically evaluate the responses of the boundary layer energy budget to boundary layer versus free-tropospheric heating.

2.2 Methods

We use the Advanced Research Weather Research and Forecasting (WRF) model configured to run in RCE (Wang and Sobel, 2011). Radiative transfer is reduced to a prescribed cooling rate in the troposphere ($T > 207.5$ K), and Newtonian relaxation in the stratosphere to 200 K on a time scale of 5 days (Pauluis and Garner, 2006). This highly idealized radiation scheme allows us to focus on the effects of imposed

atmospheric heating without complicating factors such as water vapor feedback and cloud radiative effect. Sub-grid diffusion is parameterized following the YSU boundary layer scheme (Hong et al., 2006) in the vertical direction, and the Smagorinsky two-dimensional scheme in the horizontal. The single-moment Purdue-Lin microphysics scheme (Lin et al., 1983; Rutledge and Hobbs, 1984; Chen and Sun, 2002) contains six species: water vapor, cloud water, cloud ice, rain, snow and graupel. Surface sensible and latent heat fluxes (SH and LH, respectively; both in W m^{-2}) are calculated using the bulk aerodynamic formula with a constant (0.005 kg m^{-2} s^{-1}) comprised of a drag coefficient of 0.001, a near-surface air density of 1 kg m^{-3} and a constant near-surface wind speed of 5 m s^{-1}:

$$SH = 0.005 c_p (T_s - T_a) \tag{2.1}$$

$$LH = 0.005 L (q_{sat} - q_a), \tag{2.2}$$

where c_p is the specific heat capacity of dry air (1004.5 J kg^{-1} K^{-1}), L the latent heat of vaporization of water in typical atmospheric conditions (2.5×10^6 J kg^{-1}), T_s surface temperature, T_a the lowest model level (or near-surface) temperature, q_{sat} the saturated water vapor mixing ratio at T_s, and q_a the lowest model level water vapor mixing ratio. As T_s and q_{sat} are fixed, the simplifications made in Equations 2.1 and 2.2 imply that the only way to alter SH and LH is by adjusting near-surface boundary layer temperature and humidity (T_a and q_a).

All simulations are performed on a doubly-periodic domain of 96×96 gridpoints with a horizontal spacing of 2 km. There are fifty vertical levels, nine of which are in the lowest 1 km. Domain-average winds are relaxed to zero on a time scale of 2 hours to prevent wind shear from developing, similar to Tompkins and Semie (2017). The surface temperature is set at 301.15 K, making the lower boundary conditions horizontally homogenous. The two control simulations with different microphysical

assumptions (to be discussed) are initialized with a warm bubble and are first performed for 240 model days; the perturbation simulations are branched off day 180 of their respective controls and last 60 model days. The last 20 days of hourly-mean outputs from each simulation are analyzed. We use five consecutive, non-overlapping 20-day periods (days 220-320), obtained by extending the control simulations, for assessing the noise level of any given variable. The difference between a control and a perturbation is considered significant if it rises above the noise level.

The prescribed radiative cooling rate is at the default value (-1.5 K day^{-1}) in the first base case (BASE). It is reduced by half to -0.75 K day^{-1} throughout the troposphere in HEAT. To isolate the boundary layer response to free-tropospheric heating, we separate the uniform radiative heating into two complementary differential heating cases: halving the cooling only above 850 hPa (A850) and below (B850). To assess the importance of rain re-evaporation in communicating free-tropospheric heating to the boundary layer, we repeat all the simulations with a model configuration in which the rate of rain re-evaporation in the cloud microphysics scheme is reduced by an factor of 10. The four additional cases are denoted by adding an asterisk to the original case names. We will refer to the two groups of experiments as full and partial re-evaporation, respectively. Throughout this chapter, a response to heating is denoted with a δ.

2.3 Results

2.3.1 Domain-average responses

Through the energetic constraint, the radiative heating alters surface fluxes, thereby affecting temperature, moisture, and precipitation. We begin by examining a set of key domain-average quantities and their changes resulting from forced heating (Table 2.1). Relative to BASE, the tropospheric radiative cooling (from the surface to 200

Table 2.1: Domain-average tropospheric radiative cooling (RA, W m^{-2}), surface sensible heat flux (SH, W m^{-2}), surface latent heat flux (LH, W m^{-2}), near-surface temperature (T_a, K) and water vapor mixing ratio (q_a, g kg^{-1}), precipitation (P, mm day^{-1}), and changes in the perturbation cases. All changes are significant.

	RA	SH	LH	T_a	q_a	P
BASE	-145	19.5	127	297.3	14.4	4.4
δHEAT	72	-14.7	-54.9	2.9	4.3	-1.9
δA850	59	-11.1	-45.8	2.2	3.5	-1.6
δB850	13	-4.2	-7.5	0.8	0.6	-0.3
BASE*	-145	9.4	137	299.3	13.6	4.7
δHEAT*	72	-9.3	-61.1	1.9	4.8	-2.1
δA850*	59	-4.7	-53.3	0.9	4.1	-1.8
δB850*	13	-6.3	-5.6	1.3	0.5	-0.2

hPa) is cut by half in HEAT. The resulting net heating is balanced by reducing both surface sensible and latent heat fluxes with a ratio of δSH to δLH at 0.27, which differs significantly from the Bowen ratio in BASE (0.15), suggesting that radiative cooling plays a role in determining the Bowen ratio. Consistent with Equations 2.1 and 2.2, the near-surface temperature (T_a) increases by 2.9 K, while the near-surface water vapor mixing ratio (q_a) increases by 30%. [The latter is greater than what one would expect from the Clausius-Clapeyron relation and assuming constant relative humidity (RH) (about 20%). Indeed, the near-surface RH increases by about 10% (relative change) to make up the difference.] More quantitatively, according to Equations 2.1 and 2.2, the changes in SH (δSH) and LH (δLH) can be written as $-0.005 c_p \delta T_a$ and $-0.005 L \delta q_a$, respectively, meaning that one can tie the near-surface temperature and humidity changes directly to the imposed heating. It is, nonetheless, unclear what determines the relative contributions of surface sensible and latent heating, a point to which we will return in Section 2.4. The domain-average precipitation (equivalent to latent heat flux) reduces by 43%, which is less than the relative decrease in radiative cooling.

For the two differential heating cases, the column-integrated change in radiative cooling in A850 is about 4.5 times of that in B850. This is understandable as it

is approximately proportional to the pressure depth to which the perturbations are applied [i.e. (850-200)/(1000-850)]. The ratio is 2.8 for δT_a, and 5.8 for δq_a and δP, suggesting that elevated heating is less effective at modifying surface sensible flux (near-surface temperature), but more so at altering surface latent heat flux (near-surface precipitation and moisture). It is still somewhat surprising to see that the free-tropospheric heating has a substantial warming effect on the near surface, especially given that most of the sensible heating from the YSU scheme is placed in the boundary layer. This suggests that when conjecturing a quantitative theory for the partitioning of surface sensible and latent heating, one has to take into account the vertical distribution of atmospheric radiative heating and the coupling between the free troposphere and boundary layer (to be investigated in Section 2.3.3).

Relative to BASE, the decreased microphysical cooling in BASE* warms the boundary layer by 2 K, reducing the surface sensible heat flux. The tropospheric energy balance is restored by increasing the surface latent heat flux, which is consistent with lower boundary layer humidity. The response of surface sensible heat fluxes to the heating in HEAT* is much smaller (-9.3 W m^{-2}) than that of HEAT (-14.7 W m^{-2}). Note that the surface sensible heat flux is close to zero in HEAT*. As compared to the full re-evaporation counterparts, elevated heating becomes less effective in inducing near-surface warming (1.9 K in HEAT* versus 2.9 K in HEAT, and 0.9 in A850* versus 2.2 K in A850). Consequently, the reduction in latent heat (precipitation) is more pronounced in the partial re-evaporation cases with free-tropospheric heating.

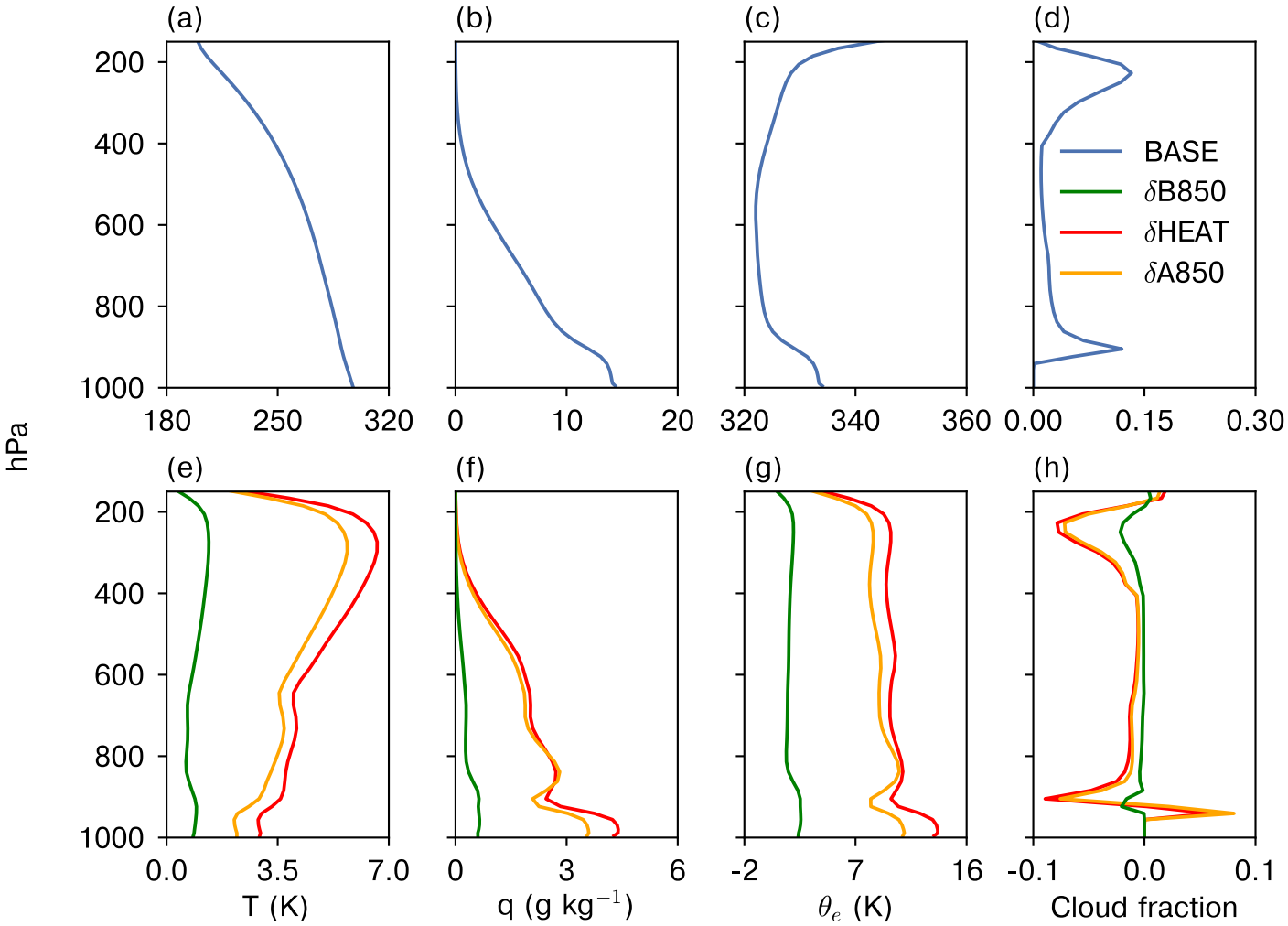


Figure 2.1: Vertical profiles of (a) temperature (T, K), (b) water vapor mixing ratio (q, g kg^{-1}), (c) equivalent potential temperature (θ_e, K), (d) cloud fraction in BASE. (e-h) Changes in (a-d) due to heating (prefixed by δ) in HEAT, A850, and B850. All changes rise significantly above the noise level.

Figure 2.1 shows the vertical profiles of temperature (T), water vapor mixing ratio (q), equivalent potential temperature (θ_e) and cloud fraction in BASE (top row) and their changes in the perturbation cases (bottom row). The temperature structure in RCE follows that of a moist adiabat (Figure 2.1a), and to first order sets the vertical structure of water vapor (Figure 2.1b) in the free troposphere. θ_e shows a first baroclinic mode structure, with a minimum at around 500 hPa (Figure 2.1c). Under heating, the near-surface warming extends throughout the troposphere, with appreciable amplification in the middle and upper troposphere, as a consequence of moist adiabatic control (Figure 2.1e). In contrast, the accompanying increase in q is bottom-heavy, as in the control (Figure 2.1f). θ_e increases rather uniformly throughout the troposphere (Figure 2.1g). As in Wang and Sobel (2011), a grid is defined as cloudy if the total cloud condensate (water and ice) exceeds 0.005 g kg^{-1}. Cloud fraction has two maxima in the vertical direction (Figure 2.1d). One can regard the lower one approximately as the lifting condensation level (LCL). It becomes lower in HEAT as the near-surface RH increases (Romps, 2017). Note that the LCL remains above 965 hPa (the boundary layer top used in this paper) in all experiments. The cloud fraction in HEAT is approximately half of that in BASE (Figures 2.1d,h). The domain-mean responses are qualitatively similar in the other simulations (e.g. Figure 2.4). Next, we explore connections between domain-mean quantities and precipitation intensity.

2.3.2 Precipitation intensity

In this section we explore if the reduction in domain-mean precipitation shifts the intensity distribution of precipitation. The domain-average precipitation of the events at gridpoints where the hourly precipitation rate r exceeds a threshold value r_t (in mm day^{-1}), is denoted as $p(r{>}r_t)$ (Figure 2.2a). By definition, $p(r{>}0)$ is the domain-average precipitation of all events (P), which was discussed in Section 2.3.1. Figure

2.2b shows $p(r > r_t)$ normalized by the domain-mean precipitation P. In BASE, the top 50% of precipitation have precipitation rates exceeding 210 mm day^{-1}. Despite the substantial (43%) reduction in HEAT, the top 50% of precipitation falls with precipitation rates exceeding 320 mm day^{-1} in HEAT. In this sense, the reduction in precipitation is realized through a reduction in weak, rather than strong, events.

Figure 2.2c plots the hourly precipitation rate against 500-hPa (nearest model level) vertical velocity (w) for all gridpoints in BASE and HEAT. Both quantities are strongly correlated, especially for the events with appreciable positive (upward) w (greater than ~ 0.1 m s^{-1}); a linear regression through the origin yields $R = 0.66$ for BASE and HEAT. Yet, the slope (k) for HEAT is 34% larger than for BASE, meaning that the same ascending motion generates considerably more precipitation in the former. This is consistent with the 30% increase in the average near-surface water vapor mixing ratio (q_a) as discussed above. One may also gather that vertical velocity is generally weaker in HEAT than in BASE.

Figure 2.2d shows the probability of w exceeding a threshold w_t for $w_t > 0.1$ m s^{-1}, or $\int_{w_t}^{\infty} \mathcal{P}(w)dw$, where $\mathcal{P}(w)$ is the probability density function of w. Ascents are relatively rare; on average only 1.0% of the grids have w larger than 0.1 m s^{-1}. The probability decreases by more than three orders of magnitude as w_t increases to 5 m s^{-1}. In HEAT, ascending motions become even less likely across the entire range of w_t, affirming the impression of weaker ascents from Figure 2.2c. The idealized calculations of Pendergrass and Gerber (2016) suggests that a shift towards strong events is accompanied by increased skewness in $\mathcal{P}(w)$. Indeed, skewness increases by 22% in HEAT (not shown).

To better understand the different responses of strong versus weak events, we write the domain-average precipitation of the events with w greater than a certain positive value w_t [$p(w > w_t)$, w_t in m s^{-1}] approximately as:

$$p(w > w_t) = k \int_{w_t}^{\infty} w\mathcal{P}(w)dw. \tag{2.3}$$

$p(w > 0.1)$ is 2.3 mm day^{-1} in BASE, which accounts for slightly more than half of the total precipitation (Figure 2.2e). The remaining is associated with very weak ascents (less than 0.1 m s^{-1}) and descents. $p(w > w_t)$ is consistently smaller in HEAT for w_t greater than 0.1 m s^{-1}, making it easier to interpret the difference between the two cases than in terms of $p(r)$ (Figure 2.2a). By assuming that k is independent of $\mathcal{P}(w)$, one can linearly decompose the difference $[\delta p(w > w_t)]$ into the thermodynamic (δk) and dynamic ($\delta\mathcal{P}$) terms:

$$\delta p(w > w_t) \approx \delta k \int_{w_t}^{\infty} w\mathcal{P}(w)dw + k \int_{w_t}^{\infty} w\delta\mathcal{P}(w)dw. \tag{2.4}$$

Figure 2.2f indicates that although neglecting the nonlinearities underestimates the difference between BASE and HEAT, it does capture some important characteristics of the simulations [e.g. $\delta p(w > w_t)$ generally decreases as w_t increases]. While the thermodynamic effect owing to higher near-surface water vapor mixing ratio acts to enhance precipitation, the dynamic effect in the form of weaker ascents tends to lower precipitation. As the dynamic effect outweighs the thermodynamic effect, the net result is a reduction of precipitation at a given w_t. A similar cancellation is seen when the full vertical velocity distribution is included (e.g. O'Gorman and Schneider, 2009; Fildier et al., 2017) (not shown). Additional experiments with doubling domain size, increasing SSTs (+10 K) and halving the amount of prescribed heating confirm the shift towards strong precipitation and the compensation between thermodynamic and dynamic effects (not shown). The cancellation between the thermodynamic and dynamic effects for strong events implies that energy balance is maintained by preferentially reducing weak events. The key role of boundary layer moisture in maintaining

the intensity of strong precipitation events motivates an analysis of the surface sensible versus the latent heat response.

2.3.3 Boundary layer energy balance

In equilibrium, the processes that influence surface sensible heat fluxes (SH) are encapsulated in the boundary layer energy balance: $SH + RA_b + RE + EX = 0$. SH is the main energy source for the boundary layer in BASE (Figure 2.3a). Additional heating is realized through the exchange of sensible heat with the free troposphere, either explicitly resolved or parameterized at the sub-grid scale (EX), which is inferred as a residual. The sink terms are radiative cooling (RA_b) and re-evaporative cooling (RE), calculated by integrating the radiative and microphysical heating rates over the boundary layer. The latter takes place as rain falls through the unsaturated boundary layer and is thus microphysical in nature. Somewhat surprisingly, the magnitude of re-evaporative cooling is larger than that of radiative cooling, which is often presumed to be the dominant sink term.

Figure 2.3b summarizes how the individual terms vary in the perturbation cases. Although imposed radiative heating is clearly present in HEAT, the main balance is between SH and RE, both of which decrease substantially in magnitude. As A850 and B850 add up roughly to HEAT, one can see that the boundary layer radiative heating is balanced almost entirely by lowering SH, as is the case in B850. The large reduction in RE seen in HEAT can be attributed to the radiative heating above 850 hPa, and amounts to a warming effect on the boundary layer. This is consistent with lower SH and higher near-surface temperature (Table 2.1). The changes in EX are small compared to those in SH.

One can define precipitation efficiency (ϵ) as the ratio of precipitation (P) over column-integrated condensation (C) (Zhao, 2014), with a value of 0.33 in BASE. Column-integrated re-evaporation (E), which is equal to the difference between C

and P (i.e. $C - P$), can be written as $P(1-\epsilon)/\epsilon$. As ϵ is little changed across the cases (within 0.01), the fractional changes in column-integrated re-evaporation and precipitation are similar (Figure 2.5). Note that the scaling of Lutsko and Cronin (2018) for the fraction of precipitation that is re-evaporated need not explain most of the changes in re-evaporation (Section 2.A).

The partial re-evaporation simulations allow us to further assess the importance of re-evaporation. Despite having the same boundary layer radiative cooling as BASE, the magnitudes of the surface sensible heating and the exchange term are much reduced in BASE*, presumably due to the suppressed re-evaporative cooling (Figure 2.3c). The response to free-tropospheric heating is also muted considerably in A850*; the resulting reduction in SH is less than half of that in A850 (Figure 2.3d). The same is true for near-surface temperature T_a (Table 2.1). This reaffirms the importance of re-evaporative cooling in communicating the effect of free-tropospheric heating to the boundary layer and surface fluxes. In summary, heating the free-troposphere reduces mean precipitation and rain re-evaporation, leading to boundary layer warming.

2.4 Discussion and summary

It is clear from the above results that the vertical distribution of radiative heating is key to determining the relative roles of surface sensible and latent heat adjustments in re-establishing the tropospheric energy balance. In particular, re-evaporative cooling is the main process through which the effect of free-tropospheric heating can be felt by the boundary layer. Thus, re-evaporation has to be considered explicitly in any attempt to develop a quantitative theory of the surface sensible heat flux response to atmospheric heating.

If one assumes that the free-tropospheric energy balance can be approximated as radiative cooling balancing out latent heating, it follows that the fractional change of precipitation is equal to that of the free-tropospheric radiative cooling ($\delta P/P = \delta RA_f/RA_f$). As discussed in Section 2.3.3, the fractional changes of the boundary layer re-evaporative cooling is approximately equal to that of precipitation. Thus, δRE can be written as $\alpha\delta RA_f$, where α is the ratio of RE to RA_f in the control case. If the exchange term does not vary appreciably with imposed heating, the boundary layer energy balance leads to the following expression of the surface sensible heat flux change:

$$\delta SH = -\delta RA_b - \alpha\delta RA_f. \tag{2.5}$$

Furthermore, its latent heat counterpart can be derived from the tropospheric energy balance:

$$\delta LH = (\alpha - 1)\delta RA_f. \tag{2.6}$$

This constitutes a predictive theory of δSH and δLH in response to δRA_b and δRA_f as α (0.11 in BASE) depends only on values in the control experiment. The predicted δSH (solid lines in Figure 2.3) is in good agreement with the simulations (bars). According to this theory, free-tropospheric heating reduces latent heating more than surface sensible heating as long as α is smaller than 0.5. Also, boundary layer heating decreases surface sensible heating only.

The approximation used in Takahashi (2009) and Cronin (2013) can be viewed as a special case of Equation 2.5 with $\alpha = 0$:

$$\delta SH = -\delta RA_b. \tag{2.7}$$

The partial re-evaporation experiments allow us to test the theory for a small value of α (0.02 in BASE*) that approaches this special case. Indeed, the predictions from Equations 2.5 and 2.7 are much closer in the partial re-evaporation than full re-evaporation experiments. In other words, the $\alpha \delta RA_f$ term in Equation 2.5 greatly improves the accuracy of the predicted δSH by incorporating the effect of re-evaporation in coupling the boundary layer and the free-troposphere. To generalize our results to the full climate response, one must account for changes in precipitation efficiency under surface warming (Lutsko and Cronin, 2018). The response to heating might be altered in the presence of a large-scale circulation (e.g. Wing and Cronin, 2016; Lutsko and Cronin, 2018).

In summary, imposed radiative warming reduces domain-average precipitation (evaporation) by increasing boundary layer water vapor, a thermodynamic effect that tends to enhance precipitation rate at a given vertical velocity. This effect opposes the weakening of ascents (a dynamic effect), resulting in no significant change in the precipitation from strong events. The decrease in domain-average precipitation is realized mainly through weak events. A key finding is that free-tropospheric radiative heating affects the boundary layer primarily by weakening the re-evaporative cooling. This insight leads to a predictive theory of the surface latent and sensible heat flux changes caused by radiative heating.

2.5 Acknowledgments

Shuguang Wang provided the source code for the WRF model and valuable advice. The analysis was aided by the "aospy" package. XRC thanks Hailey Shin, Usama Anber, Spencer Clark, Leo Donner and Lucas Harris for helpful discussions. NJ is supported by a Harry Hess fellowship. We thank Leo Donner, Levi Silvers, and the two anonymous reviewers for constructive reviews.

2.A Frameworks for re-evaporation

We examine the relative importance of changes in domain-mean precipitation (P) versus changes in the fraction of precipitation that is re-evaporated (β) for understanding changes in column-integrated re-evaporation (E) under heating in our experiments. In Section 3.3, we explained that $E = (\frac{1}{\epsilon} - 1)P$, where ϵ is the precipitation efficiency. Since changes in $\frac{1}{\epsilon} - 1$ are small (less than 11%) in our experiments, $\frac{\delta E}{E} \approx \frac{\delta P}{P}$ (circles in Figure 2.5a). In other words, P is of leading order importance in understanding changes of E in our heating simulations.

Separately, Lutsko and Cronin (2018) (henceforth LC) proposed that β scales with the saturation deficit $1 - RH$ and the terminal fall speed w_f. This scaling can be linearized as:

$$\frac{\delta\beta}{\beta} = \frac{\delta(1 - RH)}{1 - RH} - \frac{\delta w_f}{w_f}. \tag{2.8}$$

Figure 2.5b shows the changes in β against the changes predicted by Equation 2.8. Following LC, $\beta = \frac{E}{E+P}$, and both RH and w_f are weighted by the amount of precipitating condensates at each level. Equation 2.8 holds reasonably well in our experiments; the best-fit line with no intercept has $R = 0.85$.

Since β is only one factor that influences E, changes in β need not be the leading explanation for changes in E. The crosses in Figure 2.5a illustrate that the RHS of Equation 2.8 underestimates the changes in re-evaporation in our experiments by more than a factor of two. Comparing the two scalings (circles versus crosses) confirms that P plays a larger role than β in influencing E in our experiments.

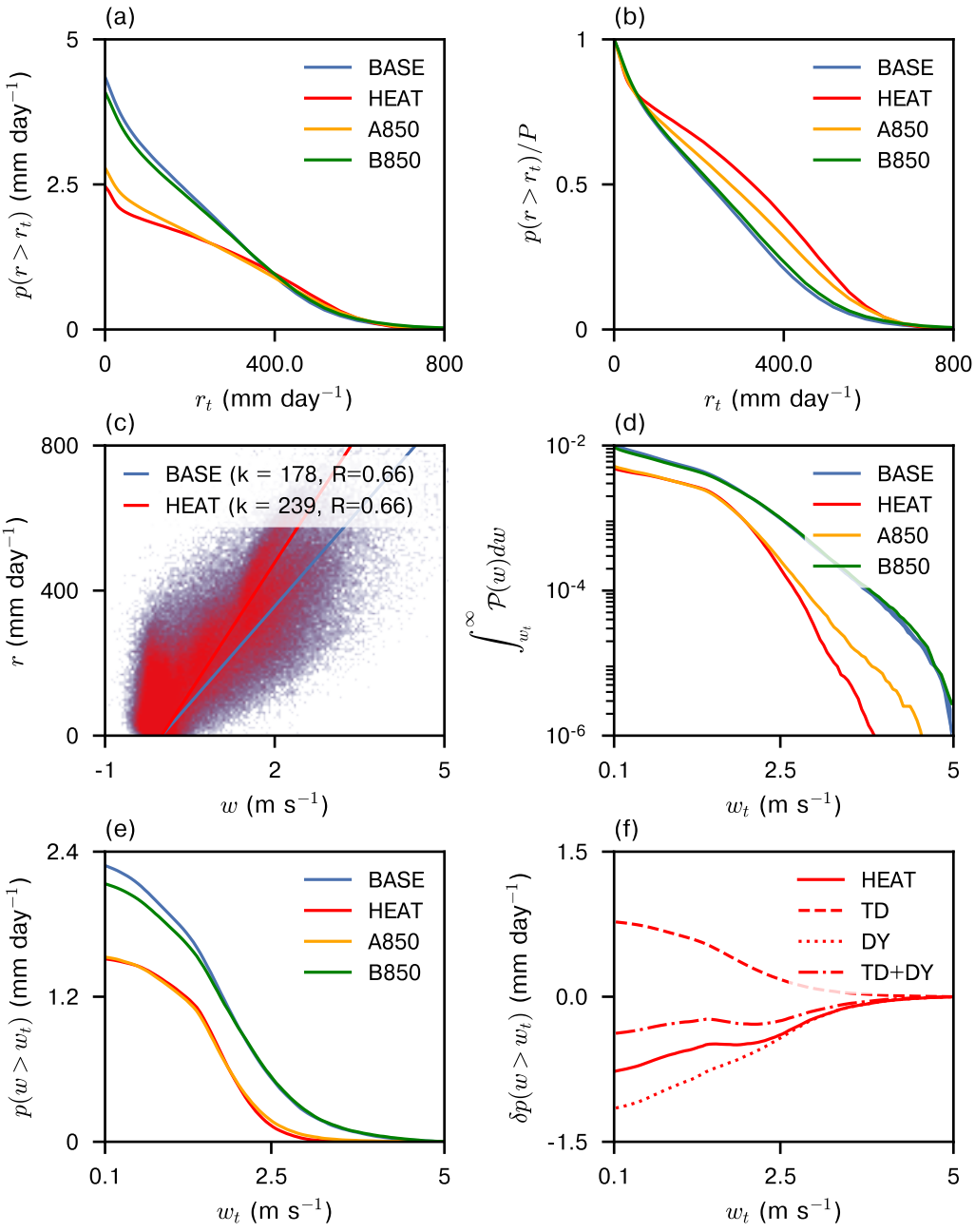


Figure 2.2: (a) The domain-average precipitation ($p(r{>}r_t)$, mm day^{-1}) of the events whose hourly precipitation rates exceed r_t (mm day^{-1}) in the full re-evaporation experiments. (b) $p(r{>}r_t)$ normalized by domain-mean precipitation P. (c) The scatter plot of r (mm day^{-1}) against 500-hPa vertical velocity (w, m s^{-1}) for BASE and HEAT. The solid lines are the best-fit lines with zero-intercept for $w > 0.1$ m s^{-1}. (d) The probability of w exceeding a threshold w_t (m s^{-1}), or $\int_{w_t}^{\infty}\mathcal{P}(w)dw$, for $w_t > 0.1$ m s^{-1}. (e) The domain-average precipitation ($p(w{>}w_t)$, mm day^{-1}) of the events where w exceeds w_t, estimated with Equation 2.3. (f) The difference in $p(w{>}w_t)$ (m s^{-1}) between BASE and HEAT, and its thermodynamic and dynamic components and their sum, estimated with Equation 2.4.

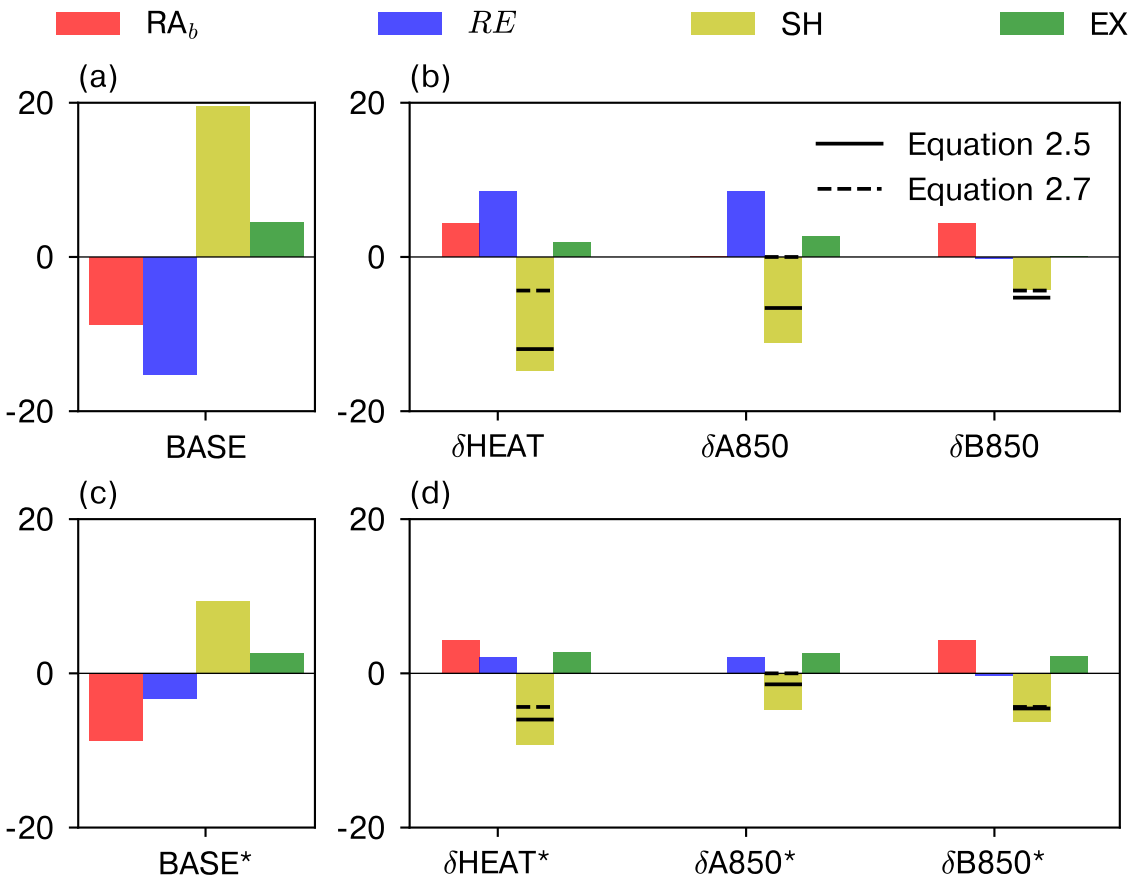


Figure 2.3: (a) The individual terms in the boundary layer energy balance (W m^{-2}) in BASE: surface sensible heating (SH), radiative cooling (RA_b), re-evaporative cooling (RE) and the exchange of sensible heat with the free troposphere (EX). (b) Changes in HEAT, A850 and B850. (c,d) Same as (a,b), but for the partial re-evaporation cases. The solid and dashed lines denote the change in SH calculated from the predictive theories that include (Equation 2.5) and exclude (Equation 2.7) the effect of re-evaporative cooling, respectively.

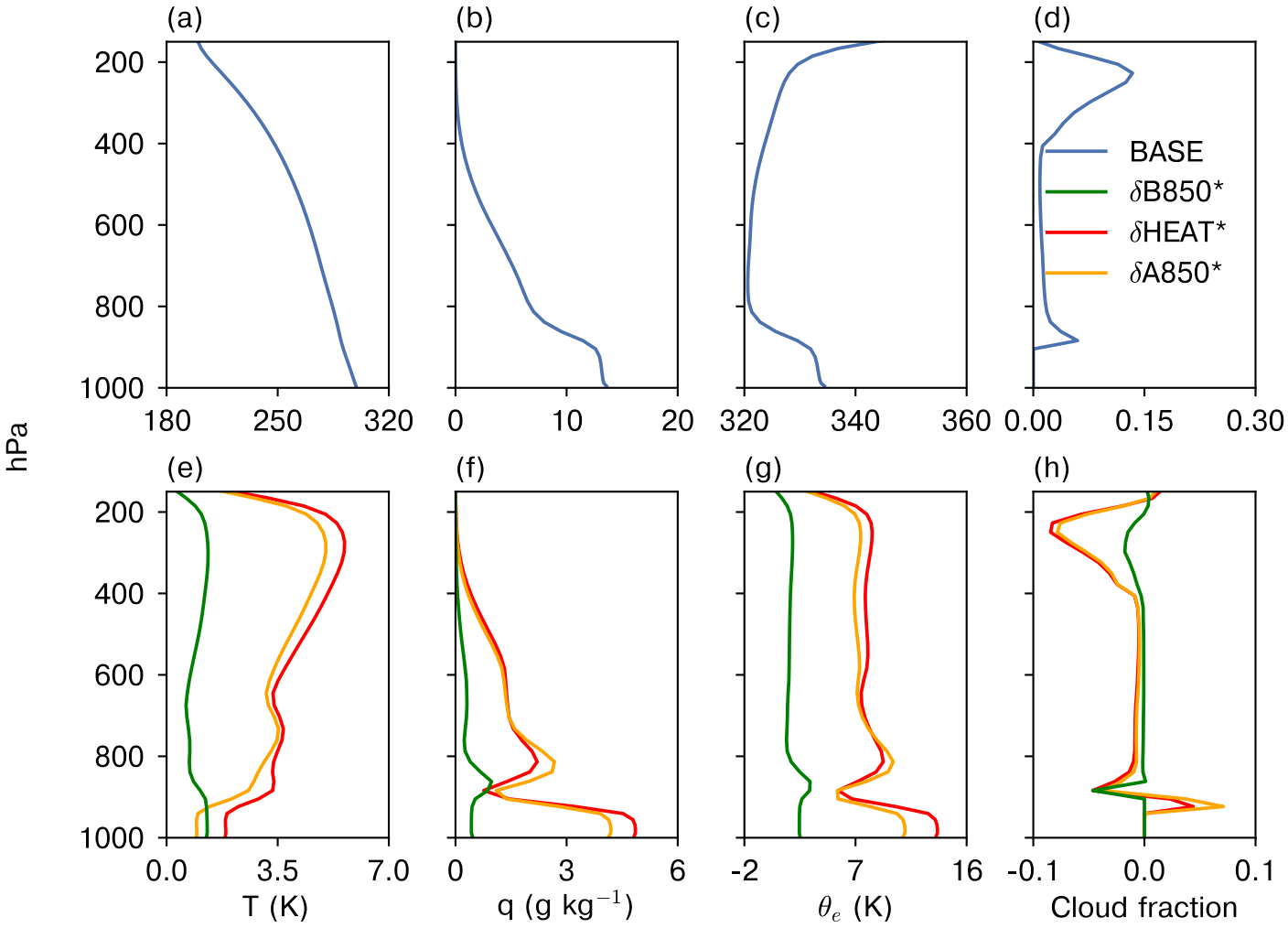


Figure 2.4: As in Figure 1, but for BASE*, HEAT*, A850*, and B850*.

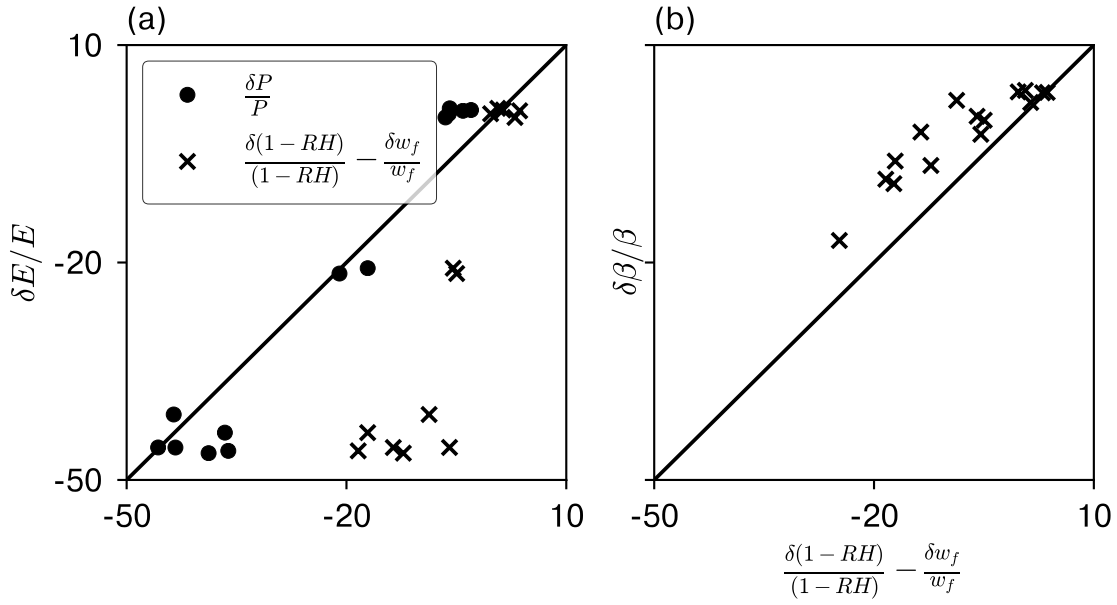


Figure 2.5: Scatter plots related to frameworks for changes in re-evaporation. The solid lines are the one-to-one lines. (a) Fractional changes in re-evaporation (E) against fractional changes in precipitation (P) (circles, best-fit slope with no-intercept of 1.1 and $R = 0.97$) and the sum of fractional changes in $1 - RH$ and the fall velocity (w_f), calculated as in Lutsko and Cronin (2018) (crosses, best-fit slope with no intercept of 2.8 and $R = 0.86$). (b) Fractional changes of the re-evaporation efficiency (β) against the sum of fractional changes in $1 - RH$ and the fall velocity (the same quantity as in (a)). The best-fit slope with no intercept is 0.47, with $R = 0.85$.

Chapter 3

On the role of liquid microphysical processes in convective invigoration

3.1 Introduction

Having discussed the effects of aerosols on atmospheric radiation in Chapter 2, we now turn to the aerosol influence on microphysical processes. The microphysical effects of aerosols on convection are thought to occur through pathways involving both ice and liquid processes. A commonly referenced mechanism (Rosenfeld et al. (2008), see also Williams et al. (2002); Andreae et al. (2004)) posits that increased aerosol concentrations increase cloud droplet number concentrations of smaller drops, which delays the formation of rain. It is thought that this would bring more cloud water above the freezing level, releasing additional latent heat and invigorating convection. Stevens and Feingold (2009) present a liquid variant of this argument, suggesting that the delayed precipitation increases evaporation at the cloud-top, destabilizing the atmosphere and favoring convection. Changes in condensate evaporation can also affect cold pool strength and the strength of subsequent convection (e.g. Tao et al., 2007; Morrison, 2012; Tao et al., 2012). Recently, Fan et al. (2018) suggested

that ultrafine (smaller than 50 nm) aerosol particles can be activated into cloud droplets, making it possible to condense more supersaturated water. Given that the enhancement of upper level condensational heating was not significant in their sensitivity tests, they argue that the convective invigoration in their experiments occurs via a warm-phase rather than a cold-phase pathway.

Generally speaking, there is no consensus on how aerosols may affect convection, with different case studies suggesting either strengthening (e.g. Fan et al., 2018) or weakening (e.g. Morrison, 2012). Making comparisons across different case studies is not straightforward, given that environmental factors such as wind shear (Fan et al., 2009) and radiative effects (e.g. Fan et al., 2015) can alter the eventual convective response. The setting of radiative-convective equilibrium (RCE) allows us to understand which processes are of importance to the climate state in a simple framework. For example, van den Heever et al. (2011) found an increase in the frequency of updrafts in response to increased aerosol concentrations. In a follow-up study focusing on deep convective cloud properties, Storer and van den Heever (2013) showed that changes in latent heat from the freezing of cloud water are not the largest contributors to the latent heat budget, suggesting that latent heat from freezing might not be of leading order importance for understanding convective invigoration, at least in RCE. This motivates the present microphysical sensitivity study in the setting of RCE with prescribed radiative cooling to isolate the dominant mechanism responsible for convective invigoration.

3.2 Methods

3.2.1 Model

The RCE configuration is almost identical to that of Chapter 2, with radiative cooling prescribed at -1.5 K day^{-1} in the troposphere (T $>$ 207.5 K) and following Newtonian

relaxation to 200 K on a time scale of 5 days, as in the BASE case in Chapter 2. By prescribing the radiative cooling, we eliminate a major confounding factor of aerosol-radiation interactions on the convective response. The only difference is the use of the double-moment Morrison scheme (Morrison et al., 2009). By predicting both the number and mass mixing ratio of hydrometeors, a double moment scheme captures more degrees of freedom of the microphysical response to aerosols.

The Morrison scheme can be set to only consider liquid (or warm rain) microphysics. In that configuration, condensation of water vapor (q_v) to cloud water (q_c) takes place via saturation adjustment. Re-evaporation of cloud droplets occurs only in subsaturated conditions, and is limited by the availability of cloud water. Rain (q_r) is converted to vapor by rain re-evaporation. The conversion of cloud water to rain occurs by both autoconversion and accretion, parameterized as $1350 q_c^{2.47} N_c^{-1.79}$ and $67(q_c q_r)^{1.15}$, with units of kg kg^{-1} s^{-1} (Khairoutdinov and Kogan, 2000). Here, q_c and q_r are in kg kg^{-1} and N_c is in cm^{-3}. Autoconversion is the only microphysical process among both ice and liquid processes that is directly affected by cloud droplet number concentrations.

3.2.2 Experiments

Four pairs of BASE ($N_c = 100$ cm $^{-3}$) and BASE* ($N_c = 1000$ cm $^{-3}$) simulations are performed, with different microphysical assumptions. In FULL, the default Morrison scheme configuration is used, with full ice and liquid microphysics, while LIQ involves only liquid microphysics. In addition to shutting off ice microphysics, the formula used for computing the rates of re-evaporation of cloud water and rain are multiplied by 0.1 in the CE and RE experiments, respectively. We collectively refer to LIQ, CE and RE as liquid microphysics cases. The BASE simulations are initialized from a warm bubble and are first performed for 240 model days. The output at day 180 of the BASE experiment is used to initialize a BASE* experiment that is run for 60 days.

We analyze the last 20 days of hourly-mean output from each simulation. The noise level of a given variable is quantified using five consecutive, non-overlapping 20 day periods (days 220-320) obtained by extending the BASE simulations. The response to higher droplet number concentrations (i.e., BASE* minus BASE) is denoted by a δ.

3.2.3 Definition of convective mass flux

For the purpose of quantifying convective invigoration, we use convective mass flux (M_c) from updrafts as our main metric for convection (e.g. Lebo et al., 2012; Morrison, 2012). Updrafts are vertical velocities averaged over cloudy (cloud condensate exceeding 0.005 g kg^{-1}, e.g. Wang and Sobel, 2011) exceeding 1 m s^{-1} (e.g. Robe and Emanuel, 1996). M_c is the sum of the mass flux from all updrafts.

3.3 Domain-mean vertical responses

In this section, we describe the responses of key microphysical, dynamic and thermodynamic quantities to the microphysical perturbations imposed by our experiments. Figure 3.1 illustrates the influence of the microphysical perturbation on condensates. In all BASE cases, the distribution of cloud water (q_c, Figure 3.1a) is similar in the lower and mid troposphere, with a peak at about 900 hPa. In the upper troposphere, the high clouds are comprised by ice (dashed) in FULL and cloud water in the liquid microphysics cases. Compared to the liquid microphysics cases, q_c is highest in FULL. The distribution of precipitating condensates (q_p, Figure 3.1b) is similar in the lower troposphere, with a peak at around 700 hPa. Above 600 hPa, the solid condensates (snow and graupel) dominate the precipitating condensates in FULL (dashed). As is the case for q_c, q_p is highest in FULL. Cloud fraction (calculated as in Chapter 2) has two maxima. The cloud fraction in FULL is lower than that of the liquid

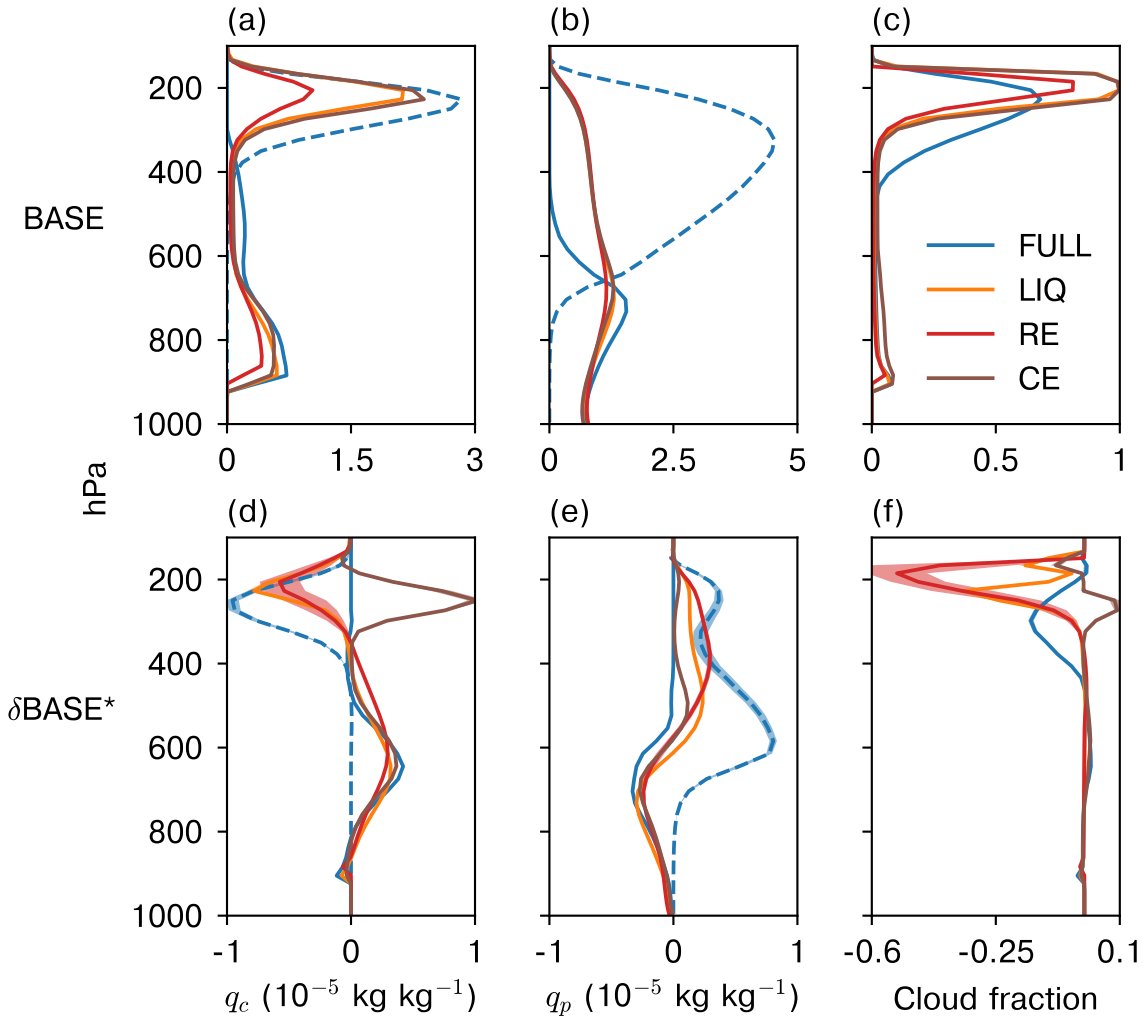


Figure 3.1: Domain-average vertical profiles of (a) cloud liquid (solid) and ice (dashed) condensates (q_c, 10^{-5} kg kg^{-1}), (b) precipitating liquid (solid) and ice (dashed) condensates (q_p, 10^{-5} kg kg^{-1}) and (c) cloud fraction (unitless) in the BASE experiments. Cloud fraction is calculated using a condensate and vertical velocity threshold as in Chapter 2. (d-f) Changes in (a-c) due to δBASE*. The shading in (d-f) represents the noise in BASE.

microphysics cases, suggesting that q_c is more uniformly distributed in the domain in the liquid microphysics cases as compared to FULL.

In all δBASE* cases (Figure 3.1d), there is an increase in cloud condensate below 500 hPa. At 200 hPa, there is a decrease in q_c in all cases except CE. There is also a decrease in q_p below 700 hPa (Figure 3.1e). The increased cloud water and reduced rain concentrations are consistent with the nature of the perturbation, which

suppresses the conversion of cloud water to rain. The influence on cloud fraction (Figure 3.1f) is mainly in the upper troposphere, with a decrease in cloud fraction in all cases except in δCE*. The changes in upper-tropospheric cloud fraction have similar sign to the changes in q_c.

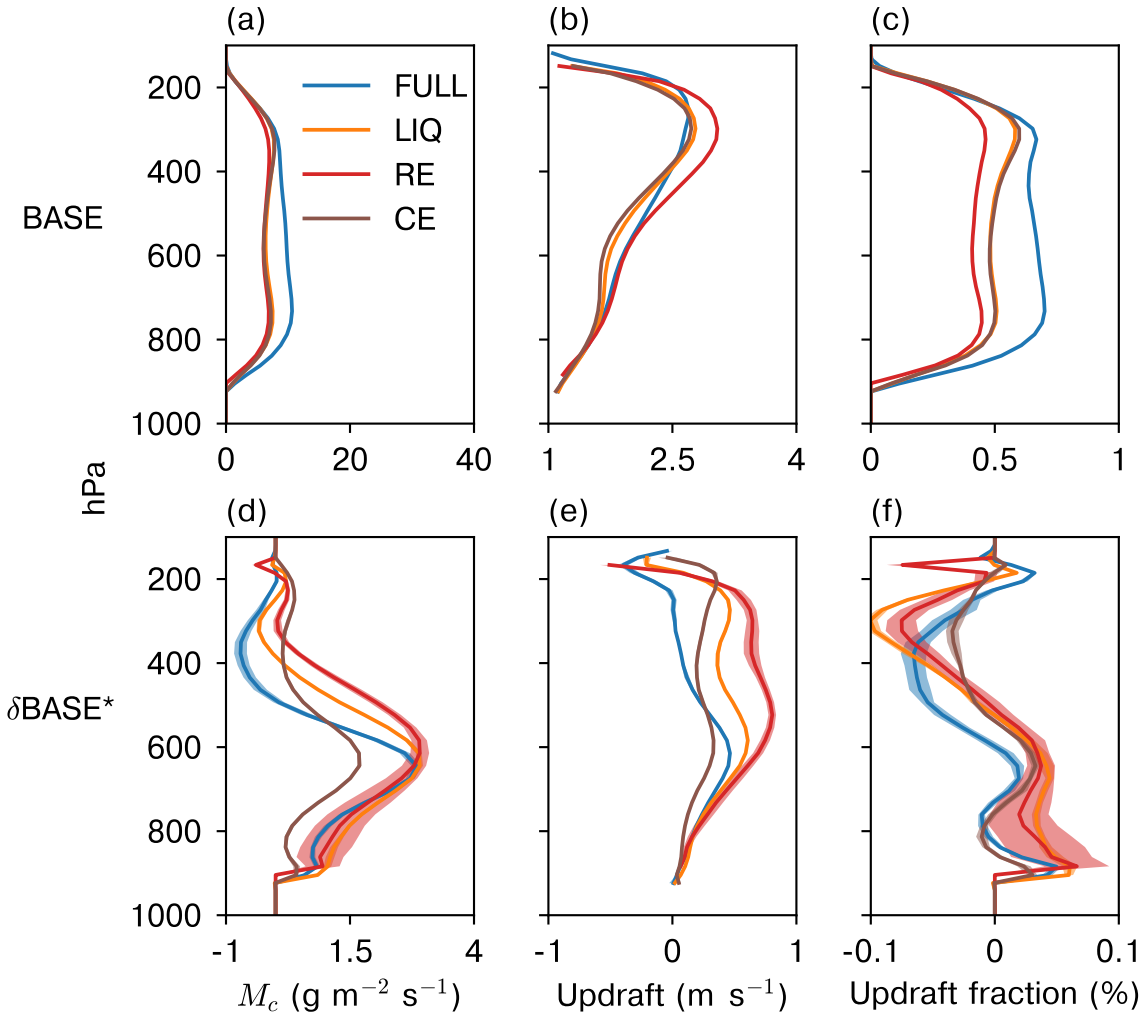


Figure 3.2: Domain-average vertical profiles of (a) convective mass flux (M_c, g m^{-2} s^{-1}), (b) updraft vertical velocity (m s^{-1}), and (c) updraft fraction (%) in the BASE experiments. (d-f) Changes in (a-c) due to δBASE*. The shading in (d-f) represents the noise in BASE.

Next, we turn to the influence of the microphysical perturbations on convective dynamics. Across the BASE cases, the convective mass flux (M_c, Figure 3.2a) is largest in FULL. The contributions of the vertical velocity of updrafts (updraft in-

tensity) and updraft area to the convective mass flux are shown in Figures 3.2b and c, respectively. In the case of FULL versus LIQ, the percentage increase in convective mass flux at 600 hPa (53%) is due mostly to an larger updraft fractional area (40%) rather than updraft intensity (10%). The small differences in convective mass flux between the liquid microphysics cases (less than 10% at 600 hPa) can be a result of compensating differences in updraft area and intensity. For example, RE has both the largest updraft intensity and smallest updraft area among all BASE cases. Note that convection remains unaggregated across all simulations.

Convective invigoration is seen in both FULL and LIQ (Figure 3.2d) in δBASE*, with the peak of the increase in M_c at around 600 hPa. Relative to LIQ, weakening re-evaporation of cloud droplets (CE) mutes the increase of convective mass flux by 56% at 600 hPa, while weakening re-evaporation (RE) does not significantly alter convective mass flux below 600 hPa. In other words, the presence of ice microphysics does not qualitatively alter the convective invigoration response. The increased M_c below 600 hPa is achieved by an increase in updraft intensity (Figure 3.2e) as well as changes in updraft area (Figure 3.2f). At 600 hPa, the increases in M_c (Figure 3.2d) at 600 hPa also coincide with the increase of q_c (Figure 3.1).

One might expect the thermodynamic environment to be important for understanding the response on convection. Figure 3.3a shows the relative humidity (RH) in the BASE cases. The profiles exhibit a C-shape, with minima in the mid-troposphere (around 500 hPa). Across the cases, experiments with larger RH have larger M_c (Figure 3.2a). One way of thinking about RH is to examine the changes in temperature (T) and water vapor concentrations (q_v) (Figure 3.3b-c). Near-surface temperatures in the BASE cases do not vary by more than 0.2 K except for RE, which warms by 1.7 K relative to FULL due to the influence of rain re-evaporation on the boundary layer budget discussed in Chapter 2. Above 400 hPa, the FULL case, which has the highest RH among the BASE cases, warms by 3 K more than LIQ. There is also a

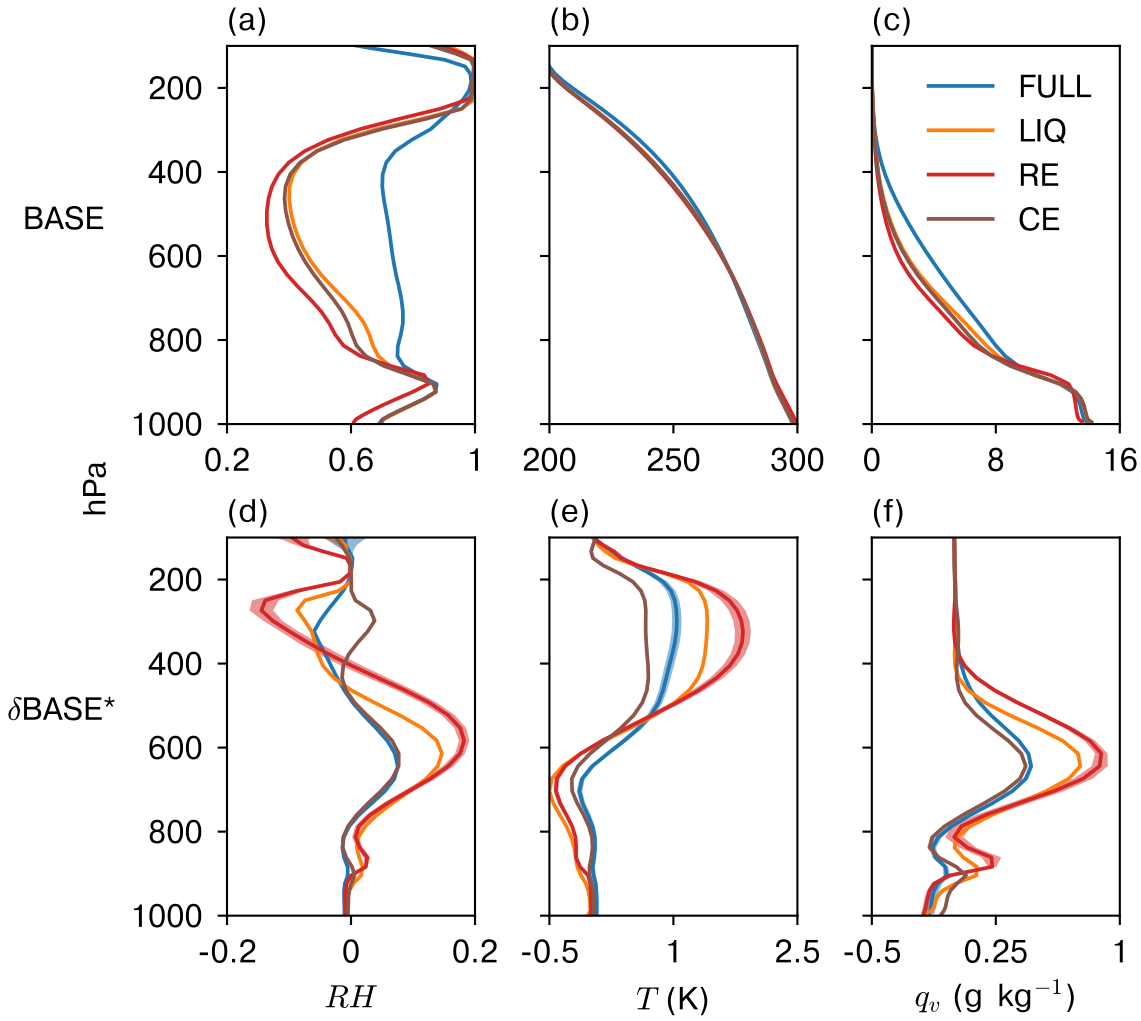


Figure 3.3: Domain-average vertical profiles of (a) relative humidity (RH, unitless), (b) temperature (T, K) and (c) water vapor mixing ratio (q_v, g kg^{-1}) in the BASE experiments. (d-f) Changes in (a-c) due to δBASE*. The shading in (d-f) represents the noise in BASE.

clear contribution of q_v to RH, where cases with larger RH generally coincide with larger q_v (Figure 3.3a and c).

The convective invigoration seen in the δBASE* cases coincide with an increase in mid-tropospheric (e.g. 600 hPa) RH (Figure 3.3d). The decrease in upper-tropospheric RH (e.g. at 300 hPa) also share the same sign as the changes in cloud fraction, and occurs alongside an increase in T (Figure 3.3e). Since temperatures increase slightly (by not more than 0.5 K) at 600 hPa, the increase in RH can be

attributed to an increase in q_v (Figure 3.3f). Having identified that convective invigoration occurs in δBASE* together with increase in mid-tropospheric RH, even in the absence of ice microphysics, we proceed with more quantitative analysis of the connections between the different domain-mean quantities.

3.4 Connections between thermodynamic, dynamic, and microphysical variables

Figure 3.4 summarizes some key relationships discussed in the previous section. Comparing across the BASE (circles) and BASE* (asterisks) cases, there is a general correspondence between column relative humidity (CRH) and vertically-averaged M_c (denoted by square brackets) (Figure 3.4a). The mid-tropospheric (400 to 600 hPa) relative humidity (MRH) is found to have a monotonic relationship with $[M_c]$ across all cases (Figure 3.4b). In this sense, the convective invigoration, as well as changes in M_c across the BASE cases, are linked to a increased RH, especially in the mid-troposphere. One way to connect RH to the microphysical perturbation is by considering the ratio of column-integrated re-evaporation (E) to condensation (C), which we denote by γ [1]. Larger values of γ have been argued to favor larger values of RH in an analytical model of RH which regards re-evaporation as a moistening of the environment (Romps, 2014). In support of this argument, there is a monotonic relationship between γ and CRH across our simulations (Figure 3.4c). Increases in γ can also be associated with increases in MRH (Figure 3.4d).

Table 3.1 presents the decomposition of γ into E and C, together with other relevant quantities in the microphysical budgets. By definition, changes in $C-E$ must equal changes in P, which changes little (less than 10%) across experiments due to the fixed tropospheric radiative cooling. The assumption of fixed P explains why increases

[1] γ is related to the precipitation efficiency ϵ discussed in Chapter 2 by $\gamma = 1 - \epsilon$.

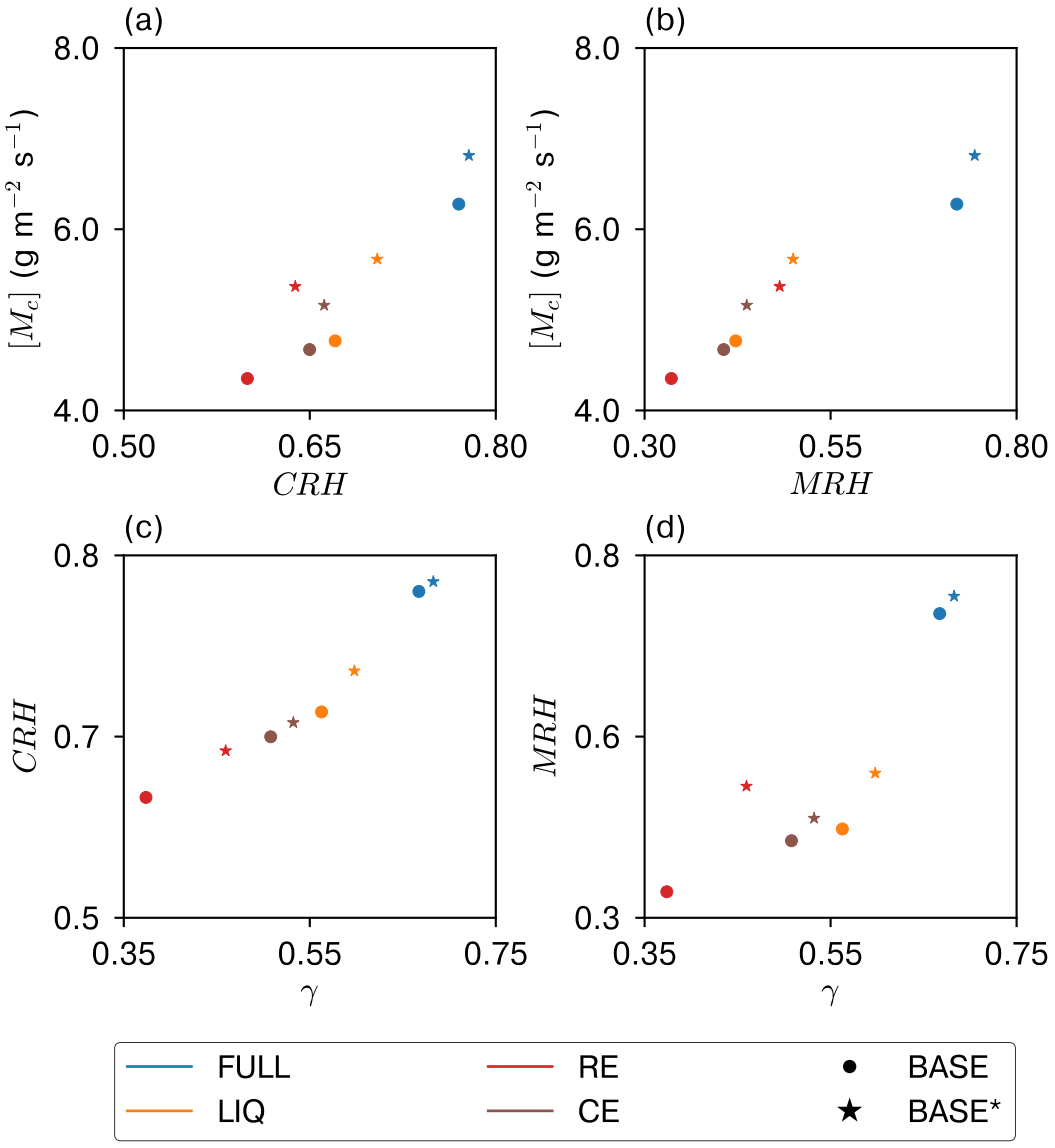


Figure 3.4: Scatter plots of (a) vertically averaged convective mass flux ($[M_c]$, g m^{-2} s^{-1}) against column relative humidity (CRH), (b) $[M_c]$ against mid-tropospheric (600 to 400 hPa) relative humidity (MRH), (c) CRH against the ratio of column-integrated re-evaporation to condensation (γ, unitless), (d) MRH against γ in all experiments.

in E increase both C and γ [2]. Relative to LIQ, E is mainly reduced via the weakening of rain and cloud evaporation in RE and CE, respectively. The weakening of EC in CE (26%) is small compared to the weakening of ER by RE (81%), suggesting that

[2] $\gamma = 1 - \frac{P}{E+P}$, which increases with E for non-negative P (as is the case here).

Table 3.1: The values of γ [the ratio of column-integrated re-evaporation (E) to column-integrated condensation (C)], E and its rain (ER) and cloud (EC) components, C, accretion (AR), precipitation P in the BASE liquid microphysics experiments, and their changes in BASE* (δBASE*). Except for γ, which is unitless, all the quantities are domain-averaged and in mm day^{-1}. The connections between the processes in LIQ are illustrated in Figure 3.5. In FULL, additional ice processes (Table 3.2) are involved in ER, EC, C, and AR.

EXPT	γ	E	ER	EC	C	AR	P
BASE							
FULL	0.67	9.1	3.7	5.4	13.7	8.2	4.5
LIQ	0.56	5.8	2.7	3.1	10.2	7.1	4.5
RE	0.37	2.8	0.5	2.3	7.6	5.2	4.7
CE	0.51	4.6	2.7	2.0	9.1	7.1	4.4
δBASE*							
FULL	0.02	0.8	-0.7	1.5	0.9	-0.6	0.1
LIQ	0.04	1.0	-0.6	1.6	1.1	-0.5	0.1
RE	0.09	1.3	-0.2	1.4	1.3	-0.1	0.1
CE	0.02	0.5	-0.6	1.1	0.5	-0.6	0.0

EC is strongly limited by the availability of condensate. To better understand how the increase in E is achieved under a suppression of autoconversion, we investigate the processes underlying the changes in its precipitation (ER) and cloud (EC) re-evaporation components.

Since ice microphysics do not fundamentally alter convective invigoration, we will focus on LIQ (Figure 3.5a), where the processes are rain (ER) and cloud evaporation (EC), droplet condensation (C), accretion (AR) and autoconversion (CR). In equilibrium, surface evaporation (ES) and precipitation (P) are in balance, as are the sources and sinks of the microphysical terms (i.e. sum of values from arrows directed inward equal the sum of values from arrows directed outward). One observation is that the conversion of q_c to q_p is mostly from accretion, as one might expect from cloud-resolving simulations (e.g. Heikenfeld et al., 2019) and observations (e.g. Gettelman et al., 2013). This does not mean that autoconversion can be disregarded, because in the absence of q_p and ice microphysics, autoconversion is the only way cloud condensates can be converted to precipitation.

Indeed, a reduction in autoconversion acts to reduce the conversion of cloud to precipitating condensates via accretion (Figure 3.5b). The reduction in accretion is balanced by a reduction in rain re-evaporation so as to balance the sources and sinks of q_p. To balance the q_c budget, there is a net increase in $EC - C$, which occurs via increases in both EC and C. In other words, the suppression of accretion leads to opposing responses in EC and ER, which act to moisten and dry the atmosphere, respectively, with the former winning out.

The competing effects of EC and ER shed some light on the response across the δBASE* experiments. As in δLIQ*, the other δBASE* experiments exhibit decreases in AR and ER, and increases in E, EC, and C (Table 3.1). In RE, where the drying response of ER is suppressed, the increase in E is the largest among the δBASE* experiments. In contrast, in CE, the moistening response of EC is suppressed, reducing the increase in E. So far, we have seen that larger values of E increase γ, which is associated with column relative humidity and M_c. In the case of suppressed autoconversion, the increase of cloud re-evaporation exceeds the decrease in rain re-evaporation, leading to a net increase in E. Next, we would like to gain a better understanding of how the changes in microphysical processes influence convective dynamics.

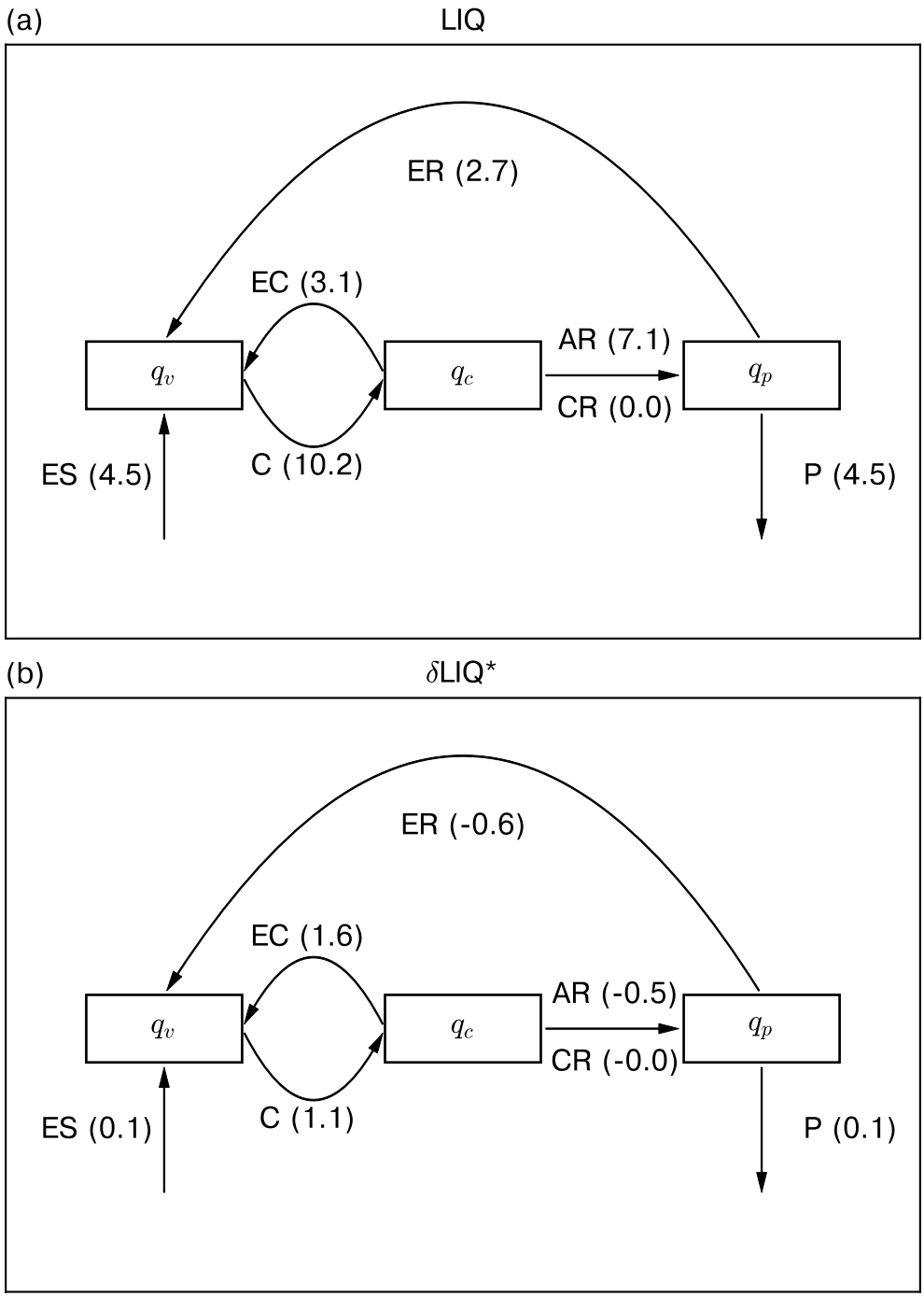


Figure 3.5: Column-integrated and domain-averaged values (mm day^{-1}) of microphysical processes converting between water vapor (q_v), cloud condensates (q_c) and precipitating condensates (q_p) [condensation of cloud condensates (C), evaporation of cloud condensates (EC), conversion of cloud water to rain by autoconversion (CR) and accretion (AR) and evaporation of rain (ER)], as well as surface evaporation (ES) and precipitation (P) for (a) LIQ and (b) δLIQ*. The corresponding values for all configurations are listed in Table 3.1.

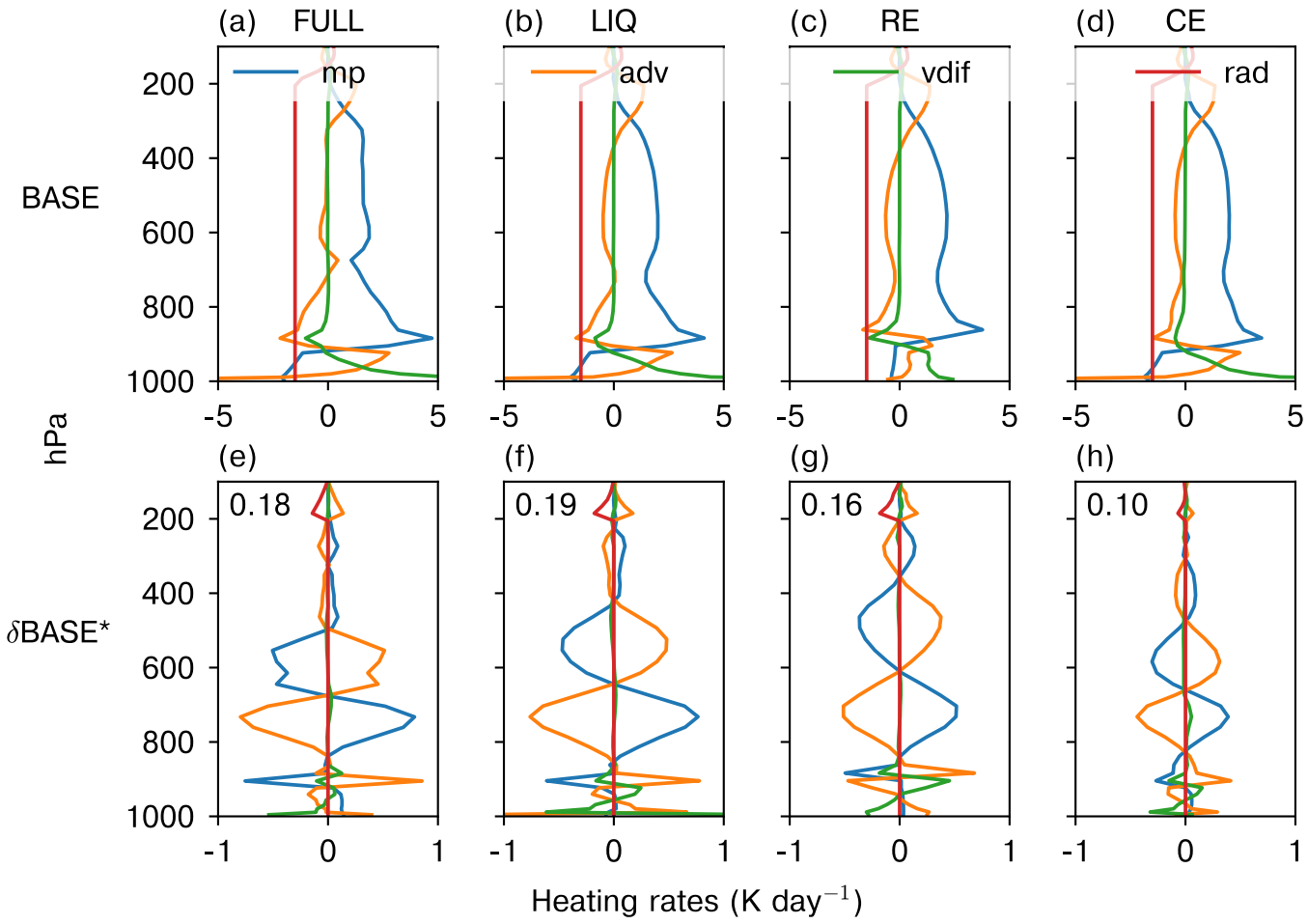


Figure 3.6: Domain-average vertical profiles of the microphysical (mp), advection (adv), vertical diffusion (vdif) and radiative (rad) heating rates in (a) FULL, (b) LIQ, (c) RE and (d) CE. (e-h) Changes in (a-d) due to δBASE*.The vertically-averaged value of the absolute changes in mp is given on the top left hand corner. All values are in K day^{-1}.

We examine the energy budget (Figure 3.6) to identify the leading processes responsible for the altered energy transport due to the increases in convective mass flux. In all the BASE cases (a-d), the prescribed radiative cooling (rad) is balanced by latent heating from the microphysics scheme (mp), vertical diffusion in the boundary layer (vdif), and transport of energy by vertical advection from resolved motions (adv). In δBASE*, the changes are largely a compensation between the mp and adv terms. The column-averaged value of the absolute change in the mp term is each case is given in the top left corner of Figure 3.6e-h. This compensation is similar (within 15%) of the FULL case in LIQ and RE, but is reduced by 44% in CE, consistent with the muting of convective invigoration in CE*. A feature of this compensation is a dipole structure between 800 and 400 hPa, with microphysical heating underneath microphysical cooling that is balanced by advective cooling underneath advective heating. As such, we can think of the convective invigoration as a response to the vertical heating dipole imposed by the microphysical changes.

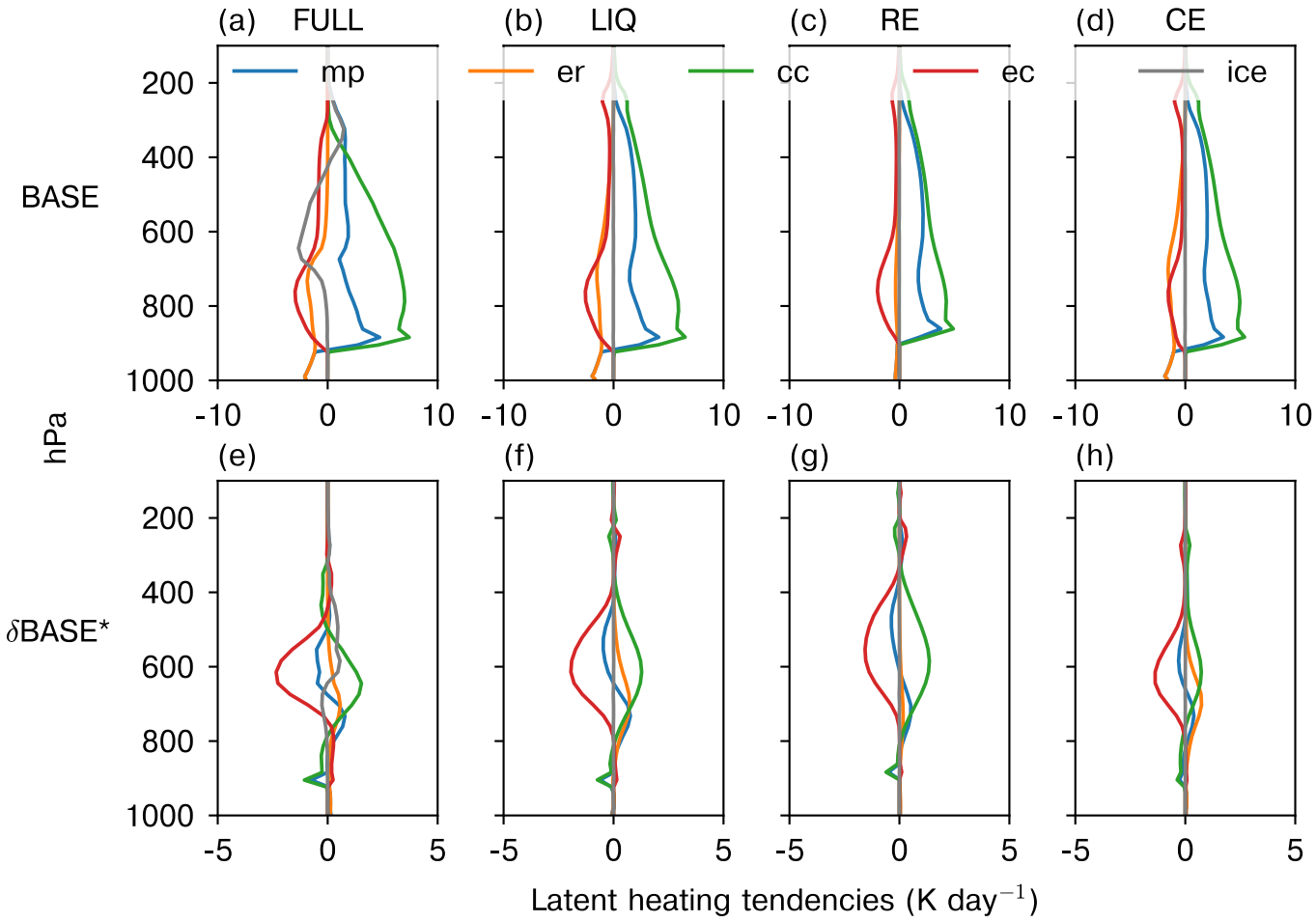


Figure 3.7: The decomposition of the microphysical term in Figure 3.6 (mp) into contributions from rain re-evaporation (er), formation of cloud droplets by condensation (cc), evaporation of cloud droplets (ec), and ice processes (ice) in the BASE configurations (a) FULL, (b) LIQ, (c) RE and (d) CE. (e-h) Changes in (a-d) due to δBASE*. All values are in K day^{-1}.

To understand how the vertical dipole is created in terms of microphysical tendencies, we examine the changes in the latent heat budget (Figure 3.7). In all the BASE cases, condensation of cloud droplets (cc) peaks lower in the atmosphere (around 900 hPa) than the re-evaporation of cloud and rain condensates (ec and er, respectively). Conceptually, the condensation at cloud base generates buoyancy for the air parcel experiencing an updraft. As the parcel rises, it detrains cloud condensates, which evaporate into the surrounding air. Across the BASE cases (Figure 3.7a-d), larger values of γ (e.g. from RE to LIQ) are associated with a larger dipole of condensational heating below re-evaporative cooling. In δBASE* (Figure 3.7e-h), a similar dipole of latent heating beneath cooling is seen. The dipole is mainly a cancellation between condensation (cc) and re-evaporation (ce) of cloud droplets, with ice processes (ice) playing a secondary role. The importance of mid-tropospheric evaporative cooling in creating this latent heating dipole, which we have seen is connected to the changes in convection (Figure 3.6), is consistent with the monotonic relationship between mid-tropospheric relative humidity and M_c (Figure 3.4b).

3.5 Conclusions

3.5.1 Discussion

In interpreting our results, it is useful to return to the microphysical budget constraints (Figure 3.5). Our perturbation experiments suppress the conversion of cloud condensates to precipitating condensates, giving rise to a reduction in precipitation re-evaporation and a decrease in the net production of cloud condensates. The latter can occur in one of three possible pathways: (1) an increase in condensation and a larger increase in cloud re-evaporation; (2) a decrease in condensation and a smaller (less negative) decrease in cloud re-evaporation; (3) changes in condensation and cloud re-evaporation that differ in sign (e.g. an increase in cloud re-evaporation

and a decrease in condensation). Pathway (2) does not occur because the suppressed accretion increases the concentration of cloud condensates, which seems to be the factor limiting cloud re-evaporation. For example, if one contrasts CE with LIQ, despite the prescribed 10-fold decrease in the parameterization, the actual cloud re-evaporation decreases by only 26%. It is reasonable to assume that condensation and cloud re-evaporation tend to change in the same direction. This is borne out in our simulations (Table 3.1), and allows us to rule out (3).

A plausible explanation for convective invigoration in the context of liquid or warm rain microphysics is then as follows. Increased cloud droplet number concentrations reduce accretion via the suppression of autoconversion. In the dry mid-troposphere, cloud re-evaporation is limited by condensate availability. Hence, the increased cloud condensates (due to weaker accretion) act to increase cloud re-evaporation. The additional re-evaporative cooling is balanced by more condensational heating lower in the atmosphere (Figure 3.7), creating a dipole that dynamically further enhances condensation and convective mass flux. Since precipitation is fixed, the increase in condensation must be accompanied by an increase in total re-evaporation (from cloud and precipitating condensates combined), which also favors condensation by moistening the mid-troposphere. Note that this argument is consistent with (i) the increase in cloud re-evaporation outweighing the decrease in precipitation re-evaporation and (ii) the relationship between mid-tropospheric relative humidity and convective mass flux (Figure 3.4b).

Our results support the suggestions of case studies where ice processes (Tao et al., 2007; Morrison, 2012) or upper-level heating (Fan et al., 2018) are not fundamentally important to the changes in convection under an increase in aerosol concentrations, although there are quantitative effects. Figure 3.2 shows that inclusion of ice processes modifies the magnitude of the response. Also, the extent to which the use of saturation adjustment (as in this study) as opposed to resolved supersaturation

affects convective invigoration remains open to debate (Lebo et al., 2012; Heikenfeld et al., 2019). Nevertheless, given that the sign of convective invigoration is robust across various simplified microphysical configurations, we expect that many microphysical schemes should be able to provide some relevant insights into the interactions between microphysics and convection.

3.5.2 Summary

Ice microphysical processes are often thought to play a key role in enhancing convection under polluted conditions (convective invigoration). In the setting of radiative-convective equilibrium with prescribed radiative cooling, we demonstrate that an increase in cloud droplet number concentrations can cause an increase in convective mass flux even in the absence of ice microphysical processes. Subsequent sensitivity tests of liquid microphysical processes indicate that this convective invigoration depends more strongly on cloud re-evaporation as opposed to rain re-evaporation. A microphysical process analysis reveals that the increased cloud droplet number concentrations reduces the rate of conversion of cloud water to rain and leads to an increase in cloud re-evaporation and a decrease in precipitation re-evaporation, with the former outweighing the latter. Suppressing cloud (rain) re-evaporation weakens the responses in cloud (rain) re-evaporation. Besides increasing the relative humidity, the increase in re-evaporation helps create a dipole of condensational heating beneath re-evaporative cooling, with an associated increase in convective mass flux.

3.6 Acknowledgments

We thank Hugh Morrison and Nadir Jeevanjee for helpful conversations.

Table 3.2: Additional ice processes included in the calculation of the terms in Table 3.1 in the FULL cases.

Included in	Process
AR	Cloud droplet accretion by snow
	Cloud droplet collection by graupel
	Cloud droplet collection by snow to graupel
	Accretion of cloud ice by snow
	Autoconversion of cloud ice by snow
	Ice-rain collection
	Ice-rain collision (added to snow)
	Conversion of large ice to snow
	Ice multiplication (rain and snow)
	Ice multiplication (rain and graupel)
EC	Sublimation of cloud ice
C	Deposition of cloud ice
	Primary ice nucleation
ER	Sublimation of graupel
	Sublimation of snow
	Evaporation of graupel
	Evaporation of snow
	Deposition of graupel
	Deposition of snow

Chapter 4

The fast response of tropical cyclones to black carbon

4.1 Introduction

Absorbing aerosols, such as black carbon (BC) and dust, can significantly perturb Earth's radiative balance. Strongly absorbing in the shortwave, BC has an estimated global-mean preindustrial-to-present-day top-of-the-atmosphere (TOA) radiative forcing of 0.3-1.1 W m^{-2} (Myhre et al., 2013), the third largest anthropogenic warming effect on climate after carbon dioxide (CO_2) and methane. In contrast to well-mixed greenhouse gases, the radiative effect of BC varies with its highly uneven horizontal and vertical distributions. The spatial inhomogeneity of BC arises from non-uniform surface emissions and short atmospheric residence time (days) (Bond et al., 2013). In particular, the tropics contribute more than half of the global BC emissions (Bond et al., 2013), and the associated radiative effect is amplified by the strong local insolation (Persad et al., 2012). The spatial distribution of dust is also highly variable, with North Africa as one of the major source regions (Ginoux et al., 2012). Its radiative effect is dependent on complex mineral compositions and optical

properties, which give rise to a wide range of combinations in terms of the relative importance of absorption versus scattering, both in the shortwave and in the longwave. In a global model simulation using the optical characteristics of absorbing dust over the southwestern Sahara, Strong et al. (2015) found that dust enhanced the regional net TOA clear-sky shortwave absorption by up to 30 W m^{-2}, while reducing the surface shortwave fluxes by a similar magnitude. Besides the direct effect, absorbing aerosols are also capable of indirectly modifying the global radiative balance through increasing cloud albedo (Twomey, 1974) and lifetime (Albrecht, 1989) – collectively known as the indirect effects. Since the indirect effects still suffer from large uncertainties (e.g. Carslaw et al., 2013), this study will focus on the climate response to the direct effect in isolation.

Once being subjected to the radiative perturbation of absorbing aerosols, the atmosphere, land and ocean components of the climate system must adjust collectively to re-establish the TOA radiative balance on the planetary scale. As the atmosphere and land respond on much shorter time scales (days to months) than the ocean (years and longer), there is value in establishing a holistic understanding of the climate impacts of absorbing aerosols by separately investigating the fast and slow responses (e.g. Andrews et al., 2010). The focus of this work is on the fast response of the tropical atmosphere-land system from the perspective of tropical cyclones (TCs). Given that extreme weather events such as TCs are under heavy influence of large-scale environment, we begin by reviewing the current literature on the impacts of absorbing aerosols on the tropical general circulation and precipitation.

Absorbing aerosols increase the shortwave radiation retained within the atmosphere. On fast time scales, the atmospheric energy balance dictates that the increased absorption must be balanced, to first order, by a reduction in the tropical-mean latent heat release by precipitation (Andrews et al., 2010; Ming et al., 2010). One can decompose the fractional change in precipitation into those in convective

mass flux and in boundary layer specific humidity (Held and Soden, 2006). Since the latter is small under fixed sea surface temperatures (SST) (as is the case for the fast response), the reduction of tropical-mean precipitation can be linked to a decrease in convective mass flux, which is concurrent with a weakening of the tropical general circulation in climate model simulations (Held and Soden, 2006; Ming and Ramaswamy, 2011).

The radiative heating from absorbing aerosols can influence different monsoonal systems. In the atmosphere-land-only context, Miller and Tegen (1998) discussed an increase in the West African JJA monsoon precipitation in response to the heating, but Mahajan et al. (2012) later found a decrease in precipitation over the same region [see Table 1 of Strong et al. (2015) for a quantitative comparison]. For Asia, where the emissions of BC are concentrated, climate models are in qualitative agreement on the direct effect of absorbing aerosols on fast time scales. Absorbing aerosols are thought to increase pre-monsoonal and decrease monsoonal rainfall over India (Chung et al., 2002; Collier and Zhang, 2009; Mahmood and Li, 2013), while suppressing summer monsoonal rainfall over South China (Persad et al., 2017). To explain features of the induced monsoonal changes over India and China, it was first proposed that absorbing aerosols would generally lead to ascending motion, which tends to enhance precipitation (Menon et al., 2002). To further address the shift of the timing of the Indian monsoon, Lau et al. (2006) suggested that pre-monsoonal aerosol heating strengthened the meridional tropospheric temperature gradient that drives the monsoon. Bollasina et al. (2008) postulated that this enhanced temperature gradient could also be due to the observed reduction in cloud cover in May, possibly due to aerosol heating, which increases the amount of shortwave radiation able to reach and warm the surface. To disentangle the combined effects of atmospheric heating and surface dimming, Persad et al. (2017) systematically considered the impacts of idealized atmospheric heating and surface dimming on moisture convergence and evaporation.

They found that the sign of the aerosol-induced precipitation response over China was the same as that of the response to the imposed surface dimming, as opposed to the atmospheric heating. While atmospheric heating did not determine the sign of precipitation change, it was crucial for differentiating the hydroclimate impacts of absorbing versus scattering aerosols. On the whole, existing works substantiated the potent influence of BC on large-scale circulation and precipitation. One should be cautious in generalizing the findings on mean precipitation to extreme precipitation. The tropical-mean and continental-scale monsoonal precipitation changes caused by absorbing aerosols concern averaging over large domains and long durations. In comparison, extreme precipitation is a subset of the total precipitation corresponding to high percentiles of the intensity distribution, or weather events such as TCs. One cannot rule out a re-distribution of precipitation of different intensities while the average conforms to the large-scale constraints that have been identified. On the other hand, it is well-known that certain large-scale conditions exert strong controls over the development of weather events, a classical example being that low vertical wind shear and high mid-tropospheric humidity have to be satisfied for TCs to occur (e.g. Gray, 1998). In this sense, the past work on aerosol-induced large-scale circulation changes provides a useful starting point for thinking about possible changes in the frequency and intensity of extreme precipitation.

Most of the published literature on the fast TC response to BC focused on environmental factors such as the strength of convection, sources of vorticity disturbances (e.g. African easterly waves) and wind shear. Using satellite observations of the Saharan Air Layer, Dunion and Velden (2004) suggested that dust reinforced a temperature inversion, which might suppress convection, easterly waves, and hence TC activity. Subsequent cloud-resolving model (CRM) case studies of TCs supported the idea that atmospheric heating could reduce TC activity. One such study based on background conditions similar to Hurricane Katrina found lower TC wind speeds

when a partially absorbing aerosol was added, as opposed to a purely scattering aerosol (Wang et al., 2014b). Using CRM simulations of the Atlantic TC development region in June 2006, Chen et al. (2017) found a strengthening of convection by high-altitude dust and a weakening of convection by low-altitude dust. In a TC forecast run, the increased convective inhibition coincided with lower TC wind speeds. The effect of dust on African easterly waves, however, remains elusive. With the help of an analytic expression for the wave response, Grogan et al. (2016) suggested that the different spatial gradients of dust used in previous studies might partially explain the disagreement in the sign of the dust impacts on easterly wave activities. Spatial variations also seem to be crucial for understanding the impacts related to circulation changes, with model results showing shifts (Bretl et al., 2015) or intensification (Evan et al., 2011) of TCs depending on the TC development region considered. As almost all prior studies focused on individual storms, basins or seasons, the question of how absorbing aerosols affect TC frequency and intensity statistics across all basins still remains to be addressed. That the current-generation high-resolution atmospheric general circulation models (AGCMs) are able to resolve global TC climatology (Murakami et al., 2012; Walsh et al., 2015) affords us an opportunity to shed some light on the question.

Such AGCMs have already been utilized to study TC changes under global warming. A prominent example is the Geophysical Fluid Dynamics Laboratory (GFDL) High-Resolution Atmospheric Model (HiRAM), which was employed to simulate the fast response in TC frequency (number count) and intensity (maximum wind speed) to a doubling of CO_2 (Held and Zhao, 2011, henceforth HZ11). HZ11 found that TC frequency decreased significantly, confirming the earlier results of Yoshimura and Sugi (2005), while TC intensity decreased only slightly. Both HZ11 and Sugi et al. (2012) made scaling arguments connecting changes in TC frequency to large-scale vertical velocity, suggesting that the latter is a better predictor of TC frequency changes than

wind shear or potential intensity (PI) (Emanuel, 1986). Following the experimental design of HZ11, Walsh et al. (2015) reproduced the decreases in TC frequency and genesis-weighted vertical velocity in response to CO_2 with a suite of global models. While these global model simulations have advanced our understanding of the fast response to well-mixed greenhouse gases, they do not address, at least directly, the impacts arising from the horizontal and vertical inhomogeneity of aerosol forcings.

This work uses HiRAM to investigate the fast response of simulated TCs to changes in BC loadings as well as horizontal and vertical distributions. Section 4.2 covers some key features of HiRAM and the experimental design. In Section 4.3, we describe the direct radiative heating of BC in different cases, the resulting changes in TC frequency (in relation to mid-tropospheric vertical velocity) and in TC intensity (as viewed from the perspective of PI). A discussion of the implications and limitations is given in Section 4.4, and a summary of the key findings in Section 4.5.

4.2 Methods

4.2.1 Model description

The GFDL HiRAM (Zhao et al., 2009, 2012) uses a finite-volume cubed-sphere dynamical core (Putman and Lin, 2007) with 180 grid points on each side, yielding a horizontal resolution of approximately 50 km, and 32 vertical levels. Most of the physics parameterizations in HiRAM follow those of the GFDL AM2.1 (GFDL Atmospheric Model Development Team, 2004). The exceptions are the shallow convection scheme (Bretherton et al., 2004), the diagnostic cloud fraction scheme (Zhao et al., 2009), and the land model (Dunne et al., 2012). The choice of convection scheme results in a significant portion of convection in HiRAM being resolved at the grid scale, as opposed to being parameterized. The large-scale fraction of the tropical precipitation is 39% for HiRAM, as compared to 7.5% for AM2.1 (with a horizontal resolution

of ∼200 km). The simulated TC genesis climatology, including spatial distribution and seasonal cycles, agrees well with observations (Zhao et al., 2009). Similar to other global models, HiRAM underestimates TC intensity. The detection algorithm used in this study defines TC as a sustained warm-core vortex with 10-meter winds exceeding 15.3 m s^{-1} (Zhao et al., 2009, 2012). The algorithm occasionally identifies storms more than 30° from the equator as TCs, which are excluded from this analysis.

The offline present-day (1980-1999) aerosol climatology used in HiRAM is generated with a chemical transport model (Model for Ozone and Related Chemical Tracers, MOZART) (Horowitz et al., 2003; Horowitz, 2006), and does not interact with HiRAM's meteorology. The optical properties of aerosols are calculated with the Mie theory. In particular, BC is assumed to follow a log-normal distribution (with a geometric mean radius of 0.0118 μm and a geometric standard deviation of 2.0) and have a single-scatter albedo of ∼0.35 in the visible spectrum (Haywood and Ramaswamy, 1998). Aerosol indirect effects are not included, as cloud droplet number concentrations are fixed at 150 cm^{-3} over the land and 50 cm^{-3} over the ocean.

4.2.2 Experimental design

We explore the fast TC response to BC across a wide range of spatial distributions in a series of model simulations. The control experiment (CNTL) uses the present-day aerosol climatology as described above. The BC loadings are increased uniformly by ten times in the 10X experiment. The magnitude of the perturbation is motivated partly by the well-documented underestimation of BC concentrations in global models (Bond et al., 2013; Cohen and Wang, 2014), and the desire to achieve a favorable signal-to-noise ratio. Due to similar considerations, recent studies of BC impacts on hydroclimate chose comparable, or even larger increases (Sand et al., 2015; Guo et al., 2016; Kovilakam and Mahajan, 2016). We consider BC increases isolated over the land (LAND) and over the ocean (OCEAN) separately. To investigate the

sensitivity of TCs to the vertical distribution of BC, we confine BC increases to the free troposphere ($\sigma < 0.78$, roughly above 780 hPa) and to the boundary layer ($\sigma \geq 0.78$, roughly below 780 hPa) in the FT and BL experiments, respectively. Similar to HZ11, we double CO_2 from its present-day value in the CO2 experiment. All experiments are run from 1980 to 1999 using SSTs and sea ice prescribed from the Hadley Centre Sea Ice and Sea Surface Temperature (HADISST) observational data set (Rayner et al., 2003). The first year is discarded as spinup, and the remaining 19 years are analyzed.

4.3 Results

4.3.1 Magnitudes and spatial distributions of atmospheric absorption

We use the tropical-mean changes in atmospheric absorption as a starting point for understanding the basic characteristics of the fast response to increased BC and CO_2 (Table 4.1). The shortwave absorption (AS) is computed as the net shortwave (SW) radiative fluxes entering the atmospheric column from the TOA and surface (SFC), i.e. $AS = SW_{\downarrow}^{TOA} - SW_{\uparrow}^{TOA} + SW_{\uparrow}^{SFC} - SW_{\downarrow}^{SFC}$, where the subscripts $\uparrow$ and $\downarrow$ denote upward and downward fluxes, respectively, and positive values of AS represent net atmospheric heating. Similarly, the longwave absorption (AL) can be calculated as $LW_{\uparrow}^{SFC} - LW_{\downarrow}^{SFC} - OLR$, where OLR is the TOA outgoing longwave radiation. The increase in shortwave absorption (δAS) amounts to 9.9 W m^{-2} in the 10X case. Fortuitously, the LAND (4.6 W m^{-2}) and OCEAN (5.2 W m^{-2}) cases each account for about half of the increase in 10X. The FT (5.2 W m^{-2}) and BL (5.0 W m^{-2}) cases also contribute roughly equally. Hence there is no need for normalization when comparing the two pairs of experiments. In comparison, the CO_2 forcing manifests as an increase of longwave absorption (2.3 W m^{-2}).

Table 4.1: Tropical-mean changes in the various components of the atmospheric energy balance (W m^{-2}). The fractional changes (percentage) are in parentheses.

	δAS	δAL	δSH	δLH	$\delta(SH+LH)$
10X	9.9	-3.0	-2.5 (-11.9)	-4.2 (-4.5)	-6.7 (-5.9)
LAND	4.6	-1.6	-1.8 (-8.7)	-1.3 (-1.4)	-3.2 (-2.8)
OCEAN	5.2	-1.4	-0.76 (-3.6)	-2.9 (-3.2)	-3.7 (-3.2)
FT	5.2	-2.1	-0.77 (-3.6)	-2.2 (-2.4)	-3.0 (-2.6)
BL	5.0	-0.96	-1.9 (-8.9)	-2.1 (-2.2)	-4.0 (-3.5)
CO2	0.74	2.30	-0.59 (-2.8)	-2.4 (-2.6)	-3.0 (-2.6)

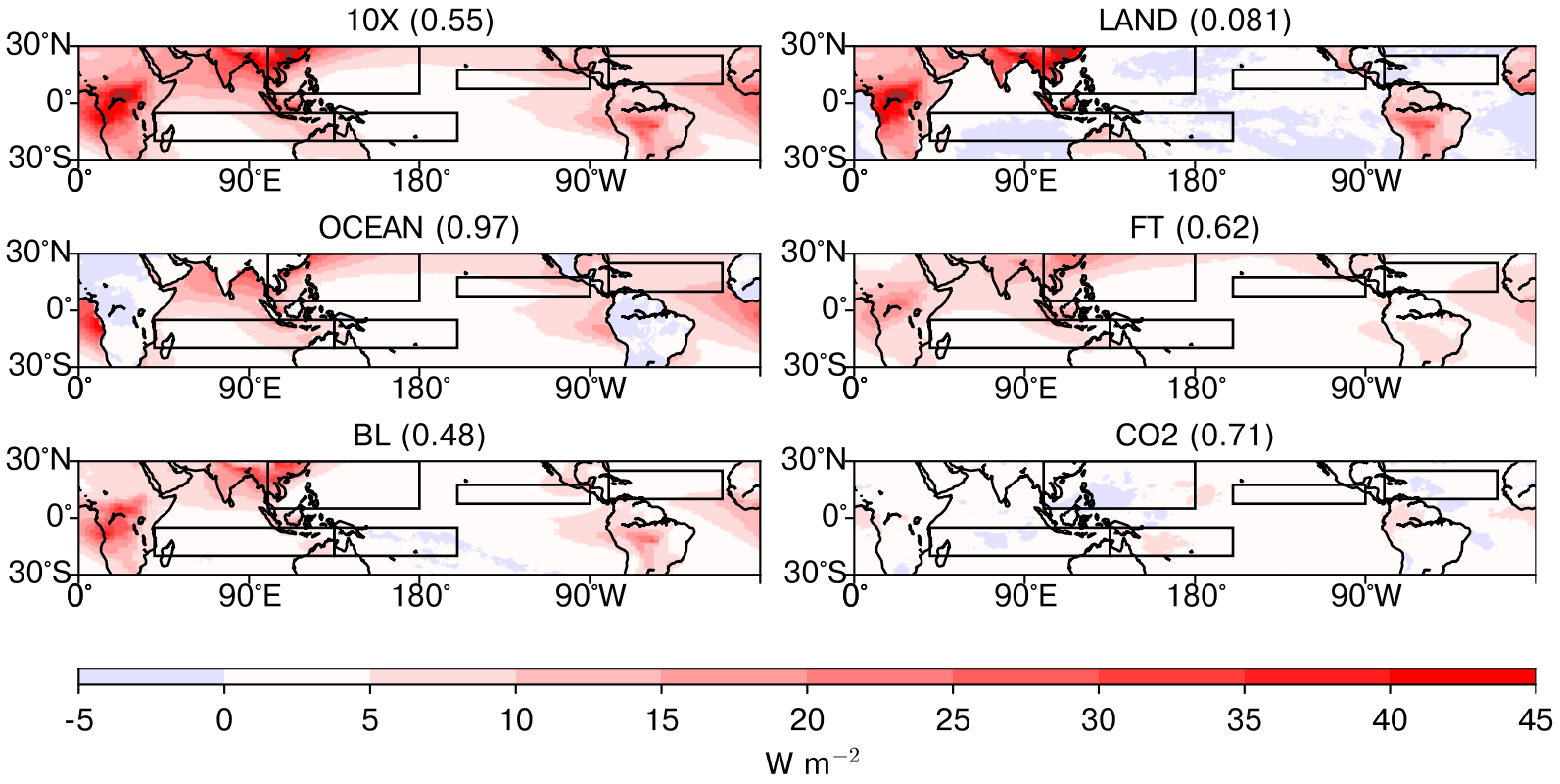


Figure 4.1: Geographical distributions of the changes in atmospheric absorption (W m^{-2}, δAS for BC cases and δAL for CO2). The numbers in parentheses indicate the fraction over the ocean (f_o). The rectangle boxes denotes the main development regions, as is the case for the other maps in this chapter.

The geographical distributions of δAS due to the BC perturbations are given in Figure 4.1. The pattern in the 10X case reflects the present-day BC climatology. The largest increases are found over the main source regions, namely South and East Asia, Central Africa and the Amazon, where the local values can exceed the tropical-mean by a factor of more than three. Since TC genesis takes place exclusively over the ocean, one may speculate that the efficacy of BC-induced absorption in altering TC would depend on whether it is over the land or over the ocean. To facilitate this discussion, we calculate the fraction of the increased absorption over the ocean (f_o) as $a_o \delta AS_o / \delta AS$, where a_o is the fraction of the tropics covered by the ocean (0.75), and AS_o is the increase in shortwave absorption averaged over the ocean. As a limiting case, a f_o of one means that all the increased absorption occurs over the ocean. Despite stronger absorption over the land than over the ocean, f_o is 0.55 in 10X due to much larger oceanic coverage. As expected, f_o is effectively zero in LAND and one in OCEAN. That f_o is larger in the FT case (0.62) than in the BL case (0.48) indicates that BC is more elevated over the ocean, consistent with free-tropospheric transport from land source regions to adjacent oceans.

The vertical distributions of the tropical-mean shortwave heating rate changes are shown in Figure 4.2. The profile of the 10X case is bottom-heavy, with a maximum of 0.17 K day^{-1} at ∼850 hPa, representing a 17% increase over the control value. The heating decreases gradually above 850 hPa: the heating rate increase at 500 hPa is about 45% of that at 850 hPa. As explained above, the heating profile is indeed more bottom-heavy in LAND than in OCEAN. This is particularly true above ∼150 hPa, where the heating rate in OCEAN more than doubles that in LAND. This has important implications for TC responses, a point to which we will return later. Only the free-tropospheric and (boundary layer) heating is present in the FT (BL) case. The longwave heating in the CO2 case is mostly confined between 600 and 850 hPa.

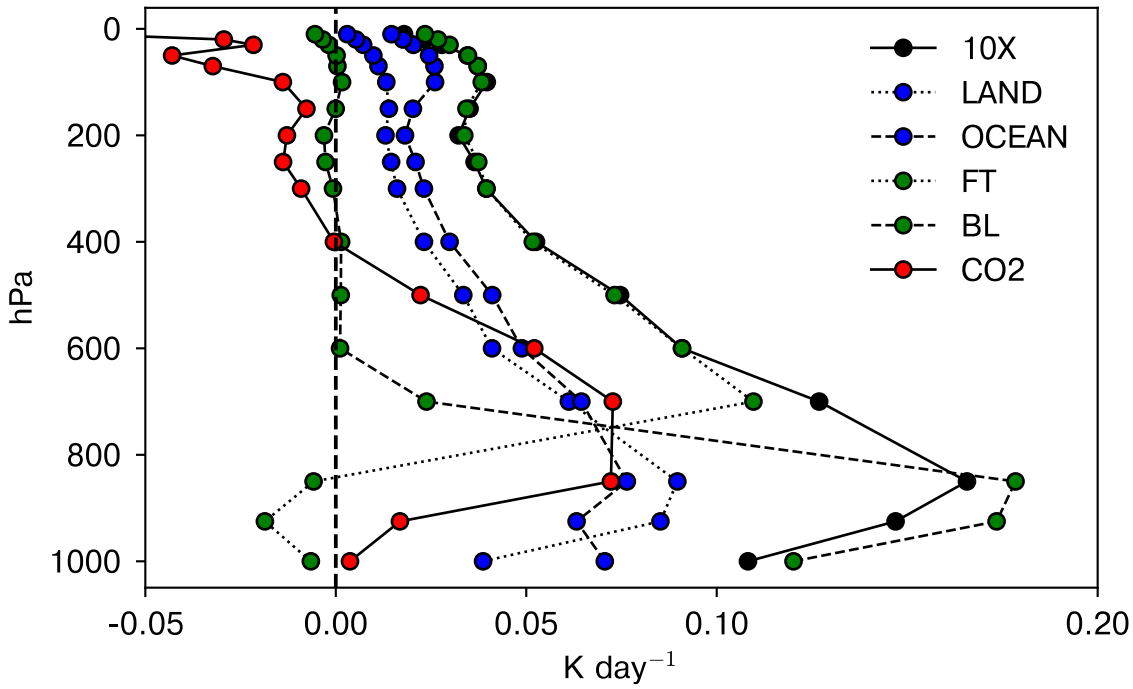


Figure 4.2: Vertical distributions of the tropical-mean changes in radiative heating rate (K day^{-1}, shortwave for the BC cases and longwave for CO2).

4.3.2 Changes in TC frequency and intensity

Table 4.2: Fractional changes (percentage) in TC and hurricane counts in the entire, Northern Hemisphere (NH) and Southern Hemisphere (SH) tropics. Statistically significant values are in bold.

	TC (Tropics)	TC (NH)	TC (SH)	Hurricane (Tropics)	Hurricane (NH)	Hurricane (SH)
10X	**-21**	**-17**	**-28**	**-26**	**-23**	**-34**
LAND	**-8.4**	**-7.2**	**-11**	**-15**	**-15**	**-13**
OCEAN	**-13**	-3.6	**-32**	**-14**	-5.1	**-39**
FT	**-14**	**-10**	**-23**	**-18**	**-15**	**-25**
BL	-1.6	1.7	**-8.7**	-3.8	-1.8	-9.1
CO2	**-9.4**	**-5.5**	**-18**	**-9.2**	**-8**	**-13**

Except for BL, all perturbation cases show statistically significant decreases in TC frequency (Table 4.2). The tropical-mean reduction is 21% in the 10X case. Despite similar increases in shortwave absorption, the reduction in LAND (8.4%) is considerably less than in OCEAN (13%), meaning that BC over the land is not as

effective at changing TCs as that over the ocean. Although this is hardly surprising given that TC genesis occurs exclusively over the ocean, the extent to which land-based atmospheric absorption can affect TC speaks to the tightly coupled nature of the tropical circulation due to the lack of scale separation. It is also interesting to note that the combined effects, if assumed to be linear, are virtually the same as the 10X case. TC formation is very sensitive to the vertical structure of atmospheric absorption. The reduction amounts to 14% in the FT case, while BL yields no significant change. They do not add up linearly to the 10X case. This suggests that free-tropospheric absorption is substantially more effective at suppressing TCs than the same magnitude of absorption placed within the boundary layer. Hurricanes (with maximum wind speeds greater than 29.5 m s^{-1}) decrease at rates even higher than TC for all BC cases, hinting at possible influence on intensity. This, however, does not hold for CO2. In terms of hemispheric responses, the fractional changes in the Northern Hemisphere are usually greater (less negative) than in the Southern Hemisphere, which is even the case for CO2. This is contrary to the doubling CO_2 simulation in HZ11, and suggests that longer integrations are needed for assessing the robustness of any disparity between the hemispheres.

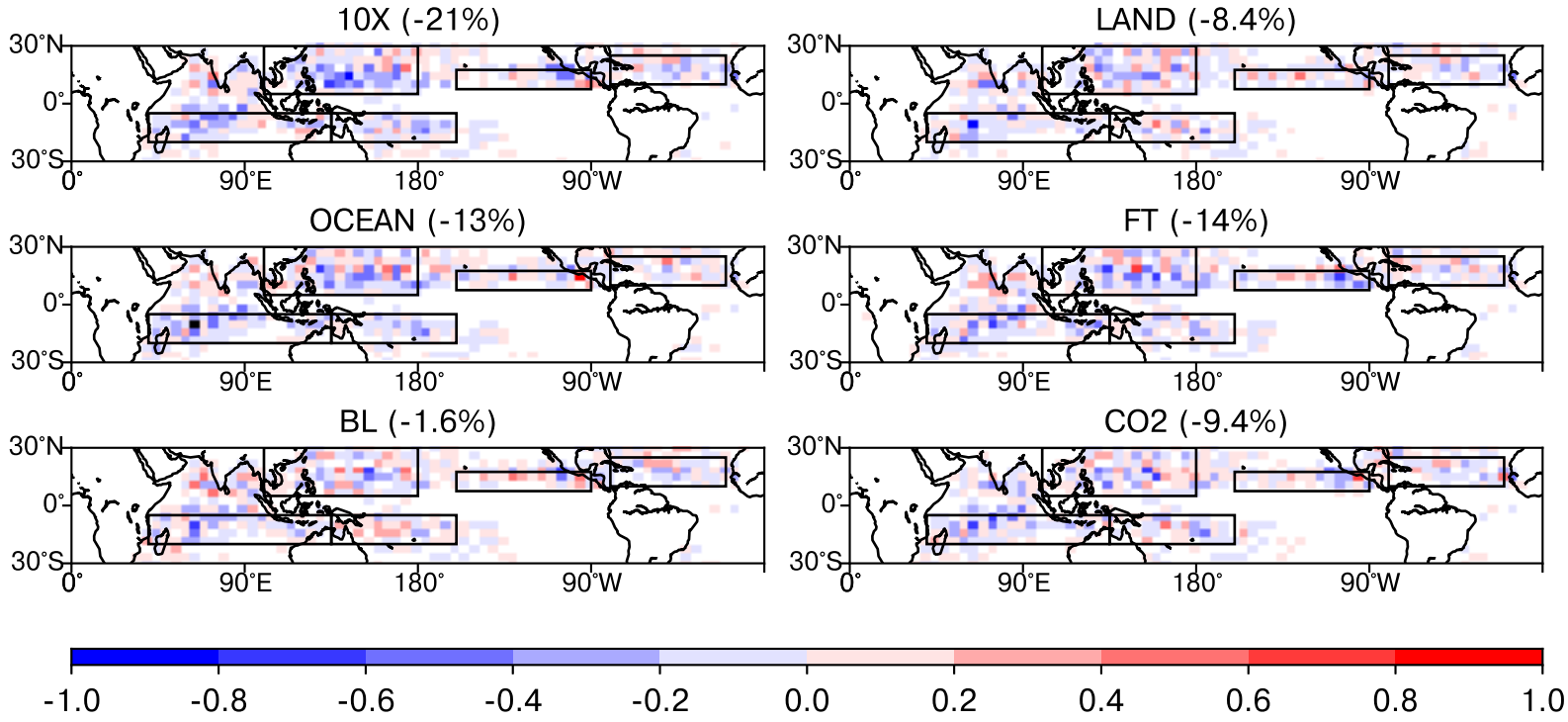


Figure 4.3: Geographical distributions of the changes in annual-mean TC genesis counts averaged over 4° × 5° grids.

The geographical distributions of the changes in annual-mean TC genesis counts are shown in Figure 4.3. The decreases in 10X are distributed unevenly among the oceanic basins, concentrated over the main development regions with West Pacific being the most prominent one, while no robust signal emerges on their poleward flanks. The same is true to the other cases, with BL as a notable exception.

Following HZ11, one can write the number of TCs with the maximum lifetime wind speed exceeding a given value I ($F(I)$) as $NP(I)$, where N is the total number of TCs, and $P(I)$ is the normalized cumulative probability distribution of TC intensity. Then the change $\delta F(I)$ can be decomposed into two parts: $\delta NP(I)$ and $N\delta P(I)$. The $\delta NP(I)$ term represents the change in TC intensity distribution solely due to the change in the overall TC frequency discussed above. The $N\delta P$ term arises from a change in the normalized intensity distribution. δF and $N\delta P$ are plotted in the upper and middle panels of Figure 4.4, respectively. For 10X, F decreases at all intensity levels. The same is apparently true for CO2. The major difference is that increased BC causes a weakening of TC intensity (as measured by I), as one can gather from the substantial reductions from $N\delta P$, while CO_2 does not alter TC intensity appreciably. The weakening is present in other BC cases, albeit to a lesser extent than 10X.

It is more natural to quantify changes in TC intensity in terms of maximum wind speed. To that end, one can plot the change in wind speed (δI) for each percentile bin, which is labeled with the corresponding wind speed in CNTL (the lower panel of Figure 4.4). The δI result confirms the widespread weakening of intensity inferred from $N\delta P$ for BC cases.

4.3.3 Connections with large-scale environment

It is well known that increased atmospheric absorption, whether it is due to absorbing aerosols or CO_2, would lower latent heating or precipitation as part of the fast response (Andrews et al., 2010; Ming et al., 2010). This is borne out in Table 4.1. For

10X, the tropical-mean latent heating (δLH) decreases by 4.2 W m^{-2}, less than half of the imposed BC heating (9.9 W m^{-2}). A reduction in sensible heating (δSH, 2.5 W m^{-2}) accounts for part of the difference. The ratio of δSH to δLH (analogous to the canonical Bowen's ratio) is 0.6. The precipitation reduces by 4.5%. Although SH and LH decrease for all other BC cases, their relative magnitude varies with spatial distribution. The ratio is substantially larger for LAND (1.4) than for OCEAN (0.26). This is because moisture is of limited supply over the land, making it possible for sensible heating to dominate latent heating. A different mechanism is behind the divergence between FT (0.35) and BL (0.90) in this regard. Originating at the surface and permeating the boundary layer by small-scale eddies, sensible heating is more effective at balancing out BC heating placed in the boundary layer. Adjusting moist convection and associated latent heating, on the other hand, is the main means to counteract free-tropospheric heating. CO_2 is more potent than BC in altering latent heating to the extent that the decrease in latent heating (2.4 W m^{-2}) is even slightly more than the longwave heating (2.3 W m^{-2}).

Although the fractional reductions in latent heating (precipitation) are much smaller than those in TC count, they are positively correlated. A linear regression through the origin (used throughout the chapter) yields a correlation coefficient (R) of 0.75, with BL as an outlier. This hints at a possible connection between TC frequency and tropical-mean precipitation, a quantity under strong energetic constraints.

To move beyond tropical means and focus on TC genesis seasons and regions, the monthly-mean spatial pattern of genesis [$G(x,y,t)$,t=1,...,12] can be used for computing the weighted mean of a variable $A(x,y,t)$ ($[A]_G$) as $\overline{G(x,y,t)A(x,y,t)}/\overline{G(x,y,t)}$, and the weighted spatial pattern ($[A(x,y)]_G$) as $\widetilde{G(x,y,t)A}(x,y,t)/\widetilde{G(x,y,t)}$, where the overline denotes time and spatial averaging and the tilde time averaging. The fractional changes in genesis-weighted precipitation ($\delta[P]_G$), along with a few other important variables, are listed in Table 4.3. $\delta[P]_G$ are highly correlated ($R = 0.81$)

with those of the un-weighted tropical-mean δP across all cases, but are three times as large. As such, $\delta[P]_G$ is much closer to, albeit consistently smaller than, the variations in TC frequency than δP in terms of fractional changes.

Table 4.3: Fractional changes (percentage) of genesis-weighted precipitation (P), 500-hPa vertical velocity ($-\omega_{500}$), wind shear (S), potential intensity ($\mathcal{I}$), thermodynamic efficiency ($\mathcal{T}$) and enthalpy difference ($\mathcal{E}$).

	$\delta[P]_G$	$\delta[-\omega_{500}]_G$	$\delta[S]_G$	$\delta[\mathcal{I}]_G$	$\delta[\mathcal{T}]_G$	$\delta[\mathcal{E}]_G$
10X	-12	-19	4.6	-3.4	-2.4	-4.1
LAND	-5.6	-11	2.2	-1.1	-0.93	-0.93
OCEAN	-8.2	-11	2.7	-2.1	-1.5	-2.9
FT	-7.4	-13	2.9	-2.5	-2.1	-2.4
BL	-6.1	-8.0	2.3	-0.87	-0.38	-1.6
CO2	-5.5	-7.6	2.1	-1.5	-0.68	-2.5

The genesis-weighted 500-hPa vertical velocity ($[-\omega_{500}]_G$) filters out subsidence regions, and decreases in all cases (Table 4.3). The magnitudes are consistently larger than $\delta[P]_G$. A linear regression against the variations in total TC count yields a slope of 1.0 and a R of 0.85, making $\delta[-\omega_{500}]_G$ a better predictor of TC frequency changes than $\delta[P]_G$. This suggests that TC frequency is proportional to the total amount of deep convection over the genesis regions as the latter plays an important role in moistening the mid-troposphere, a condition essential for genesis (HZ11). The spatial patterns of $[-\omega_{500}]_G$ is shown in Figure 4.5. The reduction is robust over the main development regions, and is not as noisy as TC counts (Figure 4.3). There is no apparent difference among the experiments including CO2.

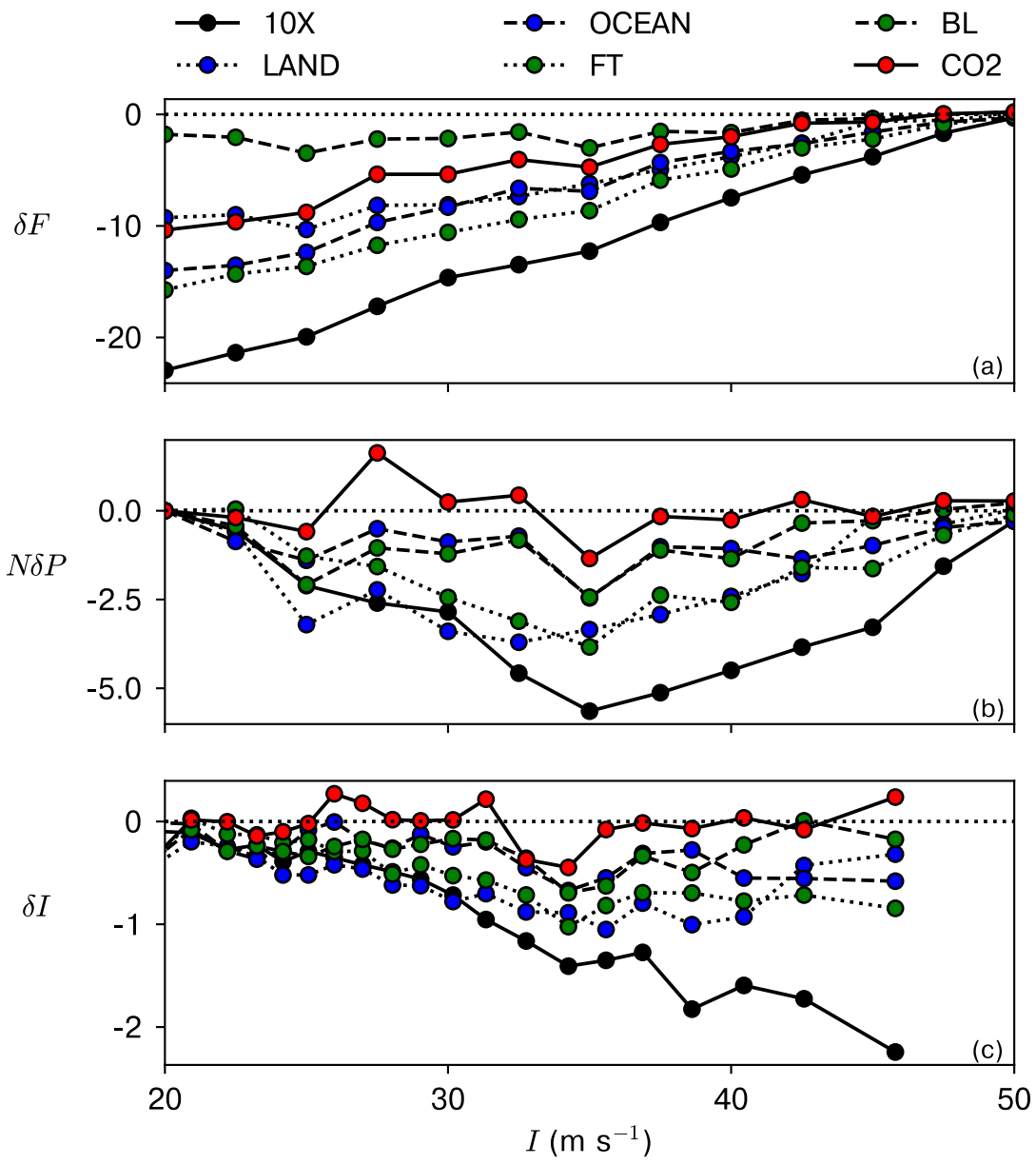


Figure 4.4: Changes in TC intensity as measured by δF (upper), $N\delta P$ (middle) and δI (lower). See text for explanation.

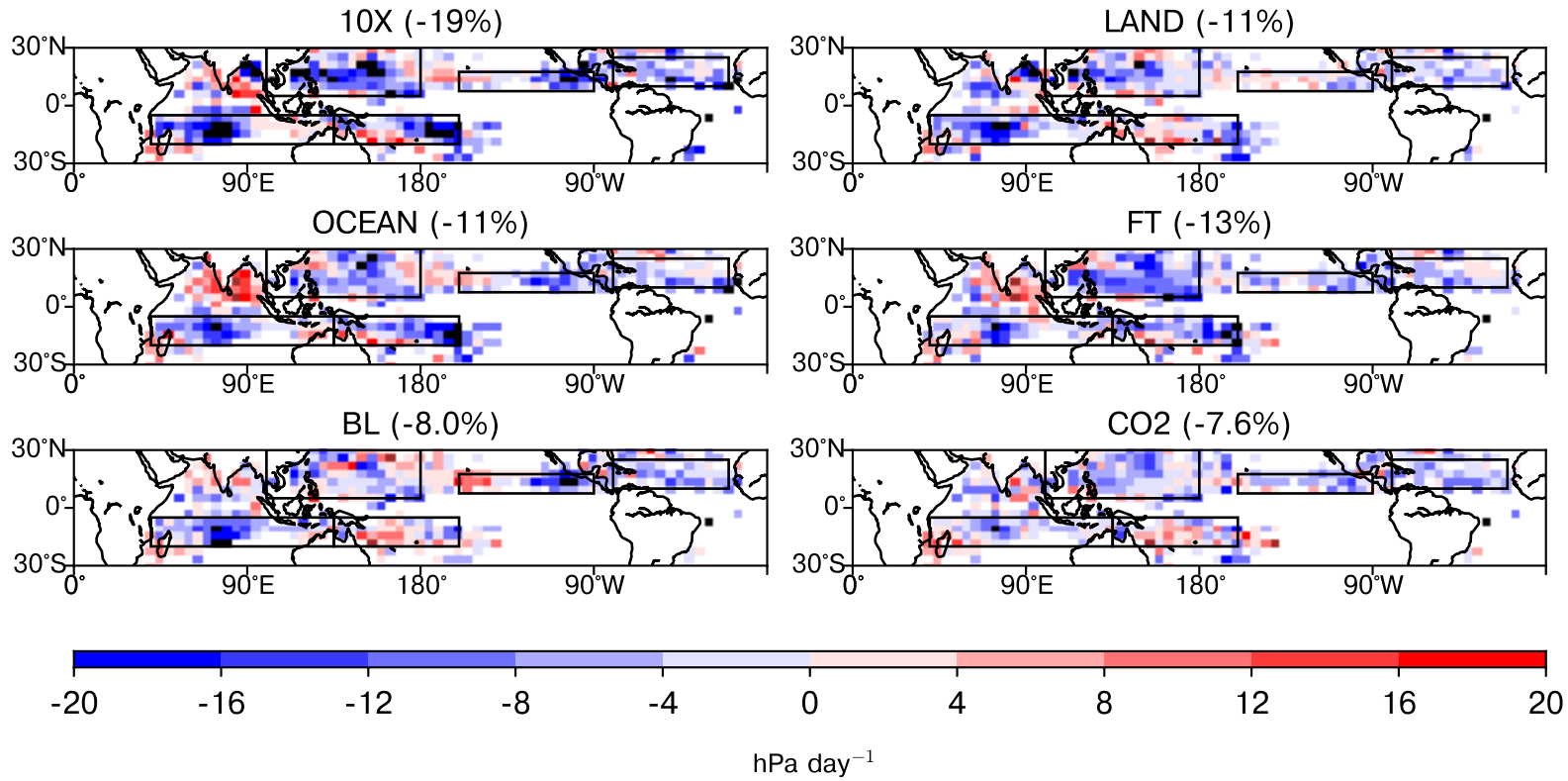


Figure 4.5: Geographical distributions of the changes in genesis-weighted 500-hPa vertical velocity ($\delta[-\omega_{500}]_G$, hPa day^{-1}). Tropical-mean values are in parentheses.

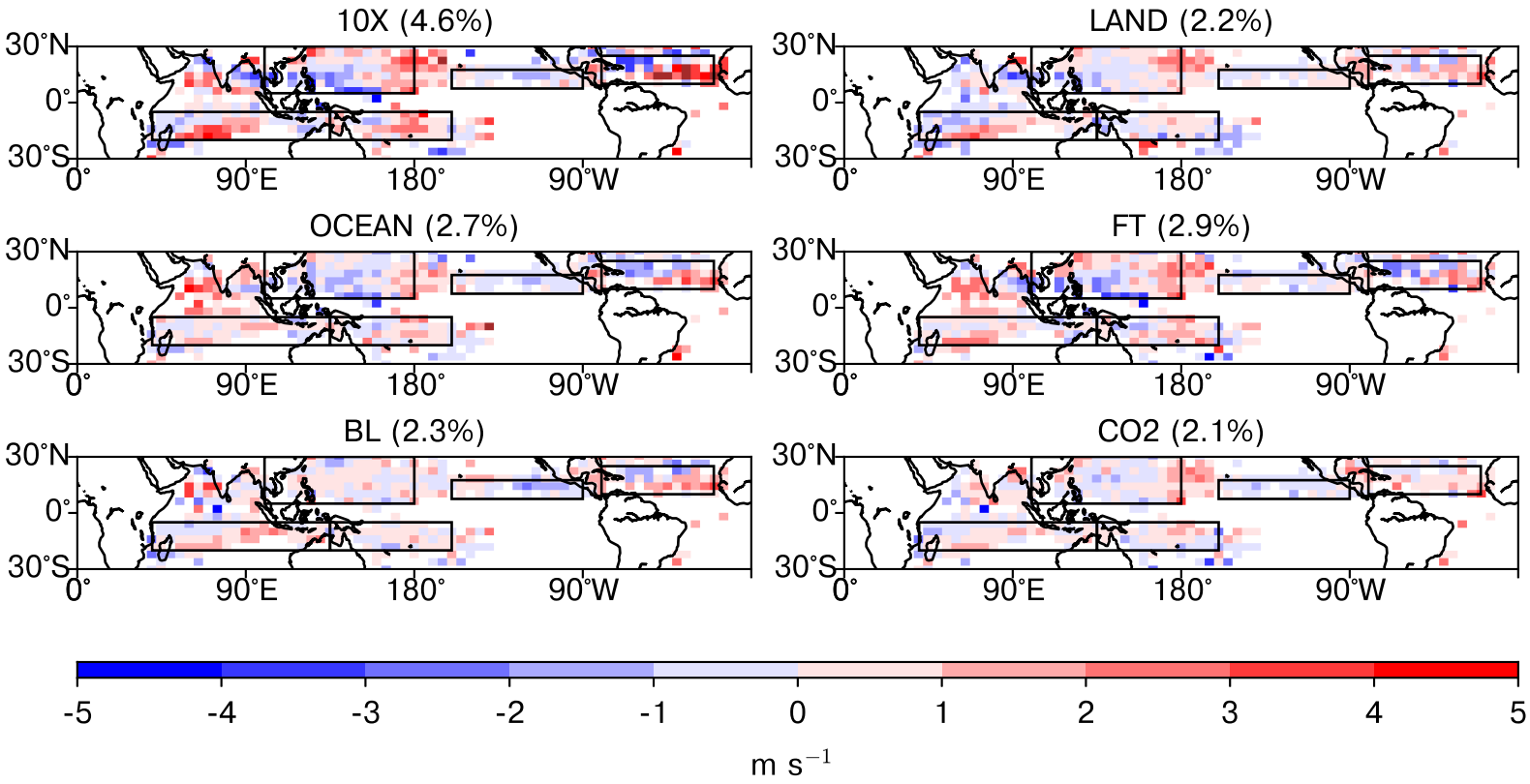


Figure 4.6: Same as Figure 4.5, but for wind shear (S, m s^{-1}).

The vertical shear index (S) is computed as the absolute value of the difference between monthly-mean 850 and 200-hPa vector winds. The genesis-weighted value increases in all cases (Table 4.3), which is consistent with lower TC number as it is well known that strong wind shear disfavors genesis. BL is still a notable exception. The correlation coefficient (R) is 0.80. The geographical distributions (Figure 4.6) appear to be more variable than $[-\omega_{500}]_G$, but rather similar among all the cases.

The potential intensity (PI) theory posits that the maximum wind speed achieved by a TC is constrained by thermodynamic considerations (e.g. Emanuel, 1988; Bister and Emanuel, 1998). Furthermore, PI is also thought to be relevant for genesis (Camargo et al., 2007b). One can write PI ($\mathcal{I}$) as:

$$\mathcal{I}^2 = \frac{C_k}{C_d}\mathcal{T}\mathcal{E}, \tag{4.1}$$

where C_k and C_d are the exchange coefficients for enthalpy and momentum, respectively. The term $\mathcal{T}$ is defined as $(T_s - T_o)/T_o$, where T_s and T_o are the surface and outflow temperatures, respectively, and can be perceived as the thermodynamic efficiency of TC. The term $\mathcal{E}$ is the enthalpy difference between the surface and boundary layer, i.e. $c_p(T_s - T_b) + L(q_s^* - q_b)$, where c_p is the specific heat of dry air at constant pressure, L the latent heat of vaporization, q specific humidity and q^* saturation specific humidity. The subscripts s and b denote the surface and boundary layer, respectively. We use a parcel lifting algorithm (Bister and Emanuel, 2002) (available at `ftp://texmex.mit.edu/pub/emanuel/TCMAX/`) to estimate the changes in the outflow temperature and enthalpy. The resulting changes in genesis-weighted PI are given in Table 4.3. The variable decreases in all BC cases as well as CO2, in qualitative agreement with lower TC counts. More quantitatively, Camargo et al. (2007a) assumed that genesis frequency is proportional to PI raised to the third power, which implies that the fractional change in TC frequency would be three times of that in PI.

In this set of simulations, the correlation between the two quantities is exceptionally high ($R = 0.96$). This is mainly because $\delta[\mathcal{I}]_G$ captures the lack of frequency change in the BL case much better than the other three metrics discussed above. Yet, their ratio is about six, suggesting that PI has an even stronger bearing on TC number than suggested by Camargo et al. (2007a). Although lower PI is generally consistent with the weakening of TC intensity in BC cases, the reduced PI in CO2 appears to be at odds with unchanged intensity. This issue can be illustrated by contrasting CO2 with LAND. Despite similar $\delta[\mathcal{I}]_G$ in the two cases, LAND shows a distinct decrease in intensity (Figure 4.4). Figure 4.7 shows the spatial structures of $\delta[\mathcal{I}]_G$. The decrease is widespread, and relatively uniform over the main development regions. There is no obvious dependence on the spatial distributions of BC or CO_2 forcings.

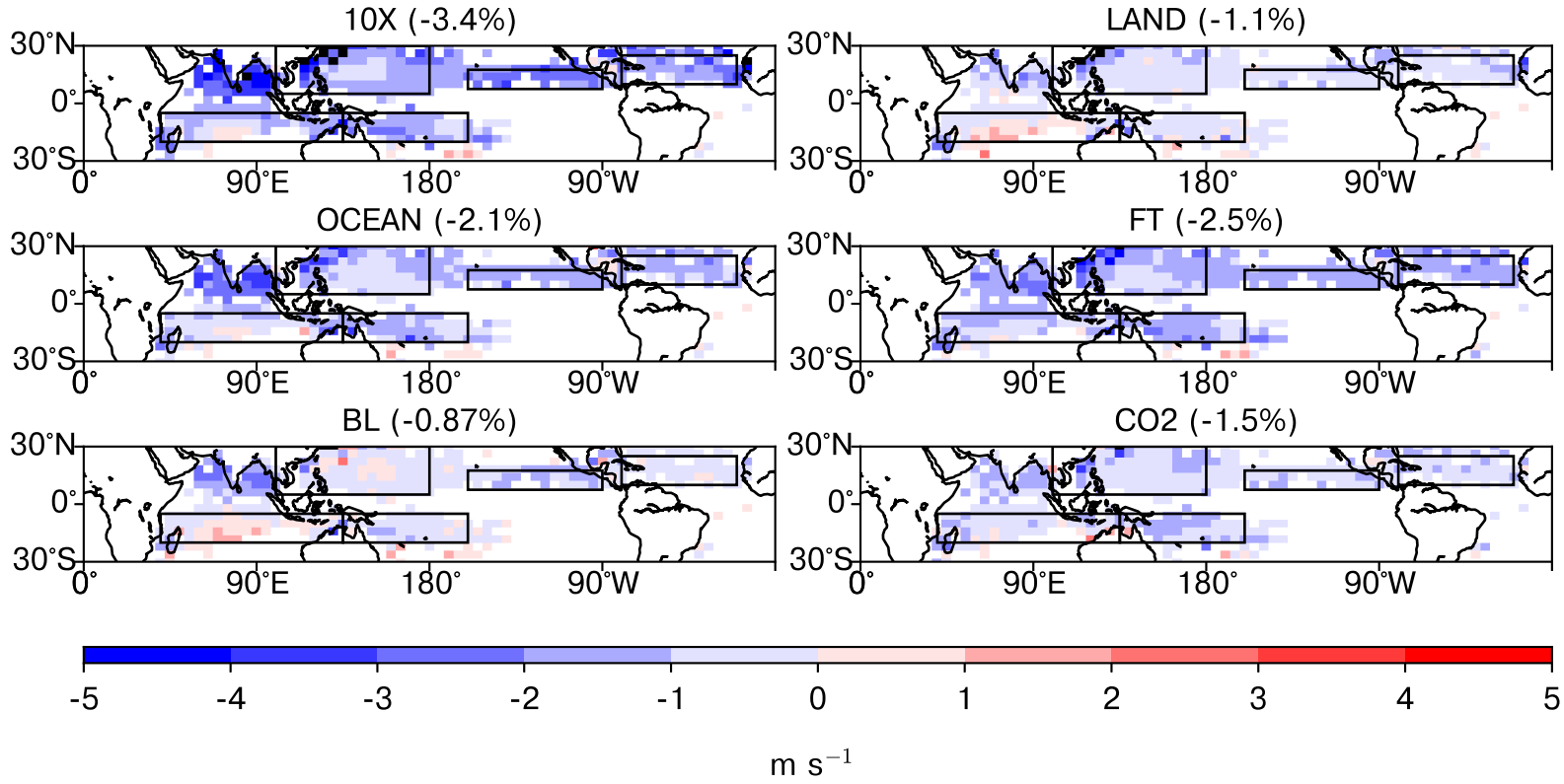


Figure 4.7: Same as Figure 4.5, but for potential intensity ($\mathcal{I}$, m s^{-1}).

To better delineate how atmospheric heating alters PI, we decompose it into two components, similar to Gilford et al. (2017). C_k/C_d is constant across our experiments because it is set to be consistent with the dissipative heating in HiRAM (Zhao et al., 2009). Thus the fractional change in PI can be written as:

$$\frac{\delta\mathcal{I}}{\mathcal{I}} = \frac{\delta\mathcal{T}}{2\mathcal{T}} + \frac{\delta\mathcal{E}}{2\mathcal{E}}. \tag{4.2}$$

It is clear from Table 4.3 that this linear decomposition holds reasonably well for all cases. The enthalpy difference term ($\delta\mathcal{E}$) roughly tracks the tropical-mean change in latent heating (Table 4.1), implying that genesis weighting favors latent heat more than sensible heat. This is understandable as TC genesis occurs over the oceanic regions of deep convection where moisture is in abundant supply. As explained above, the atmospheric energy balance dictates that imposed absorption, no matter where it is placed, would reduce the total surface flux, an effect manifested as decreases in $\mathcal{E}$ across all cases.

The thermodynamic efficiency term ($\delta\mathcal{T}$) is more variable than $\delta\mathcal{E}$ (Table 4.3). BL stands out as the only BC case in which it is substantially smaller than (about one quarter of) the corresponding enthalpy difference term. The same is also true for CO2. The two terms are within a factor of two for other cases. The setup of fixed surface temperature (T_s) means that any change in $\mathcal{T}$ is caused by different outflow temperature (T_o). In the simulations discussed here, genesis-weighted T_o match closely the average temperature at ∼100 hPa, where the thermal inversion marks the tropopause. Thus it is reasonable to think of the decrease in $\mathcal{T}$ as a consequence of the warming at 100 hPa, as opposed to a change of the outflow level. The vertical distributions of the tropical-mean changes in air temperature are plotted in Figure 4.8. In response to forced radiative heating (Figure 4.2), the troposphere undergoes modest warming, which is typically confined to be less than 0.5 K below

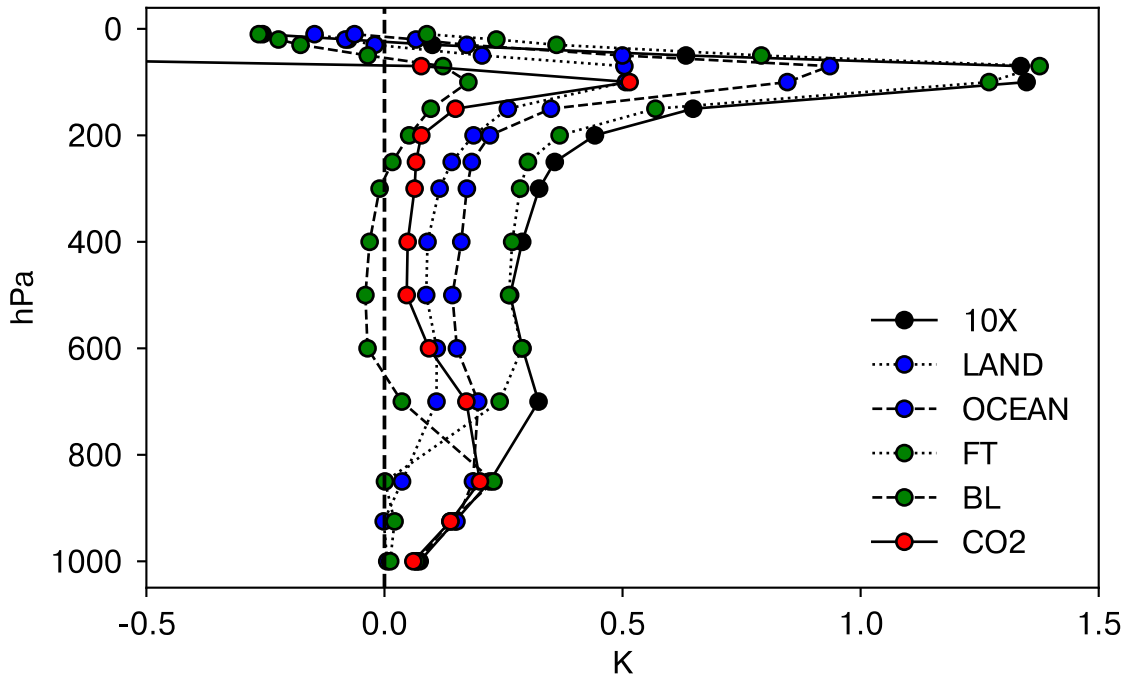


Figure 4.8: Vertical distributions of the tropical-mean changes in air temperature (K).

200 hPa by fixed surface temperature and moist adiabat. The surface control starts to loosen as one moves above 200 hPa (Lin et al., 2017). Strong warming is present in all non-BL cases, reaching about 1.4 K at 100 hPa in 10X and FL. The upper-tropospheric response is rather muted in BL. The warming caused by doubling CO_2 (about 0.5 K at 100 hPa) is in line with what Lin et al. (2017) found with a different GFDL model. These results can explain why atmospheric heating, when located in the free troposphere, causes the thermodynamic efficiency term to decrease.

The strong dependence of the TC response on the vertical structure of imposed absorption motivates us to examine the energy balance within the atmosphere's interior for the FT and BL cases (Figure 4.9). At each level, the BC-induced shortwave absorption increase (SW) must be compensated by changes in longwave radiation (LW), latent heating from the model's convection parameterization (CV) and large-scale cloud scheme (LS), and sensible heating from sub-grid vertical diffusion (VD) and

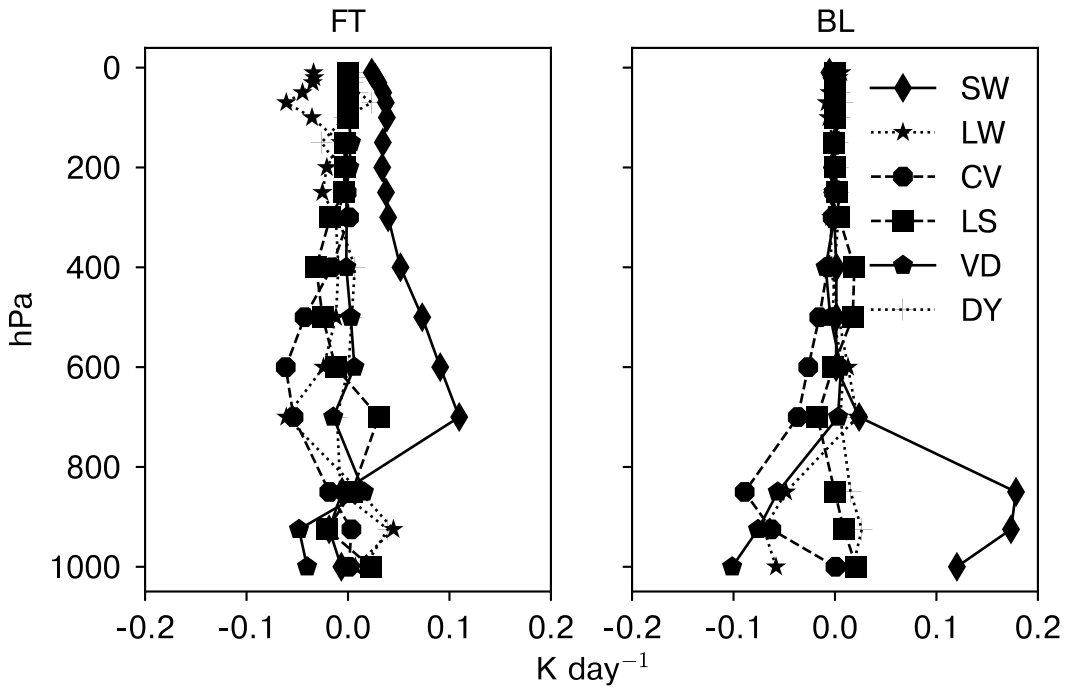


Figure 4.9: Tropical-mean changes in atmospheric heating rates (K day^{-1}) in FT and BL. They include shortwave radiation (SW), longwave radiation (LW), convective (CV) and large-scale (LS) latent heating, and vertical diffusion (VD) and dynamical advection (DY) of sensible heat.

grid-scale dynamical advection (DY). Note that the vertically-integrated advection term is practically zero, suggesting negligible change in atmospheric energy transport out of the tropics under fixed SST (Held, 2001).

For the FT case, the additional shortwave heating is balanced primarily through reducing convective and large-scale latent heating in the lower and mid-troposphere, the root cause of suppressed precipitation. Radiative to first order, the upper-tropospheric energy balance (above ∼100 hPa) is re-established by enhancing longwave cooling, which is realized through localized warming. In contrast, the reduction in sensible heating plays a leading role in counteracting boundary layer heating, while convective heating also decreases. These adjustments take place almost entirely within the boundary layer, and the upper troposphere is unchanged.

The PI decomposition also provides important insights into why BC over the ocean is more effective than that over the land in altering TCs. The tropical-mean contribution from latent heating in OCEAN is more than twice of that in LAND (Table 4.1) due to the abundance of moisture over the ocean. The role of latent heating is further amplified by genesis weighting, which favors the moist deep tropics over the dry subtropics. As a result, the decrease in the enthalpy difference term ($\delta\mathcal{E}$) in OCEAN is more than three times of that in LAND (Table 4.3). From the perspective of thermodynamic efficiency ($\delta\mathcal{T}$), the tropical-mean 100-hPa or outflow temperature (T_o) increase in OCEAN is about twice of that in LAND (Figure 4.8), approximately proportional to the shortwave heating rate (Figure 4.2). This is attributed to oceanic BC being more elevated, and gravity waves being effective at propagating temperature anomaly throughout the tropical free troposphere (Sobel et al., 2001).

4.4 Discussion

Although the initial perturbation by BC is entirely in the shortwave, the subsequent fast adjustment gives rise to a substantial reduction in longwave absorption (Table 4.1). In the 10X case, the magnitude of the latter is about 30% of the shortwave absorption. If one thinks of the longwave absorption as the divergence between surface and TOA fluxes, about half of δAL can be attributed to increased OLR, and the other half to decreased net surface longwave flux into the atmosphere. Both are linked partly to atmospheric warming. The clear- and cloud-sky components of δAL have similar magnitudes, and more interestingly, the latter takes place almost entirely over the ocean, which is even the case for LAND, indicating that BC tends to decrease high cloud cover (and thus increase OLR). The high cloud change can be ascribed to suppressed precipitation as high cloud cover and the associated longwave cloud radiative effect (CRE) are known to be tightly coupled to precipitation, both in

models and in observations (Hill et al., 2018). Note that CO_2 leads to an increase in shortwave absorption, which is coincidentally also 30% of the imposed longwave absorption (Table 4.1). This exclusively clear-sky effect suggests that higher water vapor concentrations may be the cause. Further effort is needed to understand why there is no change in CRE given the decreased precipitation.

The atmospheric energy balance argument does not distinguish shortwave and longwave absorption, and what matters is the combined effect. Our results confirm that the downstream impacts on precipitation and TC activities are indeed approximately proportional to the total (shortwave plus longwave) absorption. This is consistent with the reduction in mean precipitation and frequency of ascending motions in Chapter 2. In this sense, the aforementioned fast adjustment has a tendency to dampen the effect of BC, but enhance the effect of CO_2. This insight helps understand a key finding by Emanuel and Sobel (2013). In that study, the authors conducted a series of radiative-convective equilibrium simulations with a single column model, and showed that precipitation and PI are less sensitive to SST in CO_2 warming experiments than in prescribed SST experiments. We argue that the disparity can be thought of as a manifestation of the fast response to CO_2-induced absorption. Specifically, at $\sim$32X CO_2 ($\sim$37°C), the difference from 1X CO_2 with a prescribed SST of $\sim$37°C amounts to about 0.8 mm day^{-1} (or 23 W m^{-2}) in precipitation. Our work based on a GCM suggests a reduction in precipitation of 2.4 W m^{-2} per doubling of CO_2 or 12 W m^{-2} for 32X. Given how vastly different the two models are, it is encouraging to see that the simulated (inferred) fast responses to CO_2 agree with each other within a factor of 2.

In addition to the shared pathway of curtailing surface enthalpy supply, BC is more effective than CO_2 at altering the upper-tropospheric temperature and thus thermodynamic efficiency. This motivates us to conduct an experiment in which only BC above 200 hPa is increased by 10 times. The resulting warming is confined locally

with a magnitude comparable to 10X, while the surface enthalpy does not change. The fractional change of $\mathcal{E}$ is -1.7%, similar to what is in FT (-2.1%). While there is no statistically significant change in TC frequency in this experiment, the reduction in intensity is comparable to FT, especially for winds stronger than 35 m s^{-1}. Taken together, our results suggest that the thermodynamic efficiency term is more important than the enthalpy difference term in affecting TC intensity.

Although it is fully possible that the offline aerosol climatology used in HiRAM may overestimate the amount of upper-tropospheric BC (Koch et al., 2009), there are observational evidences suggesting that aerosols and their precursors can be transported to the upper troposphere and lower stratosphere by deep convection associated with Asian summer monsoon (Yu et al., 2017). Our work shows that the upper-tropospheric temperature is susceptible to even a small radiative perturbation, and the influence of regional aerosols can be felt throughout the tropics. Therefore, the elevated aerosols may have an important effect on TC formation even when they are relatively removed from the main development regions.

BC can potentially affect TCs through cloud microphysics, or the indirect effects. Although cloud processes (such as latent heat release and re-evaporative cooling) are central to TC dynamics, the indirect effects do not alter the atmospheric energetics or thermal structure directly. So, many of the intuitions developed here for radiative perturbations may not be applicable to microphysical perturbations. While HiRAM does not consider the indirect effects, some of the results of Chapter 3 might be potentially relevant to the GCM context. In particular, one might expect the increase in upper-tropospheric temperatures under increased cloud droplet number concentrations (Chapter 3) to reduce TC intensity.

4.5 Conclusions

This work addresses the direct radiative effect of BC on TC frequency and intensity with an atmospheric model capable of simulating a realistic TC climatology. We consider the impacts of a tenfold increase in BC as compared to CO_2 doubling, focusing on the differences that arise due to the magnitude and distribution of BC perturbations.

There are statistically significant decreases in TC frequency in all the BC cases with free-tropospheric perturbations, even when BC is placed solely over the land. In contrast, the boundary layer BC in isolation does not have an appreciable effect. The lowering of TC frequency correlate well with the reductions in convective activities, as measured by genesis-weighted precipitation and mid-tropospheric ascent. The latter is attributed to added free-tropospheric heating cutting down the need for latent heating. The boundary layer heating, on the other hand, is mostly communicated downward toward the surface by adjusting sensible heating.

As a characteristic difference between the two forcings, BC causes TC intensity to decrease substantively, while CO_2 does not. This cannot be explained by PI, as it shows similar decreases in response to the two forcings. An inspection of the thermodynamic efficiency term of PI indicates that BC, when placed in the upper troposphere, can induce significant warming locally, and thus lower the thermodynamic efficiency in a way that uniformly distributed CO_2 cannot. This suggest that thermodynamic efficiency may be particularly relevant to understanding TC intensity changes.

4.6 Acknowledgments

We thank Jenny Chang, Spencer Clark, Stephen Garner, and Ming Zhao for helpful discussion. Ming Zhao shared some of the code used in HZ11 which is used in the

analysis in this paper. Nadir Jeevanjee and David Paynter provided constructive internal reviews.

Chapter 5

The effect of surface warming on cold surges over the Maritime Continent

5.1 Introduction

The Maritime Continent (Ramage, 1968) comprises of the islands and their surrounding oceans that separate mainland Asia from Australia. Its position on the Western Pacific Warm Pool also makes it one of the rainiest locations on the globe (e.g. Wang et al., 2014a; Yamanaka et al., 2018), earning it the name of the "boiler-box" of the atmosphere (Simpson et al., 1993). During boreal winter (December to February, or DJF), the intense latent heat release over the Maritime Continent significantly impacts North America and northeast Eurasia weather through the generation of Rossby waves (Neale and Slingo, 2003).

Chang et al. (2005) identified cold surges to be a major synoptic contributor to boreal winter precipitation, alongside a quasi-stationary low-level vortex centered over Borneo (Cheang, 1977) and the Madden-Julian Oscillation (MJO). The surges

can be thought of as a consequence of Rossby waves (Lim and Chang, 1981; Chang et al., 2016) excited by the movements of the Siberian High (Ding, 1993). As the cold surge winds pass over the South China Sea, they are warmed and moistened by surface fluxes (Johnson and Houze, 1987). As such, the cold surges are linked to precipitation extremes in the Maritime Continent (Tangang et al., 2008; Pullen et al., 2015; Lim et al., 2017). Cold surges also interact with the other boreal winter synoptic features, serving to spin-up Borneo vortices (e.g. Koseki et al., 2014) and possibly aid the MJO in propagating across the Maritime Continent (Pang et al., 2018). Thus, cold surges have both direct and indirect influences on the boreal winter circulation.

Given the contributions of cold surges to both local precipitation and global latent heat release, it is important to understand how the behavior of such surges would change as the climate warms. An observational analysis reveals that the easterly component of the surges have strengthened from 1962-2007, with no significant change in the northerly component (Juneng and Tangang, 2010), which the authors suggest might be linked to trends in the Siberian High. Over the past few decades, trends in the Siberian High have switched from weakening over 1976-2000 (Gong and Ho, 2002) to strengthening from 1996-2015 (Zhao et al., 2018c), complicating attempts to connect trends in surges and Siberian High strength in observations. As yet, the issue of future changes in cold surge strength has yet to be examined in a GCM. One concern with using GCMs to study changes in Maritime Continent climate is the substantial bias in regional precipitation simulated by coupled GCMs (Raghavan et al., 2017).

As a first step, we use atmospheric GCMs with prescribed SSTs so as to eliminate effects of the bias from SSTs simulated by coupled models. For example, Toh et al. (2018) find that atmospheric GCMs outperform their coupled counterparts in simulating the global monsoon, which is linked to model skill in simulating precipitation over the Maritime Continent. In addition, the GFDL AM4 has a realistic climatology

of synoptic-scale features such as tropical cyclones (Zhao et al., 2018a) and monsoon depressions (Adames and Ming, 2018). Hence, we are encouraged to apply the model to studying the response of cold surges to surface warming.

Section 2 describes the methods used in this study. We evaluate AM4 in Section 3. The results of the warming perturbations are presented in Section 4, with a discussion and summary in Section 5.

5.2 Methods

5.2.1 Model, data and experiments

AM4 uses a finite-volume cubed-sphere dynamical core with 33 vertical levels (Zhao et al., 2018b). The double-plume scheme is based on the Bretherton et al. (2004) shallow convection scheme used in the GFDL HiRAM (Zhao et al., 2009), with a second plume to represent deep convection. The base AMIP (1979-2014) simulation (denoted by AM4) is performed using prescribed monthly SSTs and sea-ice concentrations at a horizontal resolution of 50 km. AM4 is evaluated using the daily (0000 UTC) zonal and meridional winds, specific humidity, temperature, and mean sea level pressure (MSLP) from ERA-interim, as well as the daily mean precipitation from TRMM 3B42 (1998-2014).

Two perturbation experiments are performed to examine the role of mean and spatial SST changes. In the 2K experiment, SSTs are increased uniformly by 2K. The P1 experiment makes use of warming and preindustrial simulations using the GFDL CM3 (Paynter et al., 2018). In the preindustrial CM3 simulation, all radiative forcing agents are set at 1850 levels. In the CM3 warming simulation, CO2 increases from the preindustrial level (286 ppmv) by 1% per year until doubling at year 70, after which CO_2 is held constant at 572 ppmv. The prescribed anomaly in the P1 experiment is the difference (warming minus preindustrial) in SSTs and sea ice averaged over years

70-100 of the CM3 simulations (personal communication, Paynter, 2019). After the introduction of the sea ice perturbation, the sea ice fractions prescribed in the P1 experiment were adjusted to be within zero and unity. The first year is discarded as spinup, and the remaining years (1980-2014) are used for analysis.

5.2.2 Definition of cold surges

The definition of a cold surge combines wind and sea level pressure indices, as suggested by Lim et al. (2017). The wind index is calculated using 850 hPa winds averaged over the latitude and longitude bounds of 5°-10°N and 107°-115°E (lower red box in Figure 5.1), while the pressure index is the maximum of MSLP over the latitude and longitude bounds of 18°-22°N and 105°-122°E (higher red box in Figure 5.1). The wind threshold for identification of a cold surge is set at 0.75 standard deviations above the long-term mean in the simulation climatology, calculated separately for ERA and each model simulation. Similarly, the pressure threshold is set at the long-term mean in the climatology for each simulation. In ERA, this time-mean sea level pressure is 1020 hPa, which is an operational threshold used in the region (Lim et al., 2017). A surge day occurs when the wind and pressure indices both exceed their respective thresholds.

5.2.3 Weather regime classification

Following Hassim and Timbal (2019) (HT19), eight weather regimes are identified by k-means clustering of standardized ERA reanalysis data from a 0.125° by 0.125° grid box over Singapore (1.375°N, 103.875°E) using temperature, specific humidity, zonal and meridional winds from 12 pressure levels: 1000, 925, 850, 700, 600, 500, 400, 300, 250, 200, 150 and 100 hPa. Similarly, eight weather regimes are identified in AM4 using data from the same pressure levels over the grid box containing Sin-

gapore. The standardization[1] (subtracting the mean and dividing by the standard deviation) makes the classification potentially sensitive to small changes (e.g. due to interpolation) in upper level specific humidity. To assess the robustness of the features identified by the regime analysis, we also perform the same classification by (i) excluding specific humidity above 300 hPa (S300), (ii) using data from only 1998-2014 (1998), (iii) using data from 1998-2014 and excluding specific humidity above 300 hPa (1998_S300). Since our focus is on DJF precipitation, we restrict our analysis to the three most frequent regimes in DJF. To aid comparison between AM4 and observations, the regimes are numbered in descending order of vertically-averaged relative humidity averaged over each regime.

5.2.4 Statistical significance

The significance of a change in weather regimes is evaluated with respect to the robustness of the feature across the sensitivity cases. Otherwise, significance is evaluated using a t-test at the 95% confidence interval, treating each season (DJF of each year) as an independent sample.

5.2.5 Moisture budget analysis

In steady state, the difference between DJF mean (overline) precipitation (P) and evaporation (E) is equal to the convergence of moisture flux (e.g. Li and Ting, 2017). In pressure coordinates, this is written as:

$$\overline{P} - \overline{E} = \nabla \cdot \int_{p_s}^{p_t} \frac{1}{g} \overline{\mathbf{u}q} dp, \tag{5.1}$$

where ∇ is the horizontal gradient operator, p_s is the lowest model level, p_t is the highest pressure level, $\mathbf{u}$ is the horizontal wind vector and q is specific humidity.

[1]Standardization should be distinguished from normalization, which returns values within the range of zero and unity.

Changes in Equation 5.1 can be written as a combination of changes in the mean circulation ($MC = \nabla \cdot \int_{p_s}^{p_t} \frac{1}{g} \overline{\mathbf{u}}\,\overline{q} dp$) and a residual ($RESID$) comprising of changes in transient eddies as well as changes in $P - E$, i.e.

$$\delta\overline{P} = \delta\overline{E} + \delta MC + \delta RESID \tag{5.2}$$

Changes in MC can then be decomposed into a thermodynamic (TD) component due to changes in mean moisture content ($\nabla \cdot \int_{p_s}^{p_t} \frac{1}{g} \overline{\mathbf{u}} \delta\overline{q} dp$) and a dynamic ($DY$) component from changes in mean circulation ($\nabla \cdot \int_{p_s}^{p_t} \frac{1}{g} \overline{q} \delta\overline{\mathbf{u}} dp$). The analysis is conducted with DJF-mean output.

5.3 Evaluation of AM4

5.3.1 Weather regimes

Figure 5.2 shows the representation of moisture (in the form of relative humidity (RH) and equivalent potential temperature θ_e), temperature and winds averaged over regimes 1-3 (R1-3) in OBS and AM4. Just as in OBS, R1 (R3) has a higher (lower) RH relative to climatology, with R2 being close to climatology (Figure 5.2a,e). Using equivalent potential temperature as a measurement of moisture (Figure 5.2b,f) yields the same qualitative conclusion. The northerly to northeasterly winds of the regimes are also captured well by AM4 (Figure 5.2c,g). Low level (e.g. below 800 hPa) temperatures are cold relative to climatology (Figure 5.2d,h). On the whole, it is encouraging that the qualitative differences between the thermodynamic (temperature, moisture) and dynamic (wind) quantities in the regimes are captured by AM4.

The precipitation averaged over R1-3 are shown in Figure 5.3. Of particular interest is R1, which is linked with surge rainfall (see dicussion of the Moist North East

regime in Hassim and Timbal, 2019). AM4 is able to capture the spatial variation in precipitation between regimes, with heaviest precipitation over the western Maritime Continent in R1 and the shift in precipitation to over the eastern/southeastern Maritime Continent in R2-3. The contrast in precipitation over the islands of Sumatra and Borneo (in R1) and the Philippines (R2) versus the surrounding ocean is sharper in OBS than in AM4.

Table 5.1: The relative frequency (fraction) of the three most frequent weather regimes in DJF, and their sum, in observations (OBS) and in AM4, in descending order of dryness (vertically-averaged relative humidity). Values significantly different from AM4 are in bold.

	OBS	AM4
R1	0.25	0.25
R2	**0.30**	0.24
R3	0.27	0.28
SUM	0.82	0.78

The frequency of weather regimes in DJF is presented in OBS and AM4 (Table 5.1). As an approximation, regimes R1-3 can be thought of as each occurring about 30% of the time. R1-R3 comprise the bulk (more than 78%) of the number of days in DJF, justifying our exclusion of the other regimes. Since our focus is on surge rainfall (R1), the frequency of R2 in AM4 being lower than in OBS is not a major concern. On the whole, we regard inter-regime variability as being represented adequately by AM4.

5.3.2 Cold surges

Over the Maritime Continent, we can think of DJF precipitation (P) as depending on the sum of precipitation from surge (P_s) and non-surge (P_n) events as well as the surge frequency (f_s):

$$P = f_s P_s + (1 - f_s) P_n. \tag{5.3}$$

Table 5.2: The mean and standard deviation (std) components of the wind index, the pressure index, and the surge frequency (f_s, unitless). Winds are given in m s^{-1} and SLP in hPa. Values significantly different from AM4 are in bold.

	OBS	AM4	2K	P1
Wind index (mean)	**8.4**	9.5	9.5	9.4
Wind index (std)	**2.7**	3.5	3.6	3.6
Pressure index	**1022**	1021	**1023**	**1022**
f_s	0.20	0.17	0.18	0.17

Table 5.2 lists the values of the indices in ERA (OBS) and in the model simulations, and the surge frequency. Both the mean and standard deviation components of the wind index is larger in the model simulations than in observations. There are also slight (1-2 hPa) differences in the pressure index across OBS and simulations. After incorporating the differences in wind and pressure into the threshold, there is no significant change in surge frequency across OBS and the simulations. In other words, AM4 has a realistic representation of the probability distribution of surge versus non-surge events.

The spatial pattern of P, P_s, and P_n in OBS are shown in Figure 5.1a-c, with the corresponding AM4 quantities in Figure 5.1d-f. The red boxes are the regions used to calculate the wind and pressure indices. In the simulation of mean precipitation P (Figure 5.1a,d), AM4 captures both the broad stretch of precipitation over 10°S-5°N, with northeasterly winds over the South China Sea. One caveat is that precipitation averaged over the seas around Borneo (black box, 5°S-10°N, 100-120°E) is 24% smaller in AM4 (5.7 mm day^{-1}) compared to OBS (7.5 mm day^{-1}). During surge days, precipitation increases by about 40% in AM4 to 7.9 mm day^{-1}, accompanied by a strengthening of northeasterly winds, just as in OBS (41% increase to 10.6 mm day^{-1}) (Figure 5.1b,e). Precipitation averaged over non-surge days (P_n) is distributed over 10°S-5°N (Figure 5.1c,f), similar to that of P . The surge anomalies in OBS (Figure 5.4) are more sharply aligned along the South China Sea than in AM4, presumably due to the coarse resolution of the island topography in AM4. Nevertheless, the

overall strengthening of the northeasterly surge flow confirms that AM4 performs a physically realistic simulation of the surge features.

5.4 Results

5.4.1 Temperature and precipitation

Figure 5.5 shows the changes in DJF surface temperature (T_s) in the warming experiments. Changes in global mean temperatures (parantheses in Figure 5.5) are approximately equal (within 0.2 K), and the Maritime Continent warms by close to 2 K (within 0.1 K) in both experiments. In the Arctic (60-90°N), the increase in T_s in P1 (11.2 K) is much larger than that in 2K (3.6 K), a substantial Arctic amplification that is more than four (4.4) times the increase in global mean T_s (2.5 K). The differences in surface temperature serve to influence the zonal-mean temperature structure of the atmosphere (Figure 5.6). In 2K, tropical (30S-30N) upper-tropospheric (300 hPa) temperatures increase by 4.2 K, greater than the increase in low-level (850 hPa) Arctic warming (3.0 K). The opposite is true in P1, where low-level Arctic warming (7.7 K) is almost double that of the tropical upper-tropospheric warming (4.0 K). The two experiments are therefore well-suited to comparing the influence of local versus remote SST changes on surge precipitation.

The changes in surge (P_s) and DJF precipitation (P) are shown in Figure 5.7. Warming increases P_s in both experiments (Figure 5.7a-b), with an enhancement of the northeasterly winds forming a cyclonic circulation over the South China Sea. The increase in surge precipitation around Borneo in P1 (2.5 mm day^{-1}) is almost double (79%) that of 2K (1.4 mm day^{-1}), with a sharper turning of the winds over the South China Sea. Just as in P_s, increases in P (Figure 5.7c-d) are also accompanied by strengthening of the northeasterly circulation. In both experiments, the fractional changes in surge precipitation and mean precipitation (values in parantheses) agree

to within 5%. This suggests that the DJF moisture budget is a useful way to gain insight into the mechanisms behind the changes in surge precipitation, as well as the differing responses between 2K and P1.

5.4.2 Moisture budget analysis

Figure 5.8a-d shows the changes in E, MC (Equation 5.2) and the decomposition of MC into TD and DY in 2K. The area-averaged value over the ocean around Borneo (black box) is given in the top left corner. The increased evaporation due to surface warming (Figure 5.8a) has little spatial structure over the oceans around Borneo. The largest contributor arises from the mean circulation MC, accounting for the spatial structure of P, as well as most (78%) of the increase in P (Figure 5.8b). In the ocean around Borneo, changes in $RESID$ (not shown) are the smallest term. Changes in MC come mostly from the thermodynamic (TD, Figure 5.8c) as opposed to the dynamic component (DY, Figure 5.8d). As such, the increase in precipitation in 2K can be thought of as a consequence of increased moisture availability due to surface warming, with circulation changes having a relatively small influence.

The corresponding terms for P1 are presented in Figure 5.8e-h. The increase in evaporation (Figure 5.8e) is approximately (within 0.1 mm day^{-1}) that of 2K (Figure 5.8a), consistent with the similar surface warming over the Maritime Continent (Figure 5.5). The difference between P1 and 2K is primarily attributed to the response of MC (Figure 5.8f), with small changes in $RESID$ (not shown). The TD component of MC in P1 is similar (within 0.1 mm day^{-1}) to that of 2K, with the difference arising almost entirely from the large increase (1.1 mm day^{-1}) in the DY component. This implies that in addition to the similar effects of increased moisture to those in 2K, P1 is also influenced by changes in the large scale circulation.

5.4.3 Connections with large-scale environment

A useful indicator of changes in the large-scale circulation is sea level pressure (SLP, Figure 5.9). In 2K, there is a SLP dipole pattern of a high over the extratropics and a low over the polar regions centered at approximately 50 N. When averaged over the Siberian High (rectangle, 40°-60°N, 80°-120°E, e.g. Wu and Wang, 2002), the change in sea level pressure (-0.3 hPa) is insignificant, consistent with the thermodynamic changes playing a larger role than the dynamic changes. In P1, the center of the SLP dipole shifts northward, increasing pressure over the whole Siberian High (2.4 hPa), consistent with the stronger dynamic component in the moisture budget of P1.

From hydrostatic balance, one would expect the changes in SLP to be related to temperature anomalies in the atmosphere. Figure 5.10 shows the changes in upper-tropospheric (300 hPa) temperature (contours) and winds (vectors). In 2K, there is an increase in the zonal mean jet favoring advection from west Eurasia into the region of the Siberian High, and temperatures over the Siberian High (parantheses) warm by 1.9 K. The winds take on an easterly component in P1, favoring southwestward advection of Arctic air towards the Siberian High. The temperature increase over the Siberian High in P1 is about half (1.1 K) of that in 2K, despite the similar changes in global-mean temperature. Similarly, in the lower troposphere (700 hPa, Figure 5.11), the temperature change over the Siberian High is smaller in P1 than in 2K, accompanied by easterly winds.

5.5 Conclusions

5.5.1 Discussion

Given that the forcings in our experiments differ most over the Arctic, it is reasonable to attribute the differences in circulation to the extent of Arctic warming.

Indeed, modeling studies forced with sea ice reductions over the Barents-Kara seas have exhibited a pattern of warming over the Arctic and a cooling over Eurasia, and a strengthening of the Siberian High, with various different explanations being proposed. Kim et al. (2014) propose that sea-ice loss increases the intensity of upward propagating wave activity that weakens the stratospheric polar vortex. They suggest that the weakened polar vortex favors a negative phase of the Arctic oscillation, which is known to correlate with increased strength of the Siberian High in observations (Wu and Wang, 2002). Honda et al. (2009) have suggested that heat fluxes from areas of sea ice loss can trigger stationary Rossby waves that favor southwestward advection of cold anomalies into the region of the Siberian High. Both these mechanisms appear consistent with the jet and temperature changes in Figure 5.10.

We also caution that the response in P1 should not be taken as representative of all models. In general, coupled models disagree on the sign of wintertime changes in zonal-mean wind and jet speed, at least over the North America/North Atlantic region (Barnes and Polvani, 2015). As a specific example, the global warming experiment of Lu et al. (2008) has similar (about 4 K) warming in both the tropical upper-troposphere and the Arctic lower-troposphere, and predicts a strengthening of mid-latitude zonal mean winds around 50°N. In this respect, the response in their experiment is more similar to our 2K experiment than our P1 experiment. Instead, we hope that our work will motivate further research on constraining the effects of Arctic changes on the deep tropics.

5.5.2 Summary

We examine the response of boreal winter cold surges over the Maritime Continent to surface warming using an atmospheric GCM forced with a uniform and realistic scenario of sea surface warming. The realistic scenario features a strong Arctic amplification pattern. Surge precipitation increases in both warming experiments, with

a larger increase in the realistic scenario. The increase in surge rainfall can be interpreted as an enhanced version of the increase in DJF precipitation over the Maritime Continent. In the uniform warming scenario, the increase in precipitation can be mainly attributed to increases in evaporation and increased moisture advection by change in the moisture gradient. In addition to these effects, the realistic scenario features a large increase in moisture advection from a strengthening of the north-easterly winds, consistent with a greater strengthening of the Siberian High. The projected enhancement of boreal winter precipitation over the Maritime Continent has implications for both local precipitation extremes as well as the teleconnections over the extratropics.

5.6 Acknowledgments

Huan Guo and Spencer Clark provided assistance with AM4. The P1 pattern was supplied by David Paynter. Muhammad Hassim provided the scripts and data used in HT and helpful discussion on the regime technique. We also thank Jenny Chang, Xianan Jiang, and Lei Wang for their suggestions.

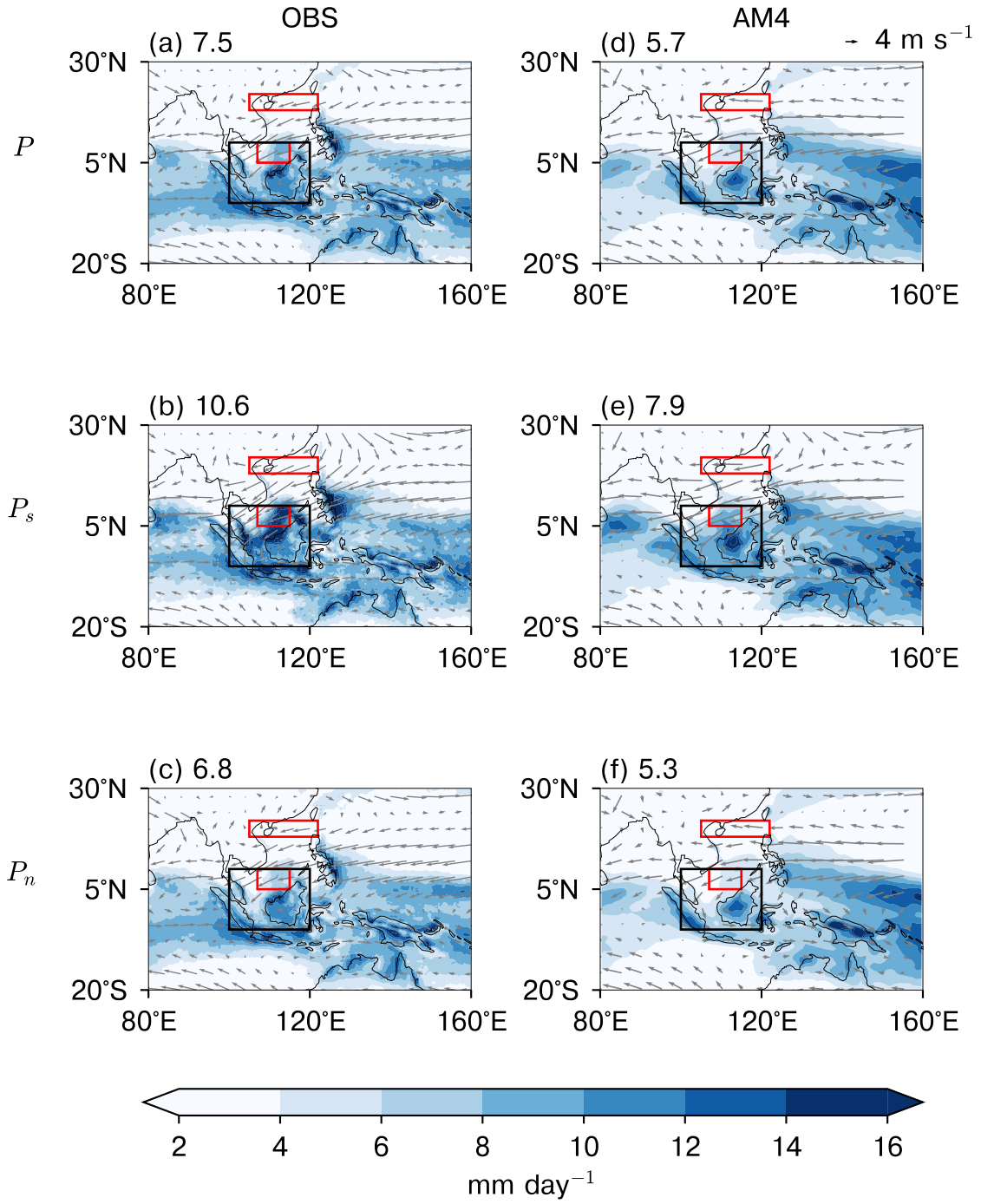


Figure 5.1: Precipitation (mm day^{-1}, contours) and low-level (850 hPa) winds (m s^{-1}, vectors) averaged over all (a) DJF days (b) surge days (c) non-surge days. The precipitation averaged over the oceans around Borneo (within the black box) is given in the top left hand corner. The red boxes are used in the definition of the surges (see Methods). (d-f) As in (a-c), but for AM4.

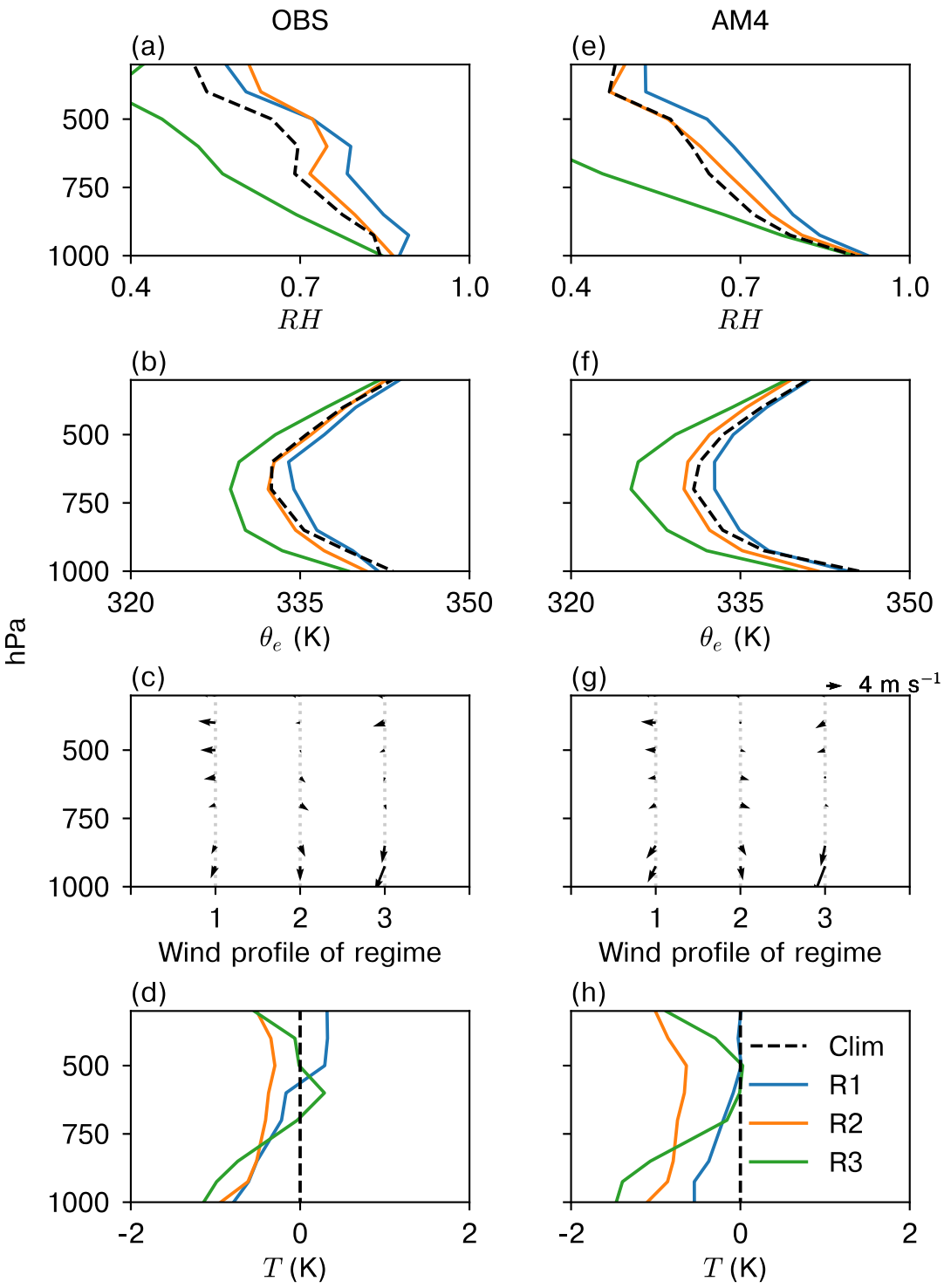


Figure 5.2: Climate variables used to perform the weather regime classification in OBS: (a) relative humidity (RH, fraction), (b) equivalent potential temperature (θ_e, K), (c) wind vectors (m s^{-1}), (d) temperature anomalies relative to the annual mean (K). The dashed lines represent the annual climatological mean. (e-h) As in (a-d), but for AM4.

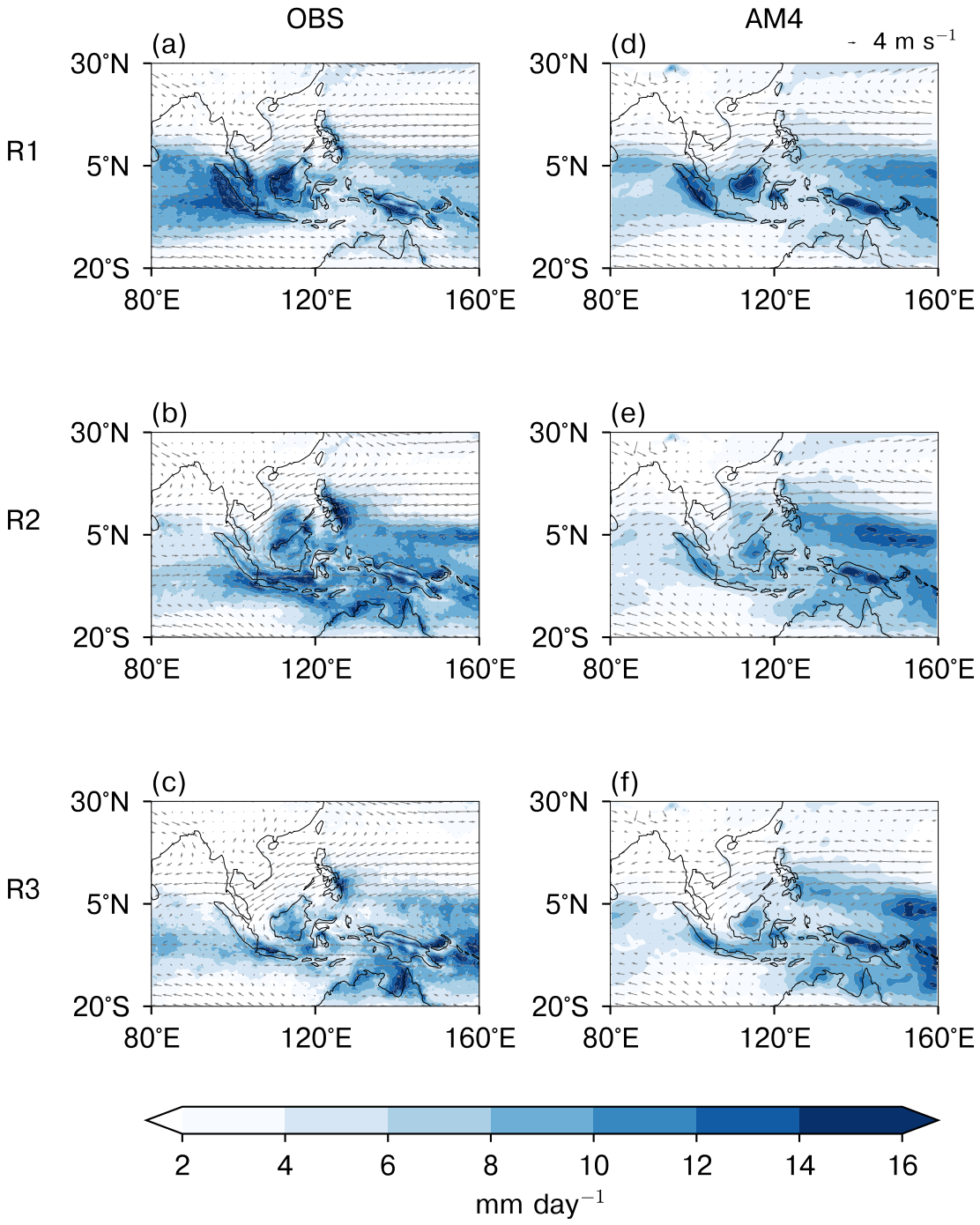


Figure 5.3: (a-d) Precipitation (mm day^{-1}, contours) and low-level (850 hPa) winds (m s^{-1}, vectors) averaged over the days in R1-R4 in OBS, respectively. (e-h) As in (a-d), but in AM4.

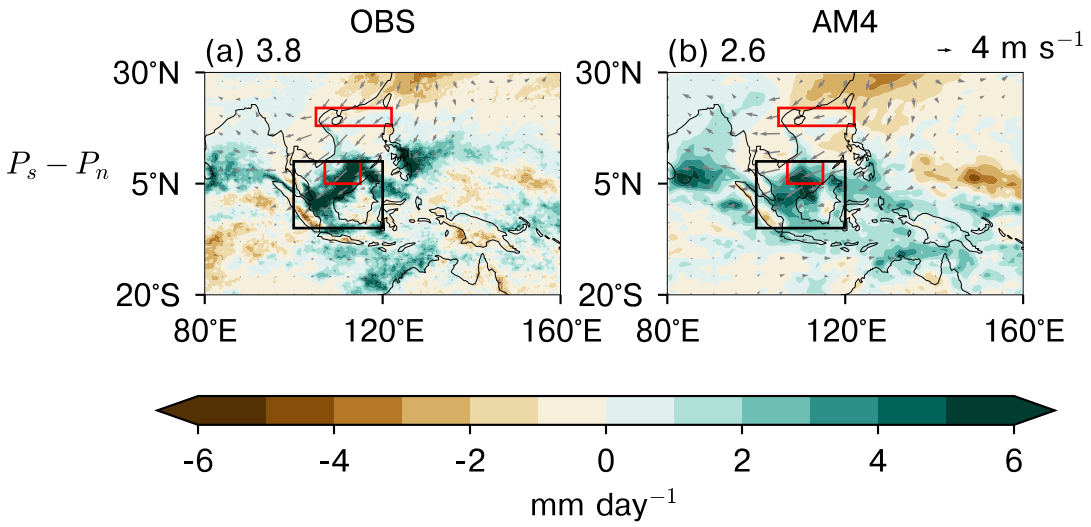


Figure 5.4: (a) Precipitation (mm day^{-1}, contours) and low-level (850 hPa) winds (m s^{-1}, vectors) due to surges in OBS (i.e. (b)-(c) in Figure 5.1). (b) As in (a), but for AM4. The precipitation averaged over the oceans around Borneo (within the black box) is given in the top left hand corner. The red boxes are used in the definition of the surges (see Methods).

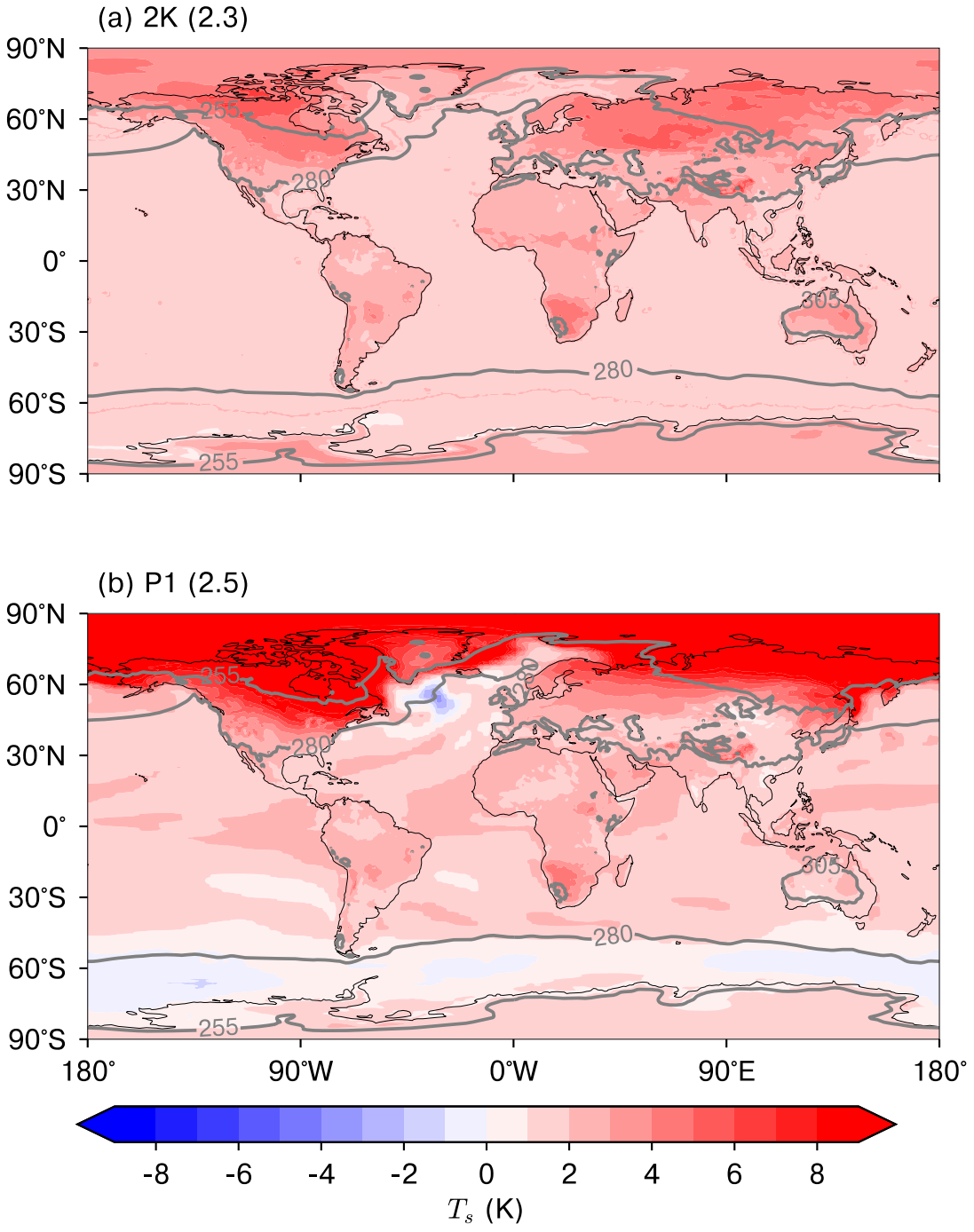


Figure 5.5: Geographical distribution of changes in DJF surface temperature (T_s, K) in (a) 2K (b) P1. The global mean temperature change is given in parentheses.

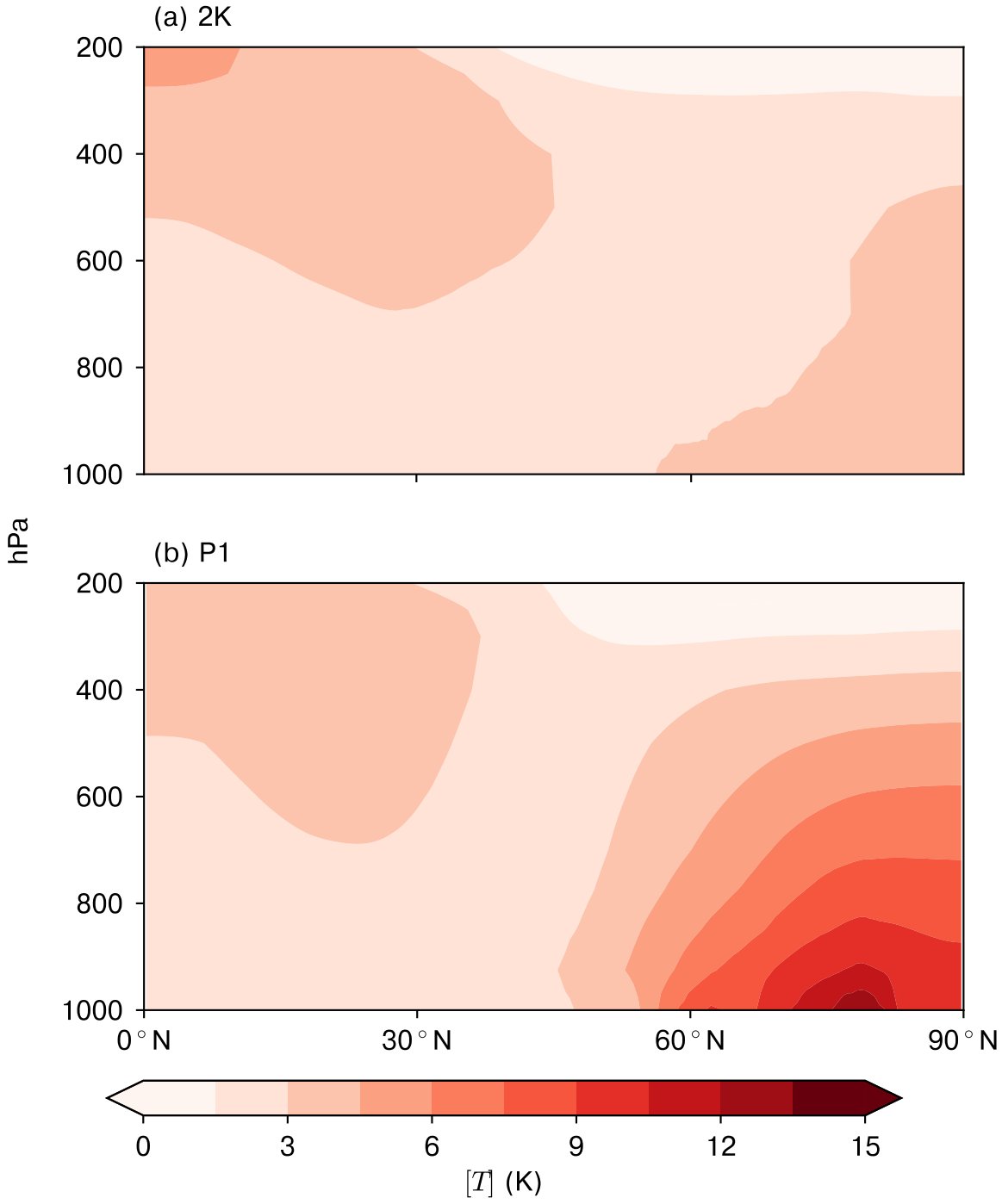


Figure 5.6: Zonal-mean DJF temperature changes in the Northern Hemisphere ($[T]$, K) in (a) 2K (b) P1.

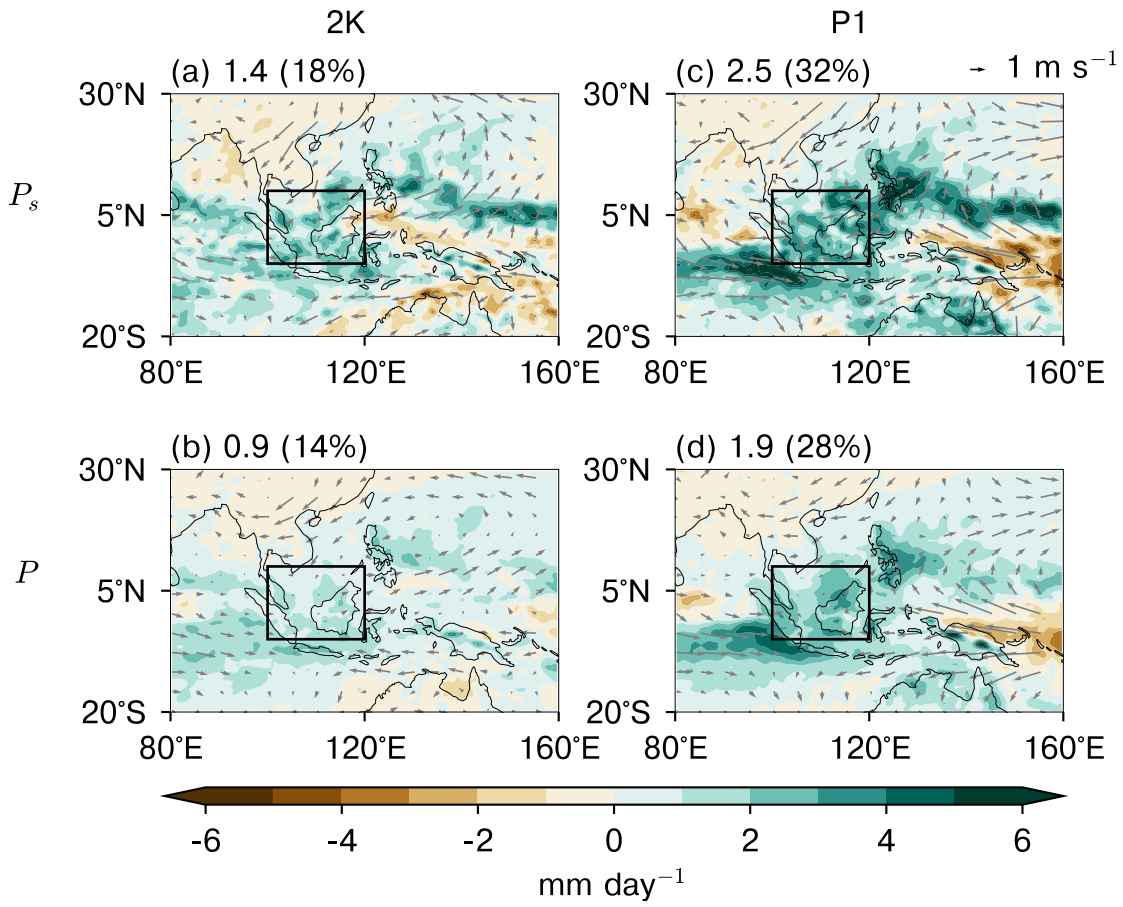


Figure 5.7: The changes in (a) surge and (b) DJF precipitation (mm day^{-1}, contours) and 850 hPa winds (m s^{-1}, vectors) in 2K. The percentage increase in precipitation over the ocean around Borneo (box) is given in the top left corner, with the percentage increase in parantheses. (c-d) As in (a-b), but for P1.

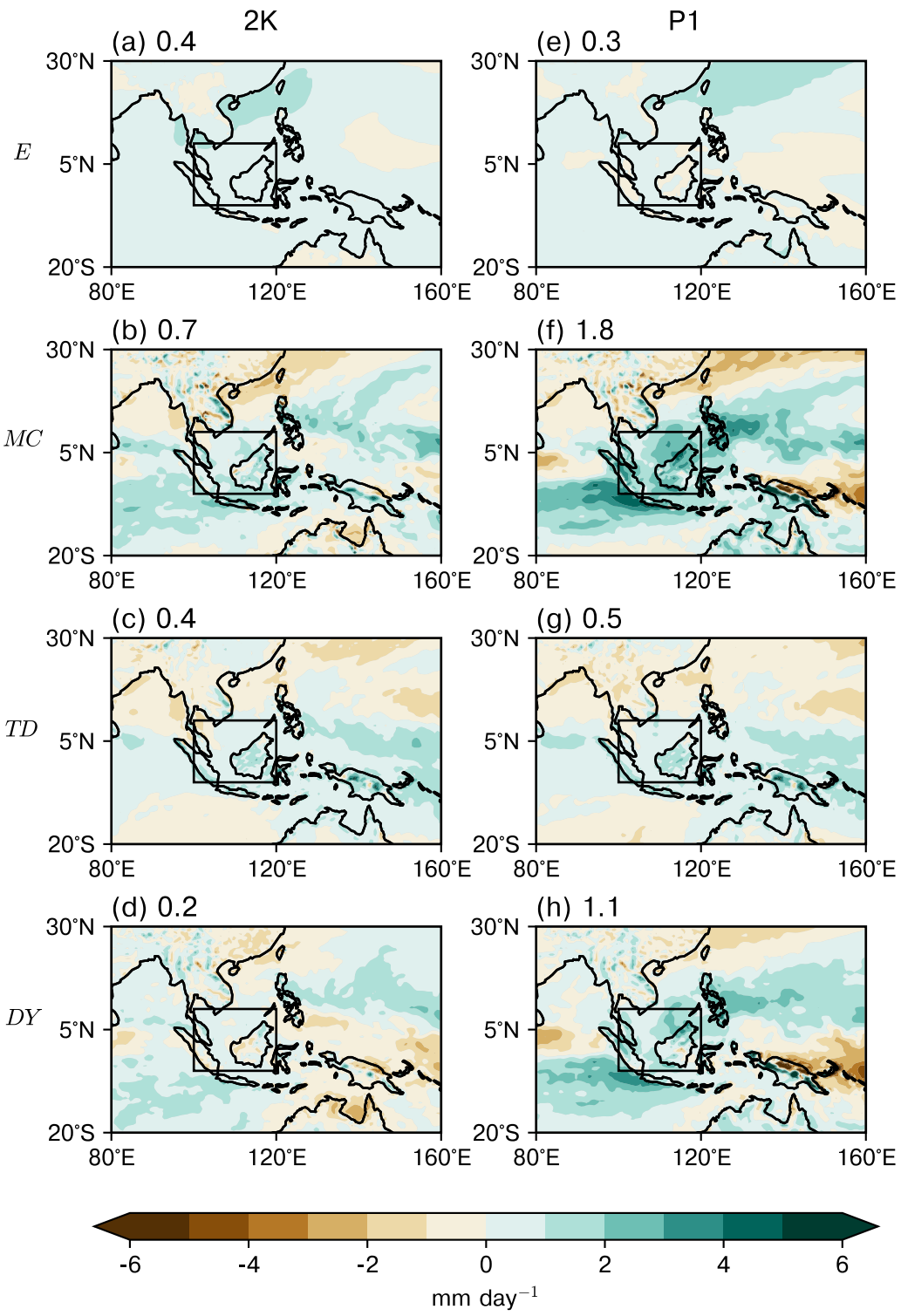


Figure 5.8: Changes in (a) evaporation (E), (b) advection of moisture by the mean circulation (MC) and its (c) thermodynamic (TD) and (d) dynamic (DY) components in 2K. Values averaged over the surge area (box) are given in the top left corner. (e-h) As in (a-d) but for P1. All values are in mm day^{-1}.

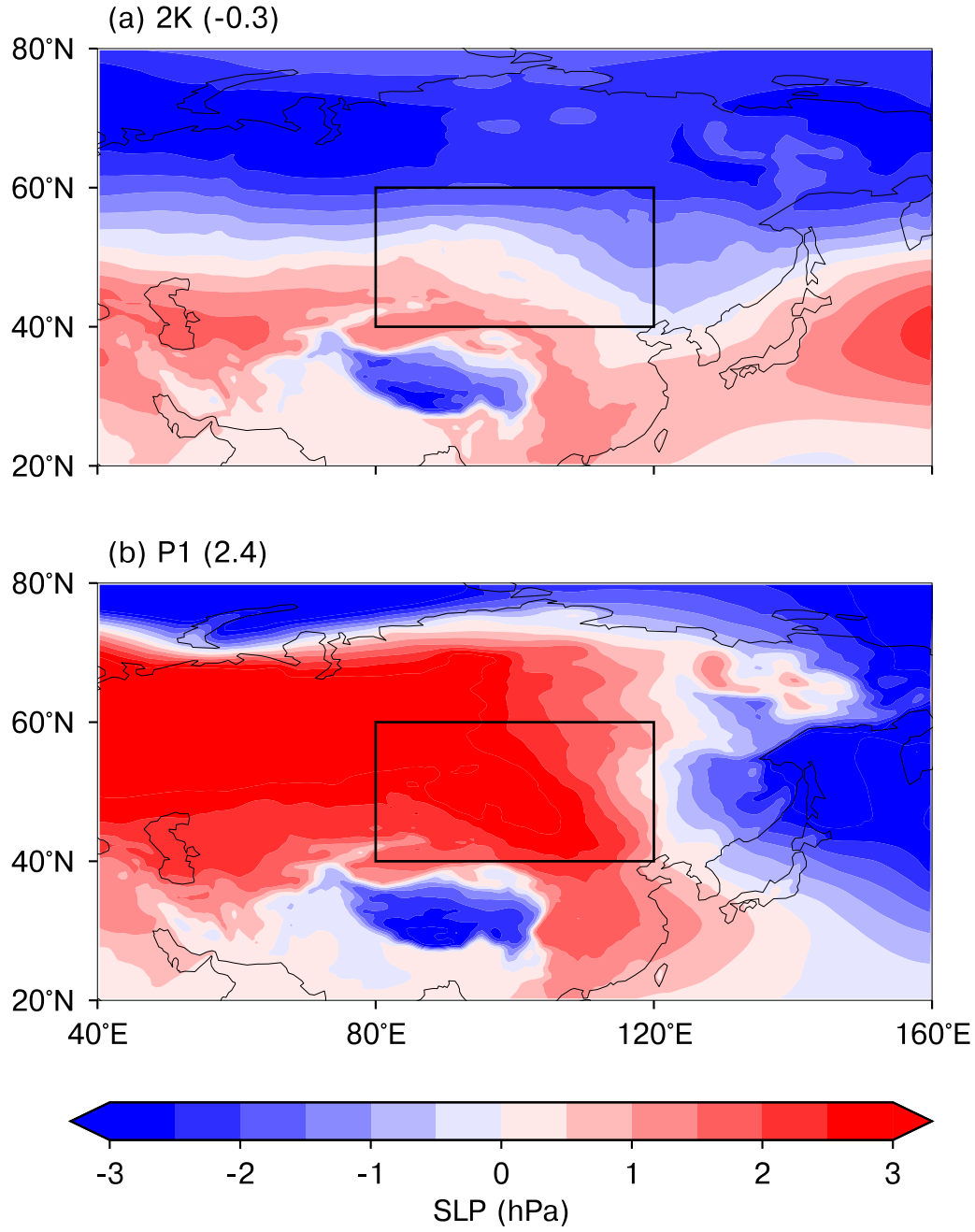


Figure 5.9: Geographical changes in sea level pressure (SLP, hPa) for (a) 2K and (b) P1 in DJF. Changes averaged over the Siberian High (rectangle) are given in parantheses.

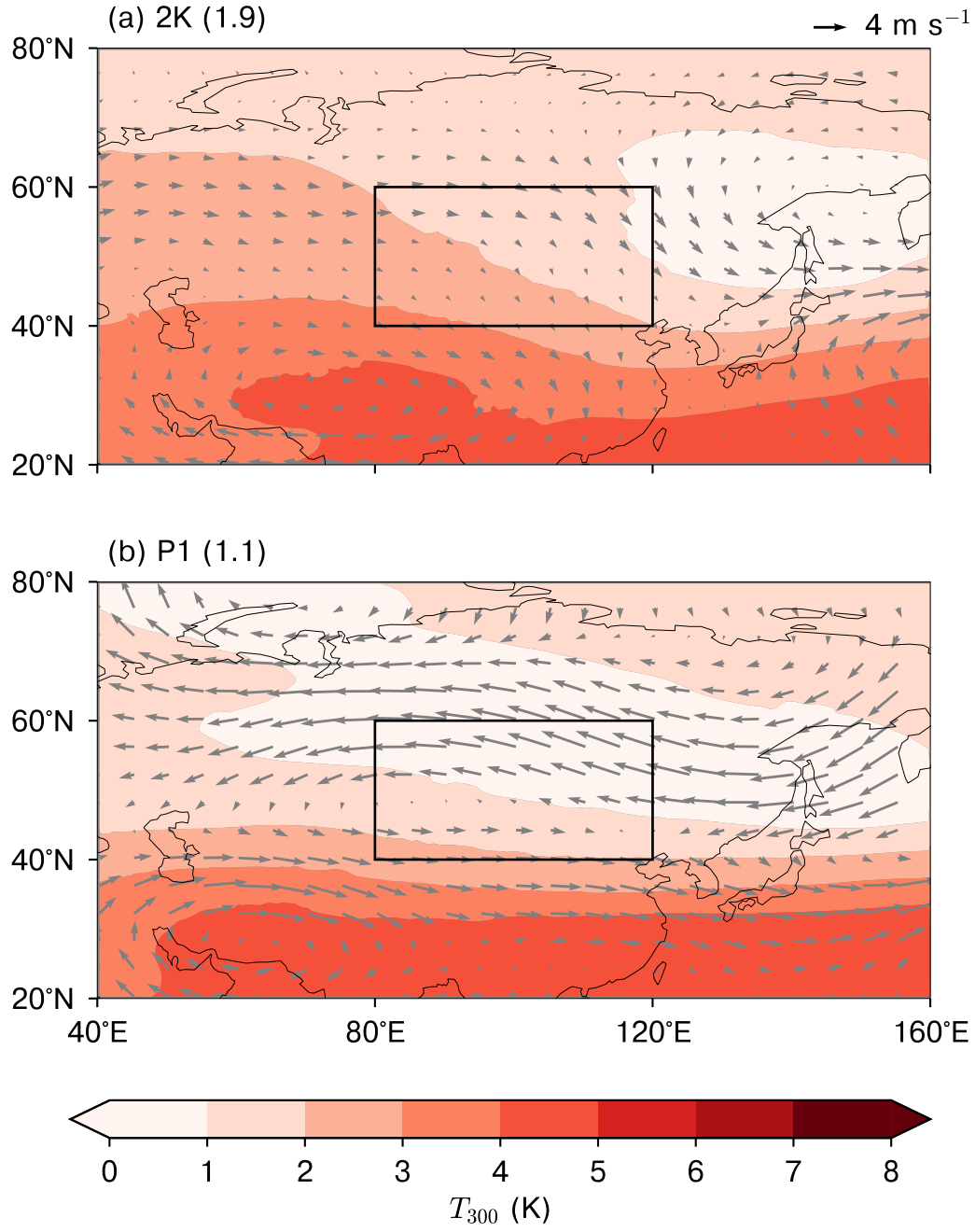


Figure 5.10: Geographical changes in 300 hPa temperature (T_{300}, K) (contours) and winds (vectors) for (a) 2K and (b) P1 in DJF. Temperature changes averaged over the Siberian High (rectangle) are given in parantheses.

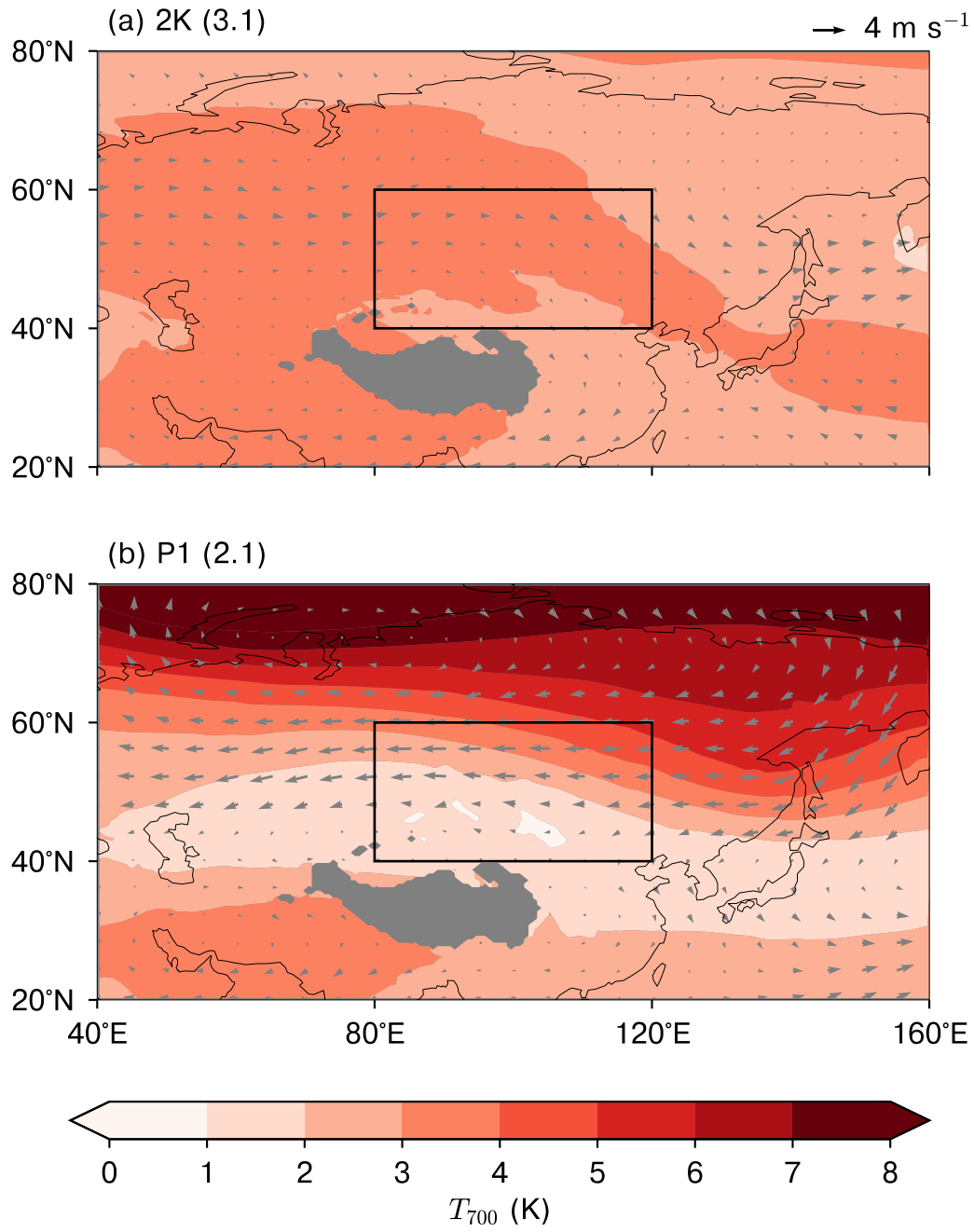


Figure 5.11: As in Figure 5.10, but for 700 hPa temperature (T_{700}, K). Missing values due to the presence of topography have been masked in gray.

Chapter 6

Conclusions

6.1 Summary and implications

Greenhouse gases and absorbing aerosols are the strongest anthropogenic sources of radiative heating. In addition, aerosols alter cloud droplet number concentrations, thereby affecting cloud microphysical processes. The thesis explores the role of both small-scale atmospheric processes (Chapters 2-3) and the large-scale circulation response (Chapters 4-5) in shaping the response of tropical precipitation to these major forcings.

Chapters 2-3 make use of cloud-resolving model simulations in the setting of radiative-convective equilibrium to uncover the mechanisms through which the atmosphere responds to radiative and microphysical perturbations such as those caused by aerosols and greenhouse gases. In Chapter 2, we find that the decrease in mean rainfall under atmospheric heating in simulations with a cloud-resolving model is largely achieved by a reduction in weak events. The precipitation from strong events is maintained by a cancellation between increases in boundary layer moisture and reduction in updraft frequencies. A boundary layer energy analysis finds that the free-tropospheric heating is mostly communicated to the boundary layer through re-

ducing re-evaporation, and a predictive theory for changes in sensible heat is proposed. The results have implications for both predictions of future changes in the intensity distribution of precipitation as well as analytic theories of boundary layer climate sensitivity.

Chapter 3 shows that an increase in cloud droplet number concentrations due to elevated aerosol concentrations can increase convective mass flux even in the absence of ice microphysical processes. Further sensitivity tests indicate that the extent of this convective invigoration depends more strongly on the evaporation of cloud condensates as opposed to rain condensates. Based on microphysical and energetic considerations, we propose a mechanism through which the increased cloud droplet number concentrations affect the convective mass flux. The identification of the key microphysical processes underlying convective invigoration will aid model developers and users in selecting the appropriate amount of microphysical complexity in their examination of aerosol-convection interactions.

Chapters 4-5 present results with comprehensive global climate models forced with idealized atmospheric and surface perturbations reflecting the heating impacts of greenhouse gases and absorbing aerosols. In Chapter 4, simulations from the GFDL HiRAM indicate that a tenfold increase of black carbon reduces tropical cyclone (TC) frequency by 21%. Sensitivity experiments are conducted to examine the relative importance of the spatially inhomogenous horizontal and vertical distributions of black carbon. Both black carbon over land and ocean contribute significantly to the overall reduction, whereas boundary layer black carbon has no appreciable effect compared to free-tropospheric black carbon. The reduction in TC frequency can be related to the reduction in latent heating and the simultaneous weakening of the mid-tropospheric vertical velocity. Black carbon also reduces TC intensity, whereas a doubling of CO_2 does not. The results are qualitatively in agreement with the changes in potential intensity. Black carbon reduces potential intensity both through

an increase in outflow temperatures and by moistening the boundary layer. The warming lowers thermodynamic efficiency, which is consistent with the decreases in intensity. This suggests that the mechanisms by which aerosols affect extreme weather events might be more complex than that of well-mixed greenhouse gases.

Chapter 5 examines the response of boreal winter cold surges over the Maritime Continent to uniform and realistic sea surface warming. Surge precipitation increase in both warming experiments, with a larger increase in the realistic scenario. The increase in precipitation in the uniform warming case is attributed to increases in evaporation and increased moisture advection from a moister atmosphere. In addition to these effects, the realistic scenario shows effects from a strengthening of the northeasterly winds, consistent with a strengthening of the Siberian High. The results suggest that Arctic temperature changes may play a significant role in altering boreal winter precipitation over the Maritime Continent, and its resulting teleconnections to the extratropics.

6.2 Limitations and future work

Throughout this thesis, we have conceptually separated the response of tropical precipitation into fast and slow timescales, where sea surface temperatures are only allowed to change in the latter. In practice, this separation is not perfect, and the atmospheric absorption can modify local SSTs on the convective overturning timescale (20-30 days). One can estimate the magnitude of the temperature warming by considering the heat capacity of the mixed layer (e.g. Schollaert and Merrill, 1998); as an upper bound, given a surface cooling of 10 W m^{-2} and assuming a mixed layer depth of 20 m, SSTs would cool by 0.3 K per thirty days. The changes in surface temperature would introduce an additional feedback to the atmospheric balance. An

interesting extension to this work would be to compare our results with those of a coupled ocean model.

Additional feedbacks must be considered when seeking to relate the idealized simulations in Chapters 2 and 3 to the full climate system. The prescribed radiation does not account for the radiative feedback of the changes of clouds and water vapor to heating. For example, the decrease in cloud cover would facilitate longwave cooling from the surface to space, while the increase in water vapor would increase the absorption of radiation. It is also known that updraft speeds themselves are a major control on cloud droplet number concentration (Donner et al., 2016). Changes in precipitation would also affect the removal of aerosols by wet deposition. Given the ease with which one can utilize different physical parameterizations in WRF, a next step would be to perform experiments that systematically build from the idealized configuration towards a more realistic configuration. That would allow us to assess the extent to which the response reflects forcings, as opposed to feedbacks.

The resolutions of our simulations should also be considered in the interpretation of the results. Chapters 2 and 3 make use of simulations at a resolution of 2 km, which might not completely resolve fine scale storm structures such as unsaturated downdrafts within a convective event (e.g. Emanuel, 1981). These unsaturated downdrafts could act to cool the boundary layer by modifying the exchange between the free troposphere and boundary layer . It is possible that simulations at a much higher resolution (on the order of 100m or less) would reveal a different balance between the roles of re-evaporative cooling and exchange with the free troposphere.

The analysis of Chapter 4 focuses only on the direct effect of absorbing aerosols. In light of the convective invigoration discussed in Chapter 3, it is possible that the indirect effect would act to increase TC frequency. Simulations with interactive radiation could further be used to assess if forcings in shortwave versus longwave

might have effects on tropical cyclones via cloud feedbacks, or if the influence on TCs is only due to the temperature changes in the upper troposphere.

While Chapter 5 has shown that high-resolution GCMs have skill in capturing aspects of the boreal winter monsoon over the Maritime Continent, it is known that resolution is not the only factor that controls model performance over this region (Toh et al., 2018). The process of improving estimates of hydroclimate change over the region will rely both on improvements at the process level and using observational constraints to exclude models with unrealistic simulations over the area. High-resolution regional models can be used to determine the key surface and ocean processes that need to be resolved in order to capture intraseasonal variability in the Maritime Continent (e.g. Office of Naval Research, 2017), thereby directing the development of future GCMs. In the meantime, examining the physical processes simulated by the GCMs, as in Chapter 5, will guide the selection of GCMs for the purpose of predicting regional climate change.

Bibliography

Adames, Á. F. and Ming, Y. Moisture and moist static energy budgets of South Asian monsoon low pressure systems in GFDL AM4. *Journal of the Atmospheric Sciences*, (2018), 2018.

Albrecht, B. A. Aerosols, cloud microphysics, and fractional cloudiness. *Science*, 245 (4923):1227, Sep 15 1989.

Allen, M. R. and Ingram, W. J. Constraints on future changes in climate and the hydrologic cycle. *Nature*, 419(6903):224–232, 2002.

Andreae, M. O., Rosenfeld, D., Artaxo, P., Costa, A., Frank, G., Longo, K., and Silva-Dias, M. A. F. d. Smoking rain clouds over the Amazon. *Science*, 303(5662): 1337–1342, 2004.

Andrews, T. and Forster, P. M. The transient response of global-mean precipitation to increasing carbon dioxide levels. *Environmental Research Letters*, 5(2):025212, 2010.

Andrews, T., Forster, P. M., Boucher, O., Bellouin, N., and Jones, A. Precipitation, radiative forcing and global temperature change. *Geophysical Research Letters*, 37 (14), 2010.

Bala, G., Caldeira, K., and Nemani, R. Fast versus slow response in climate change: implications for the global hydrological cycle. *Climate Dynamics*, 35(2-3):423–434, 2010.

Ball, F. Control of inversion height by surface heating. *Quarterly Journal of the Royal Meteorological Society*, 86(370):483–494, 1960.

Barnes, E. A. and Polvani, L. M. CMIP5 projections of Arctic amplification, of the North American/North Atlantic circulation, and of their relationship. *Journal of Climate*, 28(13):5254–5271, 2015.

Betts, A. Non-precipitating cumulus convection and its parameterization. *Quarterly Journal of the Royal Meteorological Society*, 99(419):178–196, 1973.

Betts, A. K. Idealized model for equilibrium boundary layer over land. *Journal of Hydrometeorology*, 1(6):507–523, 2000.

Betts, A. K. and Ridgway, W. Climatic equilibrium of the atmospheric convective boundary layer over a tropical ocean. *Journal of the Atmospheric Sciences*, 46(17): 2621–2641, 1989.

Bister, M. and Emanuel, K. A. Dissipative heating and hurricane intensity. *Meteorology and Atmospheric Physics*, 65(3):233–240, 1998.

Bister, M. and Emanuel, K. A. Low frequency variability of tropical cyclone potential intensity 1. Interannual to interdecadal variability. *Journal of Geophysical Research: Atmospheres*, 107(D24), 2002.

Bollasina, M., Nigam, S., and Lau, K. Absorbing aerosols and summer monsoon evolution over South Asia: An observational portrayal. *Journal of Climate*, 21(13): 3221–3239, 2008.

Bond, T. C., Doherty, S. J., Fahey, D., Forster, P., Berntsen, T., DeAngelo, B., Flanner, M., Ghan, S., Kärcher, B., Koch, D., et al. Bounding the role of black carbon in the climate system: A scientific assessment. *Journal of Geophysical Research: Atmospheres*, 118(11):5380–5552, 2013.

Boucher, O., Randall, D., Artaxo, P., Bretherton, C., Feingold, G., Forster, P., Kerminen, V.-M., Kondo, Y., Liao, H., Lohmann, U., et al. Clouds and aerosols. In *Climate Change 2013: the Physical Science Basis. Contribution of Working Group I to the Fifth Assessment Report of the Intergovernmental Panel on Climate Change*, pages 571–657. Cambridge University Press, 2013.

Bretherton, C. S., McCaa, J. R., and Grenier, H. A new parameterization for shallow cumulus convection and its application to marine subtropical cloud-topped boundary layers. Part I: Description and 1D results. *Monthly Weather Review*, 132(4): 864–882, 2004.

Bretl, S., Reutter, P., Raible, C. C., Ferrachat, S., Poberaj, C. S., Revell, L. E., and Lohmann, U. The influence of absorbed solar radiation by Saharan dust on hurricane genesis. *Journal of Geophysical Research: Atmospheres*, 120(5):1902–1917, 2015.

Camargo, S., Sobel, A., Barnston, A. G., and Emanuel, K. Tropical cyclone genesis potential index in climate models. *Tellus*, 59A:428–443, 2007a.

Camargo, S., Sobel, A., Barnston, A. G., and Emanuel, K. Tropical cyclone genesis potential index in climate models. *Tellus*, 59A:428–443, 2007b.

Carslaw, K., Lee, L., Reddington, C., Pringle, K., Rap, A., Forster, P., Mann, G., Spracklen, D., Woodhouse, M., Regayre, L., et al. Large contribution of natural aerosols to uncertainty in indirect forcing. *Nature*, 503(7474):67–71, 2013.

Chang, C., Erickson, J., and Lau, K. Northeasterly cold surges and near-equatorial disturbances over the winter MONEX area during December 1974. Part I: Synoptic aspects. *Monthly Weather Review*, 107(7):812–829, 1979.

Chang, C., Harr, P. A., and Chen, H.-J. Synoptic disturbances over the equatorial South China Sea and western Maritime Continent during boreal winter. *Monthly Weather Review*, 133(3):489–503, 2005.

Chang, C.-P., Lu, M.-M., and Lim, H. Monsoon convection in the Maritime Continent: interaction of large-scale motion and complex terrain. *Meteorological Monographs*, 56:6–1, 2016.

Cheang, B. K. Synoptic features and structures of some equatorial vortices over the South China Sea in the Malaysian region during the winter monsoon, december 1973. *Pure and Applied Geophysics*, 115(5-6):1303–1333, 1977.

Chen, D., Liu, Z., Davis, C., and Gu, Y. Dust radiative effects on atmospheric thermodynamics and tropical cyclogenesis over the Atlantic Ocean using WRF-Chem coupled with an AOD data assimilation system. *Atmospheric Chemistry and Physics*, 17(12):7917, 2017.

Chen, J.-M., Li, T., and Shih, C.-F. Tropical cyclone–and monsoon-induced rainfall variability in Taiwan. *Journal of Climate*, 23(15):4107–4120, 2010.

Chen, S.-H. and Sun, W.-Y. A one-dimensional time dependent cloud model. *Journal of the Meteorological Society of Japan*, 80(1):99–118, 2002.

Chua, X. R., Ming, Y., and Jeevanjee, N. Investigating the fast response of precipitation intensity and boundary layer temperature to atmospheric heating using a cloud-resolving model. *Geophysical Research Letters*, 2019. doi: 10.1029/2019GL082408. URL `https://agupubs.onlinelibrary.wiley.com/doi/abs/10.1029/2019GL082408`.

Chung, C. E., Ramanathan, V., and Kiehl, J. T. Effects of the South Asian absorbing haze on the northeast monsoon and surface–air heat exchange. *Journal of Climate*, 15(17):2462–2476, 2002.

Cohen, J. B. and Wang, C. Estimating global black carbon emissions using a top-down Kalman Filter approach. *Journal of Geophysical Research: Atmospheres*, 119 (1):307–323, 2014.

Collier, J. C. and Zhang, G. J. Aerosol direct forcing of the summer Indian monsoon as simulated by the NCAR CAM3. *Climate Dynamics*, 32(2-3):313–332, 2009.

Cronin, T. W. A sensitivity theory for the equilibrium boundary layer over land. *Journal of Advances in Modeling Earth Systems*, 5(4):764–784, 2013.

Ding, Y. *Monsoons over China*, volume 16. Springer Science & Business Media, 1993.

Dinh, T. and Fueglistaler, S. Mechanism of fast atmospheric energetic equilibration following radiative forcing by CO_2. *Journal of Advances in Modeling Earth Systems*, 9(7):2468–2482, 2017.

Donner, L. J., O'Brien, T. A., Rieger, D., Vogel, B., and Cooke, W. F. Are atmospheric updrafts a key to unlocking climate forcing and sensitivity? *Atmospheric Chemistry and Physics*, 16(20):12983–12992, 2016.

Dunion, J. P. and Velden, C. S. The impact of the Saharan air layer on Atlantic tropical cyclone activity. *Bulletin of the American Meteorological Society*, 85(3): 353–365, 2004.

Dunne, J. P., John, J. G., Adcroft, A. J., Griffies, S. M., Hallberg, R. W., Shevliakova, E., Stouffer, R. J., Cooke, W., Dunne, K. A., Harrison, M. J., Krasting, J. P., Malyshev, S. L., Milly, P. C. D., Phillipps, P. J., Sentman, L. T., Samuels, B. L., Spelman, M. J., Winton, M., Wittenberg, A. T., and Zadeh, N. GFDL's ESM2 Global Coupled Climate Carbon Earth System Models. Part I: Physical Formulation and Baseline Simulation Characteristics. *Journal of Climate*, 25(19): 6646–6665, 2012. doi: 10.1175/JCLI-D-11-00560.1.

Emanuel, K. and Sobel, A. Response of tropical sea surface temperature, precipitation, and tropical cyclone-related variables to changes in global and local forcing. *J. Adv. Model. Earth Syst.*, 5, 2013. doi: 10.1002/jame.20032.

Emanuel, K. A. A similarity theory for unsaturated downdrafts within clouds. *Journal of the Atmospheric Sciences*, 38(8):1541–1557, 1981.

Emanuel, K. A. An air-sea interaction theory for tropical cyclones. Part I: Steady-state maintenance. *Journal of the Atmospheric Sciences*, 43(6):585–605, 1986.

Emanuel, K. A. The maximum intensity of hurricanes. *Journal of the Atmospheric Sciences*, 45(7):1143–1155, 1988.

Evan, A. T., Kossin, J. P., Ramanathan, V., et al. Arabian Sea tropical cyclones intensified by emissions of black carbon and other aerosols. *Nature*, 479(7371): 94–97, 2011.

Fan, J., Yuan, T., Comstock, J. M., Ghan, S., Khain, A., Leung, L. R., Li, Z., Martins, V. J., and Ovchinnikov, M. Dominant role by vertical wind shear in regulating aerosol effects on deep convective clouds. *Journal of Geophysical Research: Atmospheres*, 114(D22), 2009.

Fan, J., Rosenfeld, D., Yang, Y., Zhao, C., Leung, L. R., and Li, Z. Substantial contribution of anthropogenic air pollution to catastrophic floods in Southwest China. *Geophysical Research Letters*, 42(14):6066–6075, 2015.

Fan, J., Rosenfeld, D., Zhang, Y., Giangrande, S. E., Li, Z., Machado, L. A., Martin, S. T., Yang, Y., Wang, J., Artaxo, P., et al. Substantial convection and precipitation enhancements by ultrafine aerosol particles. *Science*, 359(6374):411–418, 2018.

Fildier, B., Parishani, H., and Collins, W. Simultaneous characterization of mesoscale and convective-scale tropical rainfall extremes and their dynamical and thermodynamic modes of change. *Journal of Advances in Modeling Earth Systems*, 9(5): 2103–2119, 2017.

Fläschner, D., Mauritsen, T., and Stevens, B. Understanding the intermodel spread in global-mean hydrological sensitivity. *Journal of Climate*, 29(2):801–817, 2016.

Gettelman, A., Morrison, H., Terai, C., and Wood, R. Microphysical process rates and global aerosol-cloud interactions. *Atmospheric Chemistry and Physics*, 13(19): 9855–9867, 2013.

GFDL Atmospheric Model Development Team. The new GFDL global atmosphere and land model AM2-LM2: Evaluation with prescribed SST simulations. *Journal of Climate*, 17(24):4641–4673, 2004.

Gilford, D. M., Solomon, S., and Emanuel, K. Radiative effects of stratospheric seasonal cycles in the tropical upper troposphere and lower stratosphere. *Journal of Climate*, 30(8):2769–2783, 2017.

Ginoux, P., Prospero, J. M., Gill, T. E., Hsu, N. C., and Zhao, M. Global-scale attribution of anthropogenic and natural dust sources and their emission rates based on MODIS Deep Blue aerosol products. *Reviews of Geophysics*, 50(3):RG3005, 2012.

Gong, D.-Y. and Ho, C.-H. The Siberian High and climate change over middle to high latitude Asia. *Theoretical and Applied Climatology*, 72(1-2):1–9, 2002.

Gray, W. M. Global view of the origin of tropical disturbances and storms. *Monthly Weather Review*, 96(10), 1968.

Gray, W. M. The formation of tropical cyclones. *Meteorology and Atmospheric Physics*, 67(1-4):37–69, 1998.

Grogan, D. F., Nathan, T. R., and Chen, S.-H. Effects of Saharan dust on the linear dynamics of African easterly waves. *Journal of the Atmospheric Sciences*, 73(2): 891–911, 2016.

Guo, L., Turner, A. G., and Highwood, E. J. Local and remote impacts of aerosol species on Indian summer monsoon rainfall in a GCM. *J. Climate*, 29(19):6937–6955, 2016.

Hassim, M. E. E. and Timbal, B. Observed rainfall trends over singapore and the maritime continent from the perspective of regional-scale weather regimes. *Journal of Applied Meteorology and Climatology*, 0(0):null, 2019. doi: 10.1175/JAMC-D-18-0136.1. URL `https://doi.org/10.1175/JAMC-D-18-0136.1`.

Haywood, J. and Ramaswamy, V. Global sensitivity studies of the direct radiative forcing due to anthropogenic sulfate and black carbon aerosols. *Journal of Geophysical Research: Atmospheres*, 103(D6):6043–6058, 1998.

Heikenfeld, M., White, B., Labbouz, L., and Stier, P. Aerosol effects on deep convection: the propagation of aerosol perturbations through convective cloud microphysics. *Atmospheric Chemistry and Physics*, 19(4):2601–2627, 2019.

Held, I. M. The partitioning of the poleward energy transport between the tropical ocean and atmosphere. *Journal of the Atmospheric Sciences*, 58(8):943–948, 2001.

Held, I. M. and Soden, B. J. Robust responses of the hydrological cycle to global warming. *Journal of Climate*, 19(21):5686–5699, 2006.

Held, I. M. and Zhao, M. The response of tropical cyclone statistics to an increase in CO_2 with fixed sea surface temperatures. *Journal of Climate*, 24(20):5353–5364, 2011.

Hill, S. A., Ming, Y., and Zhao, M. Robust responses of the Sahelian hydrological cycle to global warming. *Journal of Climate*, 2018.

Hodzic, A. and Duvel, J. P. Impact of biomass burning aerosols on the diurnal cycle of convective clouds and precipitation over a tropical island. *Journal of Geophysical Research: Atmospheres*, 123(2):1017–1036, 2018.

Honda, M., Inoue, J., and Yamane, S. Influence of low Arctic sea-ice minima on anomalously cold Eurasian winters. *Geophysical Research Letters*, 36(8), 2009.

Hong, S.-Y., Noh, Y., and Dudhia, J. A new vertical diffusion package with an explicit treatment of entrainment processes. *Monthly Weather Review*, 134(9):2318–2341, 2006.

Horowitz, L. W. Past, present, and future concentrations of tropospheric ozone and aerosols: Methodology, ozone evaluation, and sensitivity to aerosol wet removal. *Journal of Geophysical Research: Atmospheres*, 111, 2006. D22211.

Horowitz, L. W., Walters, S., Mauzerall, D. L., Emmons, L. K., Rasch, P. J., Granier, C., Tie, X., Lamarque, J.-F., Schultz, M. G., Tyndall, G. S., et al. A global simulation of tropospheric ozone and related tracers: Description and evaluation of MOZART, version 2. *Journal of Geophysical Research: Atmospheres*, 108(D24): 4784, 2003.

Johnson, R. H. and Houze, Jr, R. A. *Monsoon Meteorology*, chapter Precipitating cloud systems of the Asian monsoon, page 308. 1987.

Juneng, L. and Tangang, F. T. Long-term trends of winter monsoon synoptic circulations over the maritime continent: 1962–2007. *Atmospheric Science Letters*, 11 (3):199–203, 2010.

Khairoutdinov, M. and Kogan, Y. A new cloud physics parameterization in a large-eddy simulation model of marine stratocumulus. *Monthly Weather Review*, 128(1): 229–243, 2000.

Kim, B.-M., Son, S.-W., Min, S.-K., Jeong, J.-H., Kim, S.-J., Zhang, X., Shim, T., and Yoon, J.-H. Weakening of the stratospheric polar vortex by Arctic sea-ice loss. *Nature Communications*, 5:4646, 2014.

Koch, D., Schulz, M., Kinne, S., McNaughton, C., Spackman, J. R., Balkanski, Y., Bauer, S., Berntsen, T., Bond, T. C., Boucher, O., Chin, M., Clarke, A., De Luca, N., Dentener, F., Diehl, T., Dubovik, O., Easter, R., Fahey, D. W., Feichter, J., Fillmore, D., Freitag, S., Ghan, S., Ginoux, P., Gong, S., Horowitz, L., Iversen, T., Kirkevg, A., Klimont, Z., Kondo, Y., Krol, M., Liu, X., Miller, R., Montanaro, V., Moteki, N., Myhre, G., Penner, J. E., Perlwitz, J., Pitari, G., Reddy, S., Sahu, L., Sakamoto, H., Schuster, G., Schwarz, J. P., Seland, ., Stier, P., Takegawa, N., Takemura, T., Textor, C., van Aardenne, J. A., and Zhao, Y. Evaluation of black carbon estimations in global aerosol models. *Atmospheric Chemistry and Physics*, 9:9001–9026, 2009.

Kopparla, P., Fischer, E. M., Hannay, C., and Knutti, R. Improved simulation of extreme precipitation in a high-resolution atmosphere model. *Geophysical Research Letters*, 40(21):5803–5808, 2013.

Koseki, S., Koh, T. Y., and Teo, C. K. Borneo vortex and mesoscale convective rainfall. *Atmospheric Chemistry and Physics*, 2014.

Kovilakam, M. and Mahajan, S. Confronting the "Indian summer monsoon response to black carbon aerosol" with the uncertainty in its radiative forcing and beyond. *Journal of Geophysical Research: Atmospheres*, 121(13):7833–7852, 2016.

Lau, K., Kim, M., and Kim, K. Asian summer monsoon anomalies induced by aerosol direct forcing: the role of the Tibetan Plateau. *Climate Dynamics*, 26(7-8):855–864, 2006.

Lebo, Z. and Seinfeld, J. Theoretical basis for convective invigoration due to increased aerosol concentration. *Atmospheric Chemistry and Physics*, 11(11):5407–5429, 2011.

Lebo, Z., Morrison, H., and Seinfeld, J. Are simulated aerosol-induced effects on deep convective clouds strongly dependent on saturation adjustment? *Atmospheric Chemistry and Physics*, 12(20):9941–9964, 2012.

Lee, S. S., Guo, J., and Li, Z. Delaying precipitation by air pollution over the Pearl River Delta: 2. Model simulations. *Journal of Geophysical Research: Atmospheres*, 121(19), 2016.

Li, X. and Ting, M. Understanding the Asian summer monsoon response to greenhouse warming: the relative roles of direct radiative forcing and sea surface temperature change. *Climate Dynamics*, 49(7-8):2863–2880, 2017.

Lilly, D. K. Models of cloud-topped mixed layers under a strong inversion. *Quarterly Journal of the Royal Meteorological Society*, 94(401):292–309, 1968.

Lim, H. and Chang, C. A theory for midlatitude forcing of tropical motions during winter monsoons. *Journal of the Atmospheric Sciences*, 38(11):2377–2392, 1981.

Lim, S. Y., Marzin, C., Xavier, P., Chang, C.-P., and Timbal, B. Impacts of boreal winter monsoon cold surges and the interaction with mjo on southeast asia rainfall. *Journal of Climate*, 30(11):4267–4281, 2017.

Lin, P., Paynter, D., Ming, Y., and Ramaswamy, V. Changes of the tropical tropopause layer under global warming. *Journal of Climate*, 30(4):1245–1258, 2017.

Lin, Y.-L., Farley, R. D., and Orville, H. D. Bulk parameterization of the snow field in a cloud model. *Journal of Climate and Applied Meteorology*, 22(6):1065–1092, 1983.

Lu, J., Chen, G., and Frierson, D. M. Response of the zonal mean atmospheric circulation to El Niño versus global warming. *Journal of Climate*, 21(22):5835–5851, 2008.

Lutsko, N. J. and Cronin, T. W. Increase in precipitation efficiency with surface warming in radiative-convective equilibrium. *Journal of Advances in Modeling Earth Systems*, 2018.

Mahajan, S., Evans, K. J., Truesdale, J. E., Hack, J. J., and Lamarque, J.-F. Interannual tropospheric aerosol variability in the late twentieth century and its impact on tropical Atlantic and West African climate by direct and semidirect effects. *Journal of Climate*, 25(23):8031–8056, 2012.

Mahmood, R. and Li, S. Delay in the onset of South Asian summer monsoon induced by local black carbon in an AGCM. *Theoretical and Applied Climatology*, 111(3-4): 529–536, 2013.

Martin, D. W. and Suomi, V. E. A satellite study of cloud clusters over the tropical north atlantic ocean. *Bulletin of the American Meteorological Society*, 53(2):135–157, 1972.

Menon, S., Hansen, J., Nazarenko, L., and Luo, Y. Climate effects of black carbon aerosols in China and India. *Science*, 297(5590):2250–2253, 2002.

Miller, R. and Tegen, I. Climate response to soil dust aerosols. *Journal of Climate*, 11(12):3247–3267, 1998.

Ming, Y. and Ramaswamy, V. A model investigation of aerosol-induced changes in tropical circulation. *Journal of Climate*, 24(19):5125–5133, 2011.

Ming, Y., Ramaswamy, V., and Persad, G. Two opposing effects of absorbing aerosols on global-mean precipitation. *Geophysical Research Letters*, 37(13), 2010.

Morrison, H. On the robustness of aerosol effects on an idealized supercell storm simulated with a cloud system-resolving model. *Atmospheric Chemistry and Physics*, 12(16):7689–7705, 2012.

Morrison, H., Thompson, G., and Tatarskii, V. Impact of cloud microphysics on the development of trailing stratiform precipitation in a simulated squall line: Comparison of one-and two-moment schemes. *Monthly Weather Review*, 137(3):991–1007, 2009.

Muller, C. J., O'Gorman, P. A., and Back, L. E. Intensification of precipitation extremes with warming in a cloud-resolving model. *Journal of Climate*, 24(11): 2784–2800, 2011.

Murakami, H., Wang, Y., Yoshimura, H., Mizuta, R., Sugi, M., Shindo, E., Adachi, Y., Yukimoto, S., Hosaka, M., Kusunoki, S., et al. Future changes in tropical cyclone activity projected by the new high-resolution MRI-AGCM. *J. Climate*, 25 (9):3237–3260, 2012.

Myhre, G., Shindell, D., Bréon, F.-M., Collins, W., Fuglestvedt, J., Huang, J., Koch, D., Lamarque, J.-F., Lee, D., Mendoza, B., Nakajima, T., Robock, A., Stephens, G., Takemura, T., and Zhang, H. *Anthropogenic and Natural Radiative Forcing*, chapter 8, pages 659–740. Cambridge University Press, Cambridge, United Kingdom and New York, NY, USA, 2013. ISBN ISBN 978-1-107-66182-0. doi: 10.1017/CBO9781107415324.018.

National Environmental Agency. Annual weather review 2010. Technical report, National Environmental Agency (Singapore), 2010. URL `https://www.nea.gov.sg/docs/default-source/resource/annual-weather-review-(2010)33c25ff2d3864af089c73caa8854e4ec.pdf`.

Naylor, R. L., Battisti, D. S., Vimont, D. J., Falcon, W. P., and Burke, M. B. Assessing risks of climate variability and climate change for Indonesian rice agriculture. *Proceedings of the National Academy of Sciences*, 104(19):7752–7757, 2007.

NDRRMC. Effects of Typhoon "Yolanda" (Haiyan) . Situational Rep. 108. Technical report, NDRRMC, 2014. URL `http://www.ndrrmc.gov.ph/attachments/article/1329/Effects_of_Typhoon_YOLANDA_(HAIYAN)_SitRep_No_108_03APR2014.pdf`.

Neale, R. and Slingo, J. The Maritime Continent and its role in the global climate: A GCM study. *Journal of Climate*, 16(5):834–848, 2003.

O'Brien, T. A., Collins, W. D., Kashinath, K., Rübel, O., Byna, S., Gu, J., Krishnan, H., and Ullrich, P. A. Resolution dependence of precipitation statistical fidelity in hindcast simulations. *Journal of Advances in Modeling Earth Systems*, 8(2):976–990, 2016.

Office of Naval Research. Propagation of intra-seasonal tropical oscillations (PISTON): Science plan. Technical report, Office of Naval Research Departmental Research Initiative (DRI), 2017.

O'Gorman, P. A. Precipitation extremes under climate change. *Current Climate Change Reports*, 1(2):49–59, 2015.

O'Gorman, P. A. and Schneider, T. The physical basis for increases in precipitation extremes in simulations of 21st-century climate change. *Proceedings of the National Academy of Sciences*, 106(35):14773–14777, 2009.

Pang, B., Lu, R., and Ling, J. Impact of cold surges on the Madden-Julian oscillation propagation over the Maritime Continent. *Atmospheric Science Letters*, 19(10): e854, 2018.

Pauluis, O. and Garner, S. Sensitivity of radiative–convective equilibrium simulations to horizontal resolution. *Journal of the Atmospheric Sciences*, 63(7):1910–1923, 2006.

Paynter, D., Frölicher, T., Horowitz, L., and Silvers, L. Equilibrium climate sensitivity obtained from multimillennial runs of two GFDL climate models. *Journal of Geophysical Research: Atmospheres*, 123(4):1921–1941, 2018.

Pendergrass, A. G. and Gerber, E. P. The rain is askew: Two idealized models relating vertical velocity and precipitation distributions in a warming world. *Journal of Climate*, 29(18):6445–6462, 2016.

Persad, G. G., Ming, Y., and Ramaswamy, V. Tropical tropospheric-only responses to absorbing aerosols. *Journal of Climate*, 25(7):2471–2480, 2012.

Persad, G. G., Paynter, D. J., Ming, Y., and Ramaswamy, V. Competing atmospheric and surface-driven impacts of absorbing aerosols on the East Asian summertime climate. *Journal of Climate*, 30(22):8929–8949, 2017.

Pullen, J., Gordon, A. L., Flatau, M., Doyle, J. D., Villanoy, C., and Cabrera, O. Multiscale influences on extreme winter rainfall in the Philippines. *Journal of Geophysical Research: Atmospheres*, 120(8):3292–3309, 2015.

Putman, W. M. and Lin, S.-J. Finite-volume transport on various cubed-sphere grids. *Journal of Computational Physics*, 227(1):55–78, 2007.

Raghavan, S. V., Liu, J., Nguyen, N. S., Vu, M. T., and Liong, S.-Y. Assessment of CMIP5 historical simulations of rainfall over Southeast Asia. *Theoretical and Applied Climatology*, 132(3-4):989–1002, 2017.

Ramage, C. S. Role of a tropical maritime continent in the atmospheric circulation. *Monthly Weather Review*, 96(6):365–370, 1968.

Rayner, N., Parker, D. E., Horton, E., Folland, C., Alexander, L., Rowell, D., Kent, E., and Kaplan, A. Global analyses of sea surface temperature, sea ice, and night marine air temperature since the late nineteenth century. *Journal of Geophysical Research: Atmospheres*, 108(D14), 2003.

Richardson, T. B., Forster, P. M., Andrews, T., and Parker, D. J. Understanding the rapid precipitation response to CO_2 and aerosol forcing on a regional scale. *Journal of Climate*, (2015), 2015.

Robe, F. R. and Emanuel, K. A. Moist convective scaling: Some inferences from three-dimensional cloud ensemble simulations. *Journal of the Atmospheric Sciences*, 53 (22):3265–3275, 1996.

Romps, D. M. Response of tropical precipitation to global warming. *Journal of the Atmospheric Sciences*, 68(1):123–138, 2011.

Romps, D. M. An analytical model for tropical relative humidity. *Journal of Climate*, 27(19):7432–7449, 2014.

Romps, D. M. Exact expression for the lifting condensation level. *Journal of the Atmospheric Sciences*, 74(12):3891–3900, 2017.

Rosenfeld, D., Lohmann, U., Raga, G. B., O'Dowd, C. D., Kulmala, M., Fuzzi, S., Reissell, A., and Andreae, M. O. Flood or drought: how do aerosols affect precipitation? *Science*, 321(5894):1309–1313, 2008.

Rutledge, S. A. and Hobbs, P. V. The mesoscale and microscale structure and organization of clouds and precipitation in midlatitude cyclones. XII: A diagnostic modeling study of precipitation development in narrow cold-frontal rainbands. *Journal of the Atmospheric Sciences*, 41(20):2949–2972, 1984.

Sand, M., Iversen, T., Bohlinger, P., Kirkevåg, A., Seierstad, I., Seland, Ø., and Sorteberg, A. A standardized global climate model study showing unique properties for the climate response to black carbon aerosols. *Journal of Climate*, 28(6):2512–2526, 2015.

Schenkel, B. A., Lin, N., Chavas, D., Oppenheimer, M., and Brammer, A. Evaluating outer tropical cyclone size in reanalysis datasets using quikSCAT data. *Journal of Climate*, 30(21):8745–8762, 2017.

Schollaert, S. E. and Merrill, J. T. Cooler sea surface west of the Sahara Desert correlated to dust events. *Geophysical Research Letters*, 25(18):3529–3532, 1998.

Seinfeld, J. H. and Pandis, S. N. *Atmospheric Chemistry and Physics: From Air Pollution to Climate Change*. John Wiley & Sons, 2012.

Sillmann, J., Kharin, V., Zhang, X., Zwiers, F., and Bronaugh, D. Climate extremes indices in the CMIP5 multimodel ensemble: Part 1. Model evaluation in the present climate. *Journal of Geophysical Research: Atmospheres*, 118(4):1716–1733, 2013.

Sillmann, J., Stjern, C. W., Myhre, G., and Forster, P. M. Slow and fast responses of mean and extreme precipitation to different forcing in CMIP5 simulations. *Geophysical Research Letters*, 44(12):6383–6390, 2017.

Simpson, J., Keenan, T. D., Ferrier, B., Simpson, R., and Holland, G. Cumulus mergers in the maritime continent region. *Meteorology and Atmospheric Physics*, 51(1-2):73–99, 1993.

Sobel, A. H., Nilsson, J., and Polvani, L. M. The weak temperature gradient approximation and balanced tropical moisture waves. *Journal of the Atmospheric Sciences*, 58(23):3650–3665, 2001.

Stephens, G. L., L'Ecuyer, T., Forbes, R., Gettelmen, A., Golaz, J.-C., Bodas-Salcedo, A., Suzuki, K., Gabriel, P., and Haynes, J. Dreary state of precipitation in global models. *Journal of Geophysical Research: Atmospheres*, 115(D24), 2010.

Stevens, B. and Feingold, G. Untangling aerosol effects on clouds and precipitation in a buffered system. *Nature*, 461(7264):607, 2009.

Storer, R. L. and van den Heever, S. C. Microphysical processes evident in aerosol forcing of tropical deep convective clouds. *Journal of the Atmospheric Sciences*, 70 (2):430–446, 2013.

Strong, J. D., Vecchi, G. A., and Ginoux, P. The response of the tropical Atlantic and West African climate to Saharan dust in a fully coupled GCM. *Journal of Climate*, 28(18):7071–7092, 2015.

Sugi, M., Murakami, H., and Yoshimura, J. On the mechanism of tropical cyclone frequency changes due to global warming. *Journal of the Meteorological Society of Japan*, 90:397–408, 2012.

Takahashi, K. Radiative constraints on the hydrological cycle in an idealized radiative–convective equilibrium model. *Journal of the Atmospheric Sciences*, 66 (1):77–91, 2009.

Tangang, F. T., Juneng, L., Salimun, E., Vinayachandran, P., Seng, Y. K., Reason, C., Behera, S. K., and Yasunari, T. On the roles of the northeast cold surge, the Borneo vortex, the Madden-Julian Oscillation, and the Indian Ocean Dipole during the extreme 2006/2007 flood in southern Peninsular Malaysia. *Geophysical Research Letters*, 35(14), 2008.

Tao, W.-K., Li, X., Khain, A., Matsui, T., Lang, S., and Simpson, J. Role of atmospheric aerosol concentration on deep convective precipitation: Cloud-resolving model simulations. *Journal of Geophysical Research: Atmospheres*, 112(D24), 2007.

Tao, W.-K., Chen, J.-P., Li, Z., Wang, C., and Zhang, C. Impact of aerosols on convective clouds and precipitation. *Reviews of Geophysics*, 50(2), 2012.

Tennekes, H. A model for the dynamics of the inversion above a convective boundary layer. *Journal of the Atmospheric Sciences*, 30(4):558–567, 1973.

Toh, Y. Y., Turner, A. G., Johnson, S. J., and Holloway, C. E. Maritime continent seasonal climate biases in AMIP experiments of the CMIP5 multimodel ensemble. *Climate Dynamics*, 50(3):777–800, Feb 2018. ISSN 1432-0894. doi: 10.1007/s00382-017-3641-x. URL `https://doi.org/10.1007/s00382-017-3641-x`.

Tompkins, A. M. and Semie, A. G. Organization of tropical convection in low vertical wind shears: role of updraft entrainment. *Journal of Advances in Modeling Earth Systems*, 9(2):1046–1068, 2017.

Twomey, S. Pollution and the planetary albedo. *Atmospheric Environment*, 8(12): 1251–1256, 1974.

van den Heever, S. C., Stephens, G. L., and Wood, N. B. Aerosol indirect effects on tropical convection characteristics under conditions of radiative–convective equilibrium. *Journal of the Atmospheric Sciences*, 68(4):699–718, 2011.

Walsh, K. J., Camargo, S. J., Vecchi, G. A., Daloz, A. S., Elsner, J., Emanuel, K., Horn, M., Lim, Y.-K., Roberts, M., Patricola, C., et al. Hurricanes and climate: the US CLIVAR working group on hurricanes. *Bulletin of the American Meteorological Society*, 96(6):997–1017, 2015.

Wang, J.-J., Adler, R. F., Huffman, G. J., and Bolvin, D. An updated TRMM composite climatology of tropical rainfall and its validation. *Journal of Climate*, 27(1):273–284, 2014a.

Wang, S. and Sobel, A. H. Response of convection to relative sea surface temperature: Cloud-resolving simulations in two and three dimensions. *Journal of Geophysical Research: Atmospheres*, 116(D11), 2011.

Wang, Y., Lee, K.-H., Lin, Y., Levy, M., and Zhang, R. Distinct effects of anthropogenic aerosols on tropical cyclones. *Nature Climate Change*, 2014b.

Wilcox, E. M. and Donner, L. J. The frequency of extreme rain events in satellite rain-rate estimates and an atmospheric general circulation model. *Journal of Climate*, 20(1):53–69, 2007.

Williams, E., Rosenfeld, D., Madden, N., Gerlach, J., Gears, N., Atkinson, L., Dunnemann, N., Frostrom, G., Antonio, M., Biazon, B., et al. Contrasting convective regimes over the Amazon: Implications for cloud electrification. *Journal of Geophysical Research: Atmospheres*, 107(D20):LBA–50, 2002.

Wing, A. A. and Cronin, T. W. Self-aggregation of convection in long channel geometry. *Quarterly Journal of the Royal Meteorological Society*, 142(694):1–15, 2016.

Wu, B. and Wang, J. Winter Arctic oscillation, Siberian high and East Asian winter monsoon. *Geophysical Research Letters*, 29(19):3–1, 2002.

Yamanaka, M. D., Ogino, S.-Y., Wu, P.-M., Jun-Ichi, H., Mori, S., Matsumoto, J., and Syamsudin, F. Maritime continent coastlines controlling Earth's climate. *Progress in Earth and Planetary Science*, 5(1):21, 2018.

Yoshimura, J. and Sugi, M. Tropical cyclone climatology in a high-resolution AGCM-Impacts of SST warming and CO_2 increase. *Scientific Online Letters of the Atmosphere*, 1:133–136, 2005.

Yu, P., Rosenlof, K., Liu, S., Telg, H., Thornberry, T., Rollins, A., Portmann, R., Bai, Z., Ray, E., Duan, Y., and Pan, L. Efficient transport of tropospheric aerosol into the stratosphere via the Asian summer monsoon anticyclone. *Proceedings of the National Academy of Sciences*, 114(27):6972–6977, 2017.

Zhao, M. An investigation of the connections among convection, clouds, and climate sensitivity in a global climate model. *Journal of Climate*, 27(5):1845–1862, 2014.

Zhao, M., Held, I. M., Lin, S.-J., and Vecchi, G. A. Simulations of global hurricane climatology, interannual variability, and response to global warming using a 50-km resolution GCM. *Journal of Climate*, 22(24):6653–6678, 2009.

Zhao, M., Held, I. M., and Lin, S.-J. Some counterintuitive dependencies of tropical cyclone frequency on parameters in a GCM. *Journal of the Atmospheric Sciences*, 69(7):2272–2283, 2012.

Zhao, M., Golaz, J.-C., Held, I., Guo, H., Balaji, V., Benson, R., Chen, J.-H., Chen, X., Donner, L., Dunne, J., et al. The GFDL global atmosphere and land model AM4.0/LM4.0: 1. Simulation characteristics with prescribed SSTs. *Journal of Advances in Modeling Earth Systems*, 10(3):691–734, 2018a.

Zhao, M., Golaz, J.-C., Held, I., Guo, H., Balaji, V., Benson, R., Chen, J.-H., Chen, X., Donner, L., Dunne, J., et al. The GFDL global atmosphere and land model AM4.0/LM4.0: 2. Model description, sensitivity studies, and tuning strategies. *Journal of Advances in Modeling Earth Systems*, 10(3):735–769, 2018b.

Zhao, S., Feng, T., Tie, X., Long, X., Li, G., Cao, J., Zhou, W., and An, Z. Impact of climate change on Siberian High and wintertime air pollution in China in past two decades. *Earth's Future*, 6(2):118–133, 2018c.